2016

Submarine Groundwater Discharge and the Configuration of the Freshwater-Saltwater Interface at the Nearshore and Embayment Scales

Tyler Brandon Evans
University of South Carolina

Submarine Groundwater Discharge and the Configuration of the Freshwater-Saltwater Interface at the Nearshore and Embayment Scales

by

Tyler Brandon Evans

Bachelor of Science
University of North Carolina, 2011

Submitted in Partial Fulfillment of the Requirements

For the Degree of Doctor of Philosophy in

Geological Sciences

College of Arts and Sciences

University of South Carolina

2016

Accepted by:

Alicia Wilson, Major Professor

James Knapp, Committee Member

Tim Shaw, Committee Member

Holly Michael, Committee Member

Cheryl L. Addy, Vice Provost and Dean of the Graduate School

Dedication

I dedicate this dissertation to my loving and supportive wife, Jessica, and to my parents Wayne and Nancy who have all continually helped and encouraged me through life's challenges. I could not have reached this milestone without them.

Acknowledgements

I would like to acknowledge the University of South Carolina Graduate School for awarding me with the Dean's Dissertation Fellowship which was integral to the timely completion of my degree. I would like to thank the Department of Earth and Ocean Sciences for continued financial and academic support. I would also like to thank Dr. Alicia Wilson for three summers of financial support and for offering her seemingly infinite knowledge about all things groundwater modeling. Finally, I would like to thank my committee, lab mates, and field volunteers who have all helped me throughout my graduate school experience.

Abstract

Submarine groundwater discharge (SGD) rivals riverine discharge to the world's oceans but remains poorly understood. Until the early 1990's, geochemical budgets for the ocean were developed using material fluxes from rivers only. SGD has been shown to carry high concentrations of dissolved nutrients, metals and carbon. However, SGD is a difficult to measure, complex phenomenon driven by multiple physical processes. Groundwater flow and the resultant chemical exchange at the land-sea interface are heavily impacted by the hydrodynamic effects of mixing between variable-density fluids. In order to better understand SGD, investigations have focused on the configuration of the freshwater-saltwater interface in coastal aquifers. This dissertation contributes to the field by providing detailed study of the interplay between the freshwater-saltwater interface and SGD at multiple spatial scales. The first study in this dissertation examines the dynamics of the freshwater-saltwater interface and associated rates of tidally driven and density driven recirculation at the nearshore scale in theoretical beaches. I show that beach slope is an important control on the development of the upper saline plume and therefore associated rates of seawater recirculation and SGD. The second study focuses on SGD, seawater recirculation, and the configuration of the freshwater-saltwater interface in a beach on a transgressive barrier island in Georgia. I show that the inclusion of real-world heterogeneity in a beach groundwater model leads to important deviations from predictions made using only theoretical, homogenous beaches. The third and final study of this dissertation investigates SGD

and the freshwater-saltwater interface at Hobcaw Barony, South Carolina. I develop a conceptual model for groundwater flow at the combined nearshore-embayment scale and test the response of these systems to predicted rates of future sea-level rise. I show that SGD and solute transport at these two scales are largely independent, and that the impacts of future sea-level rise will be much more significant for the nearshore scale. Finally, this dissertation aims to provide a comprehensive, spatially-integrated understanding of the pertinent driving forces for coastal groundwater flow and solute transport to aid future studies and management decisions.

Table of Contents

List of Tables

List of Figures

Chapter 1

Introduction

Coastal hydrogeology is the study of all groundwater flow and related processes at the land-sea interface and has been a topic of active research beginning as early as the mid-1800s. Preliminary investigations of coastal groundwater resulted in the assumption that fresh and saline groundwater in coastal settings are in static equilibrium. This relationship is widely referred to as the Ghyben-Herzberg principle and was first described by a Dutch engineer named W. Badon Ghyben (Ghyben, 1889). This initial manuscript received little attention and was overlooked (Carlston, 1963). Twelve years later, an engineer named Alexander Herzberg independently reached the same conclusion studying water resources on the island of Norderney, the Netherlands (Herzberg, 1901). However, as pointed out by *Carlston* [1963], the first description of this principle was actually published 61 years prior by an American teacher named Dr. Joseph Du Commun in The American Journal of Science (Du Commun, 1828). Unfortunately, Du Commun wasn't recognized for this work, and the principle of static equilibrium between fresh and saline groundwater has always been credited to Ghyben and Herzberg. Significant revisions to the Ghyben-Herzberg principle were made in the mid-20th century as knowledge in groundwater dynamics improved.

Hydrologists eventually realized that groundwater at the land-sea interface was not in static equilibrium due to the fact that groundwater flows. *Hubbert* [1940] showed that the freshwater-saltwater equilibrium was hydrodynamic between flowing fresh

groundwater and static saline groundwater. *Glover* [1959] used analytical solutions to show that at steady state, seaward-flowing fresh groundwater discharges through the shore at the location of the freshwater-saltwater interface. *Henry* [1959] used similar analytical solutions to study the intrusion of saline water into coastal aquifers where fresh groundwater flow is steady. Other studies focused on the dynamic nature of the interface with respect to tidal fluctuations and subsequent diffusion between the fresh and salt water (Wentworth, 1948), and that diffusion drives circulation of seawater into the subsurface, eventually discharging back to the sea (Cooper, 1959). These hypotheses helped develop the framework for subsequent studies which showed that geothermal convection drove large volumes of seawater through continental shelf sediments (Kohout, 1967, 1964, 1960).

Growing interest in passive margin geology in the U.S. Atlantic continental margin in the mid-to-late-21st century led to drilling and geophysical studies that resulted in the discovery and documentation of large reserves of fresh groundwater and irregular distributions of brackish and saline groundwater deep in the continental shelf (Hathaway, 1979; Kohout et al., 1988; Manheim, 1981, 1968). However, the groundwater flow dynamics that controlled these observations were poorly understood at the time. Coastal groundwater was not a significant field of active research and publication during the 1980s and 1990s (Moore, 2010a). It was not until the paradigm-shifting discovery of large groundwater inputs to the South Atlantic Bight (Moore, 1996) that coastal groundwater, and more specifically, submarine groundwater discharge became a topic of considerable scientific inquiry for hydrogeologists, chemists and oceanographers.

Submarine groundwater discharge (SGD) is a combination of near-shore groundwater discharge and vertical flow through the continental shelf, most likely derived from the underlying sedimentary strata (Moore, 2010b). *Burnett et al*. [2003] defined submarine groundwater discharge as the flow of water on continental margins from the seabed to the coastal ocean, regardless of fluid composition or driving force. This definition has become the most widely accepted in the scientific community because it emphasizes that SGD includes both saline and fresh groundwater, as well as recirculated seawater. Previously, groundwater was not considered a major source of water to the ocean. Recent research has shown that submarine groundwater flux is significant. SGD likely contributes up to three times more water to the ocean than riverine flux in the South Atlantic Bight and is probably comprised mostly of recirculated seawater (Moore 2010b). Submarine groundwater discharge occurs regionally on continental shelves, locally through the nearshore seafloor as well as in beaches and salt marshes. Knowledge of the groundwater dynamics that control subsurface flow at the land-sea interface and the potential impact of this flow on geochemical processes is limited.

Significant chemical exchange between pore water and seawater occurs in coastal aquifers. These coastal aquifers, referred to as subterranean estuaries by *Moore* [1998], provide a locale for chemical reactions to occur. Nutrient export from coastal aquifers to the ocean is controlled by redox reactions and groundwater dynamics. As oxygenated sea water infiltrates anoxic coastal pore-water, a high redox potential is created. This enables biogeochemical reactions to occur, such as nutrient remineralization, followed by potential export to the coastal ocean (Burnett et al., 2001; Krest, 2000; Santos et al.,

2009; Schutte et al., 2015; Shaw et al., 1998; Slomp and Van Cappellen, 2004; Spiteri et al., 2006; Valiela et al., 1990). These nutrient fluxes from pore water to the ocean are dependent on groundwater dynamics at multiple spatial scales at the land-sea interface.

SGD can be separated into three spatial scales to reduce ambiguity between spatial scale and associated controls on subsurface flow: (1) the near shore scale; (2) the embayment scale; and (3) the shelf-scale (Bratton, 2010). The near shore scale spans 0-10 m offshore and contains the unconfined surficial aquifer. The embayment scale spans from 10 m offshore to as far as 10 km offshore and contains the first confined aquifer and its terminus. Finally, the shelf-scale spans the entire width and thickness of the continental shelf and includes effects from geothermal convection and change in sea level over geologic time (Bratton, 2010). This separation is important because the processes that control groundwater dynamics and variability on each of these scales are different. Furthermore, the degree to which SGD is influenced by exchange across these separate scales is poorly understood. A comprehensive understanding of SGD processes at the land-sea interface may require integrated studies across the multiple scales of flow, especially to aid in management decisions and mitigation with respect to future sea-level rise and increased pressure on groundwater drinking resources.

Sea-level is currently predicted to rise between 0.5 and 1.4 m above the 1900 level by the year 2100. Predicted rates of sea-level rise are proposed to be roughly proportional to the magnitude of warming above the temperatures of the pre-Industrial Age (Rahmstorf, 2006). However, modern revisions of predicted rates of sea-level rise have shown that sea-level is rising at an accelerated rate with respect to atmospheric temperature (Rahmstorf et al., 2012). These data suggest that IPCC sea-level projections

for the future may be biased low because they did not accurately include the impact of melting of continental ice sheets. Sea-level rise due to climactic warming is significant threat to human life as well as the economy. The average population density of the near-coastal zone (112 people/km^2) was almost 3 times higher than the average global population density (44 people/km^2) in 1990 (Nicholls and Small, 2002). In addition, socio-economic conditions in the near-coast zone are commonly disadvantaged, increasing the severity of the implications of sea-level rise for a significant portion of the world's population. These populations are also heavily reliant on fresh groundwater as a drinking resource. Currently, the impact global sea-level rise will have on groundwater dynamics and drinking water resources is poorly understood. The specific effects of sea-level rise on submarine groundwater discharge and solute transport have not been thoroughly investigated.

This dissertation aims to provide the coastal groundwater scientific community with improved understanding of SGD and the associated freshwater-saltwater interface at the nearshore and embayment scales. In chapter two, I examine the configuration of the freshwater-saltwater interface and rates of seawater recirculation in theoretical beaches of differing slope, tidal amplitude, permeability, inflow of fresh groundwater and dispersivity. Chapter three compares predictions derived from the theoretical study of Chapter two to a beach on a transgressive barrier island in southern Georgia. I also examine the impact of various heterogeneities inherent to barrier islands on SGD, seawater recirculation and the resultant freshwater-saltwater interface. Chapter four focuses on SGD and the freshwater-saltwater interface under Waccamaw Neck, SC. I develop a conceptual model for groundwater flow and solute transport at a combined

nearshore-embayment scale and test how this system will respond to future rates of sea-level rise through the year 2100. Overall, these three separate studies provide a more comprehensive knowledge of the dynamics of coastal groundwater flow and the freshwater-saltwater interface under modern and future hydrological conditions.

Chapter 2

Groundwater Transport and the Freshwater-Saltwater Interface below Sandy Beaches[1]

[1]Evans, T.B., Wilson, A.M., 2016. Groundwater transport and the freshwater-saltwater interface below sandy beaches. J. Hydrol. 538, 563-573. doi: 10.1016/j.jhydrol.2016.04.014

2.1 Abstract

Current conceptual models for groundwater flow in beaches highlight an upper saline plume, which is separated from the lower salt wedge by a zone of brackish to fresh groundwater discharge. There is currently limited knowledge of what conditions allow an upper saline plume to exist and what factors control its formation. We used variable-density, saturated-unsaturated, transient groundwater flow models to investigate the configuration of the freshwater-saltwater interface in beaches with slopes varying from 0.1 to 0.01, in the absence of waves. We also varied hydraulic conductivity, dispersivity, tidal amplitude and inflow of fresh groundwater. The simulated salinity configuration of the freshwater-saltwater interfaces varied significantly. No upper saline plumes formed in any beach with hydraulic conductivities less than 10 m/d. The slope of the beach was also a significant control. Steeper beach faces allowed stronger upper saline plumes to develop. Median sediment grain size of the beach is strongly correlated to both beach slope and permeability, and therefore the development of an upper saline plume. Prior studies of groundwater flow and salinity in beaches have used a range of theoretical dispersivities and the appropriate values of dispersivity to be used to represent real beaches remains unclear. We found the upper saline plume to weaken with the use of larger values of dispersivity. Our results suggest that upper saline plumes do not form in all beaches and may be less common than previously considered.

2.2 Introduction

Submarine groundwater discharge through beaches (SGD) has been shown to be a major contributor of nutrients, carbon and trace metals to the coastal ocean (Burnett et al., 2001; Johannes, 1980; Krest, 2000; Moore, 2010a; Paytan et al., 2006; Valiela et al., 1990; Whiting and Childers, 1989). Sandy beaches and beaches comprised of a mixture of sand and pebble make up approximately 75% of ice-free coastlines (Brown and McLachlan, 2002). Due to the global presence of beaches, groundwater flow in beaches is an integral constituent of near-shore SGD. Significant volumes of water are transported through beach aquifers by tidal pumping (Robinson et al., 2007c; Santos et al., 2011, 2010; Sun, 1997) and by discharge of fresh groundwater from terrestrial watersheds (Burnett et al., 2003; Kim and Hwang, 2002; Santos et al., 2011; Taniguchi and Iwakawa, 2004). Wave forcing and wave swash in the intertidal zone create strong hydraulic gradients, also driving groundwater flow and salt transport in the beach aquifer (Bakhtyar et al., 2013; Li et al., 2000; Longuet-Higgins, 1983; Robinson et al., 2014; Sorensen, 2006; Xin et al., 2010). A distinct freshwater-saltwater interface develops in the beach subsurface where terrestrially derived fresh groundwater and recirculating seawater mix.

Moore (1998) termed the salt-freshwater mixing zone in a coastal aquifer the subterranean estuary, emphasizing similarities between surficial estuaries and the shallow groundwater system with respect to physical and biogeochemical processes. Redox gradients and the availability of dissolved nutrients in the subterranean estuary drive geochemical transformations (Charette and Sholkovitz, 2002; Moore, 1996). Short residence times and rapid flow rates of recirculating seawater drive significant mixing in the beach aquifer and enhance discharge, driving chemical fluxes across the aquifer-

ocean interface (Uchiyama et al., 2000; Ullman et al., 2003). Further knowledge of the hydrologic processes that occur in these subterranean estuaries is necessary for quantifying coastal geochemical budgets.

The distribution of salinity below beaches is an important indicator of the degree of mixing between fresh groundwater and seawater in the subterranean estuary (Galeati et al., 1992; Lebbe, 1999; Yuqun Xue et al., 1995). This mixing between groundwater bodies is important as it sets up the potential for geochemical transformations to occur. The classic conceptual model for groundwater flow and solute transport under a beach describes flow of land-derived fresh groundwater toward the ocean, above seawater migrating inland, forming a Ghyben-Herzberg freshwater-saltwater interface (Fig. 2.1a). Seaward of this interface, seawater recirculation through the aquifer is driven by differences in fluid density (Cooper, 1959; Ghyben, 1889; Herzberg, 1901). Studies as recent as 10 years ago describe a salt-wedge freshwater-saltwater interface with no upper saline plume (Boehm et al., 2006; Cartwright et al., 2004). Field measurements from a sandy beach in Cape Henlopen, Delaware, suggest the presence of a complex mixing zone and nutrient diagenesis between terrestrial groundwater and recirculating seawater at the lower salt wedge (Ullman et al., 2003).

Other studies have significantly revised this conceptual model. In some beaches an upper saline plume (Fig. 2.1b) exists adjacent to the classic saltwater wedge, separated by an upward flow zone (freshwater tube) that discharges near the average low tide mark on the beach (Boufadel, 2000; Robinson et al., 2006). Frequent tidal inundation of the beach surface allows saline water to infiltrate into the subterranean estuary and develop a plume of higher density water above less dense, fresher groundwater below. The upper

saline plume is now a fixture of modern conceptual models for groundwater flow below beaches (Bratton, 2010; Santos et al., 2012; Thorn and Urish, 2013).

The configuration of the salinity distribution of the freshwater-saltwater interface has important implications for groundwater mixing and geochemistry in the subterranean estuary. *Robinson et al*. (2007b) showed that a beach with an upper saline plume can support a more dynamic zone of mixing in the subsurface than beaches with no upper saline plume. Oxygenated, recirculated seawater mixes with reduced groundwater and sets up a redox/pH potential for chemical transformations (Slomp and Van Cappellen, 2004; Spiteri et al., 2006). Fully defining the impact of upper saline plumes will require additional field monitoring, which in turn requires the ability to predict if, when and where an upper saline plume is likely to develop.

Motivated by the absence of the upper saline plume in several studies, as well as our own field site on Sapelo Island, Ga, we hypothesized that upper saline plumes do not exist in all beaches and their formation is controlled by major hydrogeologic properties such as beach slope, permeability, tidal amplitude, dispersion and fresh groundwater input. We constructed variable-density, saturated-unsaturated, transient groundwater flow models to perform a sensitivity analysis of the major factors controlling groundwater flow and salinity distribution in beaches.

2.2.1 Groundwater exchange below beaches

Although previous studies have not directly tested the effects of flow on the configuration of the salt distribution of the freshwater-saltwater interface, they have investigated the driving forces for flow through a beach. *Robinson et al.* (2007c) studied the rate of water exchange across the aquifer-ocean interface as driven by tidal pumping. They performed

a sensitivity analysis of major nondimensional parameters related to tidally driven and density driven recirculation (TDR and DDR, respectively) in beach aquifers. TDR is the flow of seawater driven into the beach driven by tides, normalized to the terrestrially derived fresh groundwater flow into the beach. DDR refers to density-driven convection of seawater into the beach normalized to the terrestrially derived fresh groundwater flow. Of particular interest here is the nondimensional ratio of the width of the intertidal zone to tidal propagation distance (Li et al., 2000; Robinson et al., 2007c):

$$\varepsilon = A\cot(\beta)\lambda \qquad (2.1)$$

where A is tidal amplitude, β is beach slope and λ is the tidal propagation distance:

$$\lambda = \sqrt{\frac{n_e\omega}{2KH}} \qquad (2.2)$$

where n_e is effective porosity, ω is tidal period, K is hydraulic conductivity and H is aquifer depth. The tidal propagation distance described by equation (2.2) describes the reduction of the amplitude of the tide as it propagates into and through the beach aquifer (Nielsen, 1990). *Robinson et al.* (2007c) held all parameters in equation (2.1) constant except beach slope (β) and tidal amplitude (A), both of which changed the horizontal shoreline excursion. Increasing the beach slope (decreasing ε) generally decreased TDR rates in the beach aquifer and increased DDR. The effect of changing ε on groundwater salinity distribution and the resulting type of freshwater-saltwater interface was not explicitly examined. A primary goal of the current paper was to test the hypothesis that ε largely controls the development of an upper saline plume in the subterranean estuary.

2.3 Numerical Models

Simulations of tidally influenced flow and solute transport processes were conducted using SUTRA (Voss and Provost, 2002). SUTRA is a finite element groundwater

modeling program that simulates variable-density, saturated-unsaturated fluid flow and transport of a single solute. We used a modified version to account for changes in total stress associated with tidal fluctuations (Wilson and Gardner 2006). The governing equation in the models is a form of the Richards equation

$$\nabla \cdot [K(\Psi)\nabla h] = S_w S_s \frac{\partial h}{\partial t} + \varphi \frac{\partial S_w}{\partial t} - \alpha_s S_w \frac{\partial \sigma_T}{\partial t} \qquad (2.3)$$

where K is hydraulic conductivity, Ψ is negative pressure head, h is hydraulic head, S_w is water saturation, φ is porosity, σ_T is total stress and S_s is the specific storage,

$$S_s = \rho g(\alpha_s + \varphi\Omega) \qquad (2.4)$$

where ρ is the density of water, g is gravity, α_s is sediment compressibility and Ω is fluid compressibility.

Five model domains were created with beach slopes of 0.01, 0.025, 0.05, 0.075 and 0.1 to determine the effect of beach slope on groundwater flow and salt transport. The modeled range of beach slopes was chosen to be representative of a range of real beaches (Bascom, 1951; Creed, 2000; McLachlan and Dorvlo, 2005). The five simulation domains contained a number of nodes ranging from a maximum of 11,707 and a minimum of 8,215. The number of elements ranged from a maximum of 11,443 to a minimum of 7,962. Element size varied from a maximum of 1 m to a minimum of 50 cm in the intertidal zone, where flow rates were the greatest, to ensure that the Peclet and Courant criteria were met. The baseline simulation had a porosity value of 0.43 and permeability of 1.2×10^{-11} m2, which is equivalent to a hydraulic conductivity of approximately 10 m /d. Tidal amplitude, was 1 m and the beach slope was 0.05. We chose a baseline freshwater flux of 7.6 x 10^{-7} m/s, which was also used in *Robinson et al.* (2007a). Longitudinal and transverse dispersivity for the baseline simulation were 10 and

1 m respectively. All of the five domains were then run through a sensitivity analysis that included a range of values for tidal amplitude, dispersivity, inflow of fresh water and permeability (Table 2.1). The values of the parameters tested were again selected to be representative of those found in real beaches. Permeability values for sandy beaches are likely to vary from approximately 10^{-12} to 10^{-10} m^2 (Wilson et al., 2008). We tested longitudinal dispersivity values that ranged from 0.5 to 10 m and held α_L/α_T constant at a value of 10 (Gelhar et al., 1992; Robinson et al., 2007c, 2006). We varied tidal amplitude from 0 to 1.5 m. In our simulations, temperature remained constant; therefore dynamic viscosity was also constant. There is slight variability between hydraulic conductivity and permeability due to variations in density between fresh and saline groundwater, but this difference is negligible. Hereafter, we report hydraulic conductivities rather than permeabilities to remain consistent with existing literature. We assumed that the sediments were homogenous and isotropic.

Boundary conditions for the model domains consisted of a no-flow boundary on the bottom, a specified fluid flux on the landward vertical boundary and a time-variable, combined specified fluid pressure and flux along the surface boundary of the domain (Fig. 2.2). For sections of the surface boundary that were never inundated by the tide, the boundary condition is no-flow. For areas that were inundated, boundary conditions were specified based on tidal height as described in *Wilson and Gardner* (2006). Inundated areas were assigned a pressure based on the depth of the overlying water column. When inundated surface nodes had saturations less than 1, a specified flux boundary was applied. If a node along the surface of the domain was exposed and the sediment was fully saturated, a seepage face formed. A semi-diurnal lunar tide was simulated using a

sinusoidal wave with a period of 12 hours. Tidal amplitude was one of the parameters systematically tested in the experiment, ranging from 0.25 to 1.5 m. Mean water level for the tidal signal was set to be 0 m.

Model domain dimensions were chosen to balance the need for accurate simulation results and computational efficiency. The boundary source of freshwater was positioned far enough away from the intertidal zone to avoid artifacts and boundary effects. The model was extended far enough offshore that the seaward no flow boundary did not interfere with development of the freshwater-saltwater interface. Final model domains ranged from 300 – 800 m in length and 32 m in depth.

For each simulation, the hydraulic head was initially set to 1m throughout the model domain; salinity was set to1 for all nodes landward of the center of the intertidal zone 34 seaward of this boundary. Salinity is reported in this manuscript using the Practical Salinity Scale of 1978 (UNESCO/ICES/SCOR/IAPSO, 1981). Initial conditions did not affect the results because all simulations ran until they reached a quasi-steady state. A total of 105 separate simulations were developed. Time steps of 10 min were required to effectively capture hydraulic responses to tidal fluctuations. All simulations reached a quasi-steady state within 550 days.

We explored three measures to rank the strength of the upper saline plume in each simulation. The first was a saline plume salinity gradient (SPSG) measured parallel to the upper boundary of the model from the center of the upper saline plume on the beach surface to the center of the freshwater tube directly seaward (Fig. 2.1b). The SPSG measurement was made at high tide in every model. Both concentration measurements were made at a depth of 1 m below land surface, representative of a typical piezometer

depth in a beach. This depth also reaches below the zone of shallow mixing induced by waves, which were not considered in our simulations. Calculated this way, the SPSG is easily measureable in field settings. We classified "strong" upper saline plumes as having an SPSG greater than 0.15. "Moderate" upper saline plumes had SPSGs between 0.05 and 0.015, and "weak" upper saline plumes had SPSGs lower than 0.05. A complete lack of an upper saline plume was characterized by an SPSG of 0.

The other two measures of groundwater flow through the beach were TDR and DDR, which were calculated as indications of the volume of water that circulated through the beach. To do so, we calculated tidally driven (Q_t) and density driven (Q_d) recharge rates in the beach aquifer. We defined Q_t to be all recharge into the beach above the elevation of low tide and Q_d to be all recharge at elevations lower than that of low tide. These volumetric fluxes were then divided by the rate of fresh water inflow into the model (Q_f) and multiplied by 100 to yield nondimensional TDR and DDR. *Robinson et al.* (2007c) segregated TDR from DDR by the location of the freshwater discharge tube, which corresponds very closely to the elevation of low tide. We did not use the location of the freshwater discharge tube specifically because it did not exist in every simulation. This approach does not measure density-driven recirculation that occurs when density gradients center around the high tide line, but our purpose was to identify the presence and importance of the freshwater tube.

We note that the saline plume salinity gradient, as defined above, provides an indication of whether an upper saline plume exists at a site, as determined by whether an identifiable freshwater tube is present. TDR and DDR are instead measures of how much water flows through the system. DDR has the potential to co-vary with the measured

SPSG because higher salinity gradients in the upper saline plume may correspond to larger density gradients surrounding the lower salt water wedge. These gradients in turn drive DDR. TDR is clearly required if an upper saline plume is to form, but the relationship between TDR and strong upper saline plumes is more complex.

2.4 Results

Our baseline simulation (Table 2.1) was used as a point of comparison for subsequent simulations due to the moderate parameter values used and upper saline plume that developed (Fig. 2.3a-e). The maximum groundwater salinity in the upper saline plume was approximately 33, and the minimum salinity of groundwater discharging from the adjacent freshwater tube was approximately 29. In this simulation SPSG was 0.11, which indicates a moderate saline plume based on our criteria. TDR for the baseline simulation was 56% and DDR was 10%. Average groundwater flow rates in the intertidal zone were greatest during low tides and the least during flood tides (Fig. 2.3b-e). In general, saline groundwater infiltrated into the aquifer during high tides and was discharged to the coastal ocean during low tides. Groundwater discharge from the beach aquifer was focused at the level of the tide as it moved across the beach. The maximum rate of discharge over a tidal cycle occurred in the saturated seepage face that formed just above the level of the tide during low tide.

All 105 simulations showed that a Ghyben-Herzberg freshwater-saltwater interface developed below the intertidal zone, but the width and configuration of the salinity distribution was highly variable. The maximum salinity of the upper saline plume ranged from 28 to 34 in each model, and the salinity of groundwater discharging from the freshwater tube varied from 6 to 34. For a hydraulic conductivity of 10 m/d, the

maximum measured rate for TDR was 85% and the minimum was 6%. The maximum rate for DDR was 44% and the minimum was 2%. Although groundwater flow patterns changed significantly over the course of a tidal period, the salinity in each simulation gradually progressed toward a stable configuration that remained constant throughout the tidal cycle.

The slope of the intertidal zone of the beach was found to be a major controlling factor for the development of an upper saline plume and for flow through the beach in general. For the cases simulated, larger beach slopes supported a greater SPSG, greater DDR and greater TDR than smaller beach slopes (Table 2.2). When beach slopes fell below 0.05, the upper saline plume weakened significantly and could not support density gradients high enough to drive significant rates of DDR. This relationship is illustrated very clearly in a subset of simulations where tidally averaged flow rates are compared directly to the subsequent salinity configuration (Fig. 2.4a-e). Tidally average flow rates decrease in magnitude with decreasing beach slope. Beach slopes above or equal to 0.05 had larger hydraulic gradients, allowing greater discharge rates from the beach, which in turn allowed greater rates of TDR. No upper saline plume formed in any beach with a slope of 0.01 except when the hydraulic conductivity was set high to 100 m/d.

SPSG increased with increasing rates of density driven infiltration (Fig. 2.5). Higher groundwater salinity gradients between the saline plume and freshwater tube, and therefore more distinct upper saline plumes, drove greater rates of density-driven convection under the beach. Rates of density-driven infiltration into the beach aquifer could therefore be used as an indicator of the strength of the upper saline plume in a beach, but we ultimately chose to report measured SPSGs because they can be readily

measured in the field. Infiltration rates into the beach aquifer are tedious and difficult to measure in a real beach.

Varying the hydraulic conductivity shifted the range of beach slopes that could sustain an upper saline plume (Fig. 2.6a). A hydraulic conductivity of 100 m/d allowed the formation of an upper saline plume only in beaches with slopes of 0.025 and 0.01. In beaches with slopes greater than 0.025, only a lower salt wedge developed. Only very low-slope beaches allowed a weak upper saline plume at this hydraulic conductivity. A hydraulic conductivity of 10 m/d led to the highest SPSG measurements and therefore the most distinct upper saline plumes (Fig. 2.6a). With this hydraulic conductivity, seawater could effectively infiltrate the subsurface during inundation, and tidally-averaged flow rates through the beach were high enough to sustain an upper saline plume. No upper saline plumes formed in any beach with hydraulic conductivities less than or equal to 1 m/d because tidally-averaged flow rates through the beach were too low. TDR and DDR rates were proportional to hydraulic conductivity because greater volumes of water moved through the beach aquifers with higher hydraulic conductivities (Fig. 2.7a; 2.8a).

We also varied the flux of fresh groundwater from the landward boundary into the models. The magnitude of fresh groundwater input into the model strongly influenced the development of the upper saline plume and associated SPSG (Fig. 2.6b). SPSGs were very low for inflow velocities of ~10^{-8} to 10^{-6} m/s, increasing significantly for velocities of 7.6 x 10^{-6} m/s and greater (Fig. 2.6b). A greater inflow of fresh groundwater caused a sharper salinity gradient to develop at the freshwater-saltwater interface because the salinity of water discharging through the freshwater tube was lower. For a given freshwater flow, SPSGs generally increased with increasing beach slope. No upper saline

plumes formed in beaches with a slope of 0.01 regardless of the magnitude of fresh groundwater input. Rates of TDR decreased with higher fluxes of terrestrially derived freshwater (Fig. 2.7b). DDR increased with higher fluxes of terrestrially derived freshwater for beach slopes greater than 0.01 (Fig. 2.8b).

We found that tidal amplitude exhibited significant control on the strength of the upper saline plume. For beaches with slopes of 0.05 to 0.1, the SPSG and tidal amplitude were approximately negatively proportional (Fig. 2.6c). Higher tidal amplitudes caused inundation of larger areas of the beach, spreading out the upper saline plume and decreasing the SPSG. The simulations with an intertidal zone slope of 0.025 were particularly sensitive to tidal amplitude; for this slope, the upper saline plume failed to form for tidal amplitudes less than or equal to 0.75 m. For tidal amplitudes of 1 m or greater, the associated SPSG was relatively constant. As previously indicated, no upper saline plumes formed in beaches with a slope of 0.01 regardless of the tidal amplitude. Rates of TDR increased with increasing tidal amplitude as larger areas of the beach were inundated by the tide (Fig. 2.7c). Rates of DDR increased with decreasing tidal amplitude because stronger salinity gradients developed between the saline plume and adjacent freshwater tube (Fig. 2.8c).

Dispersivity was also found to be a major controlling factor for the development of an upper saline plume in a beach. Transverse dispersivity was a much more significant control on salinity configuration than longitudinal dispersivity because the salinity gradients developed perpendicular to the dominant flow direction in the beach (vertical). For beaches with slopes of 0.05 or greater, smaller dispersivities increased the SPSG and allowed more distinct upper saline plumes to form (Fig. 2.6d). For beaches with lower

slopes and smaller dispersivities, upper saline plumes did not form. This occurred because a minimum level of mixing was required in the aquifer to allow the formation of an upper saline plume. Varying dispersivities in a beach with a slope of 0.01 did not produce an upper saline plume. Rates of TDR were relatively constant with increasing dispersivities while rates of DDR decreased with increasing dispersivities (Supp. 1D; 2D).

2.5 Discussion

Our results suggest that upper saline plumes do not form in all beaches. We found that the most significant controls on the development of an upper saline plume in a beach were hydraulic conductivity, the slope of the intertidal zone and fresh groundwater inflow. Additionally, we suggest that the median sediment grain size of the beach is strongly correlated to the development of an upper saline plume in the subterranean estuary due to the dependence of hydraulic conductivity and beach slope on sediment grain size.

Sediment grain size is an empirical predictor for the slope of the intertidal zone on an exposed beach (Bascom, 1951):

$$\beta = 0.0045e^{5.4d} \qquad (2.5)$$

where β is the beach slope and d is the median grain size of the beach sediments. The grain size of sediments deposited on a beach is controlled by the wave energy in the coastal ocean. Sediments with a larger median grain size can support a steeper slope while sediments with smaller grain sizes build shallower slopes. Due to the relationship between grain size and beach slope, grain size is also correlated to the development of an upper saline plume. *Wilson et al.* (2008) showed that the median grain size of coastal

sediments is also a good indicator of permeability. Sediments with larger grain sizes had higher permeability values in both near-shore and continental shelf samples and can be fit by the following equation:

$$k = 4 \times 10^{-10} d^{1.6} \qquad (2.6)$$

where *k* is permeability and *d* is the median grain size of the sediments.

Due to the correlation between sediment grain size and both permeability and beach slope, grain size of beach sediments is also indirectly correlated to the presence/absence of an upper saline plume.

The link between grain size, beach slope and permeability indicates a very specific set of conditions required to have an upper saline plume in a beach. As the median grain size in a beach increases, the permeability and slope of the intertidal zone increase (Fig. 2.9). Steeper slopes in the intertidal zone support more distinct upper saline plumes, but this is balanced by the fact that permeability values also increase and flushing rates are more rapid. Beaches with shallow slopes have finer sediments with lower permeability values, further reducing the potential for developing an upper saline plume.

Strong upper saline plumes have been well documented in sandy beaches around the world, including Waquoit Bay, Cape Henlopen and Moreton Island (Abarca et al., 2013; Heiss and Michael, 2014; Kuan et al., 2012; Robinson et al., 2006). All three of these beaches, however, have intertidal zone slopes of approximately 0.09 or greater. *Bascom* (1951) compiled approximately 500 profiles from 40 beaches on the Pacific Coast of the United States. Beach slopes in the intertidal zone ranged from 0.25 to 0.01. *McLachlan and Dorvlo* (2005) categorized 161 sandy beach transects from a wide variety

of locations worldwide and found that beach slopes range from approximately 0.2 to 0.0125, with an average beach slope of 0.037. Our model results predict that more prominent upper saline plumes develop and persist in beaches with greater slopes. Upper saline plumes weakened significantly in beaches with intertidal zone slopes less than 0.05. This suggests that a large portion of the world's beaches do not exhibit a strong, persistent upper saline plume.

We can now consider the relationship between the presence of an upper saline plume and the volume of submarine groundwater discharge. Strong upper saline plumes had high rates of TDR and DDR. Our model results indicate that increasing values of ε (lower beach slopes) lead to lower SPSGs in the beach, representative of weak or absent upper saline plumes (Fig. 2.10a). *Robinson et al.* (2007c) showed that increasing values of ε led to increasing rates of TDR for steeper beaches (0.1 to 0.4), and TDR became independent of slope for moderate beach slopes (0.067). Our results show that TDR (Fig. 2.10b) and DDR (Fig. 2.10c) drop off significantly for moderate to low slope beaches (0.05 to 0.01). As the beach slope approached the horizontal (increasing values of ε), the hydraulic gradient that drives seawater infiltration into the intertidal zone decreased. These relationships indicate that the formation of a stable upper saline plume occurs in beaches where TDR is sufficient to supply the beach with seawater each tidal cycle, and where DDR is high due to strong convective flow associated with a strong salinity gradient. Higher SPSGs form in beaches with higher slopes. Upper saline plumes cannot persist in the subterranean estuary through the tidal cycle when TDR and DDR are low, as they are in beaches with low slopes.

Controls on the formation of an upper saline plume can be further explored by examining the relationship between advection and dispersion in the beach aquifer. We can quantify these relationships by using the Peclet number:

$$P_e = \frac{v_x L}{D} = \frac{L}{\alpha_T} \qquad (2.7)$$

where v_x is groundwater velocity, L is the length scale of interest, D the dispersion coefficient and α_T is transverse dispersivity. Substituting the width of the intertidal zone (equation 1) for L yields:

$$P_e = \frac{L}{\alpha_T} = \frac{A \cot \beta}{\alpha_T} \qquad (2.8)$$

where A is tidal amplitude and β is the slope of the beach. The lowest Peclet number calculated was equal to 2.5, for a small tidal amplitude (0.25 m) and low beach slope (0.01). Therefore, all of the calculated Peclet numbers are greater than 1, indicating that advection dominates as the solute transport process in our simulations. The most significant SPSGs, and therefore the strongest upper saline plumes, occurred with relatively low (< 15) Peclet numbers (Fig. 2.10d). When Peclet numbers are very high, the upper saline plume gets flushed out and SPSGs decrease to 0. In order for an upper saline plume to develop, advection through the subterranean aquifer is necessary.

Anthropogenic modifications to beaches have the potential to alter groundwater flow and exchange. Coastal engineering and beach nourishment are currently active strategies to combat sediment loss due to erosion and longshore drift in beaches. A common practice to reduce sediment loss from beaches with high rates of erosion is to build up the beach face with sands with larger grain sizes (California Department of Boating and Waterways, 2002; Davison et al., 1992; Delft Hydraulics, 1987). The larger grain size means that less sediment can be entrained by the local waves due to the

increased grain size, leading to a net decrease in erosion. Beach nourishment could artificially increase beach slopes and permeability values, thereby allowing the development of an upper saline plume. Inducing the development of an upper saline plume in a beach could lead to increased rates of nutrient remineralization and potential export to the coastal ocean through higher rates of groundwater mixing and exchange. If a beach managed in such a way is within a coastal zone that is already experiencing anthropogenic eutrophication and algal blooms, increased nutrient export to sensitive coastal waters could further reduce water quality. Coastal managers should consider the potential effects of beach modifications on groundwater systems and the fertility of the local coastal ocean.

It is important to consider that real beaches exhibit variability in sediment grain size and therefore permeability and beach slope. Some beaches have multiple slope breaks along their profiles where small, localized upper saline plumes could develop. Beach profiles are also dynamic with respect to season, experiencing increased rates of erosion during winter months and increased sediment accretion during summer (Aubrey, 1979). Beaches on transgressive barrier islands can have relic marsh muds buried in the subsurface, leading to complex stratigraphy and permeability anisotropy (Anderson et al., 2000). Although quantifying these effects is beyond the scope of the current paper, these effects clearly warrant future investigation.

In our simulations, we used a simulated tidal signal to represent tidal forcing. Real tidal signals that include variations in mean water level, sea level and lunar cycles such as spring-neap tides are likely to yield variable results. *Abarca et al*. (2013) showed that real tides, even with small tidal amplitudes, can create significant variability in fluxes in a

beach aquifer. Spring-neap tidal cycles also cause the upper saline plume to expand and contract in response to changes in tidal amplitude (Robinson et al., 2007a). Field studies with a goal of delineating an upper saline plume in a beach should span an entire lunar tidal cycle to capture the variability in both groundwater fluxes and salinity distribution.

TDR and DDR rates are important data for understanding SGD, but are difficult to measure in the field and often require computational methods to estimate. Salinity distribution in a beach aquifer is a useful indicator of groundwater flow dynamics. Measuring the salinity of groundwater is simple, and often the first step in identifying the configuration of the freshwater-saltwater interface in a beach. A saline plume salinity gradient can be measured by installing piezometers in the intertidal zone of a beach, near the average elevation of low tide and mean sea level. By also measuring the median grain size of beach sediments, the beach slope, the tidal amplitude and elevation of mean sea level at a field site, it is then possible to estimate general rates of TDR and DDR. For example, density-driven recirculation rates are related to the strength of the measured SPSG between the saline plume and the freshwater discharge tube, located near the average low-tide line. The salinity gradient increases with increasing beach slope. In general, the fresher the water in the discharge tube, the greater the rates of DDR in the beach. TDR rates are largely dependent on the slope of the beach, tidal amplitude and permeability. Beach slopes between 0.5 and 0.1 had the greatest rates of TDR, while rates decreased significantly for lower beach slopes where the hydraulic gradient across the ocean-aquifer interface was low. When both TDR and DDR rates are low, there will be no distinct upper saline plume, and the SPSG in the beach will be close to 0. Flow velocities through the beach are slowest in beaches with shallow slopes.

2.6 Conclusion

Our results suggest that the upper saline plume may be an uncommon phenomenon that only occurs in beaches with the appropriate combination of beach slope, hydraulic conductivity and fresh groundwater flux into the beach. The development of an upper saline plume under a beach requires high rates of TDR which create strong salinity gradients and therefore high rates of DDR. Steeper beach slopes supported higher SPSGs in the beach aquifer and therefore had more distinct upper saline plumes. No upper saline plumes formed in any simulations when the hydraulic conductivity was below 10 m/d. Sufficient volumes of seawater could not infiltrate the beach aquifer during high tide. Upper saline plumes were less distinct for hydraulic conductivities greater than or equal to 100 m/d because groundwater was flushed through the beach too rapidly, leading to the development of a lower salt wedge only. Increasing the fresh groundwater flux into the model decreased the salinity of groundwater that discharged seaward of the upper saline plume, increasing the SPSG.

Dispersivity also had an important effect on the distribution of salinity in the groundwater. Lower transverse dispersivities allowed higher SPSGs to develop in the simulations. Prior studies of groundwater flow and salinity in beaches have used small dispersivities (Robinson et al., 2007c). We found that the upper saline plume became much less distinct when larger dispersivities were used, because more mixing occurred in the simulations. Real beaches are highly mixed environments, with waves, heterogeneous sediments and geologic layering. Longitudinal dispersivity can vary by an order of 2 within a single field site, adding additional complications to simulating field data of

salinity distribution (Gelhar et al., 1992). The appropriate magnitude of dispersivities to be used in modeling groundwater in beaches remains unclear (Smith, 2004).

The median grain size of beach sediments has the potential to be an indicator of whether or not a beach will have an upper saline plume because of the correlations between grain size and both beach slope and permeability. In order for a beach to contain a prominent upper saline plume, the sediment grain size must allow a steep beach face to develop with permeability values high enough to allow sufficient infiltration of seawater but not too high to prevent strong salinity gradients from developing. Because of this relationship, wide, gently sloping beaches with fine grained sands will not support distinct upper saline plumes.

Finally, the observation of the presence or absence of an upper saline plume in a beach is important because it allows a conceptual model to be developed with respect to submarine groundwater discharge and seawater recirculation. If a strong upper saline plume is identified in a beach, it can be determined that rates of DDR are high. The presence of a moderate or weak upper saline plume indicates that rates of DDR are lower in that beach. A beach with no upper saline plume will still undergo DDR across the lower salt wedge, but the rates will be significantly lower than in beaches with a USP. TDR is more difficult to determine from the configuration of the salinity distribution alone because TDR is dependent on beach slope, tidal amplitude and inland fresh groundwater head. TDR is highest in beaches with moderate to steep slopes (0.05 to 0.1), large tidal amplitudes and low terrestrial groundwater flux. These types of beaches exhibit moderate/weak upper saline plumes because the SPSG decreases with increasing tidal amplitude and decreasing terrestrial groundwater flux. Therefore, beaches with

slopes between 0.05 and 0.1 and no upper saline plume have the highest rates of TDR. Beaches with slopes in this range that have an upper saline plume will likely have moderate rates of TDR. Any beaches with slopes less than 0.05 will have the lowest rates of TDR. High rates of circulation through the beach aquifer are important because they could lead to higher rates of geochemical exchange and transformation. By identifying the salinity configuration in a beach aquifer, powerful hypotheses about flow and geochemical exchange can begin to be developed from a simple measure.

Table 2.1. Parameters used in base model and subsequent beach simulations

Beach Slope	0.01	0.025	0.05*	0.075	0.1	
Tidal Amplitude (m)	0.25	0.5	0.75	1.0*	1.25	1.5
Dispersivity (m) (α_L, α_T)	(0.5, 0.05)	(1, 0.1)	(2.5, 0.25)	(5, 0.5)	(7.5, 0.75)	(10,1)*
Freshwater Flux (m/s)	7.6E-08	7.6E-07*	7.6E-06	7.6E-05	7.6E-04	
Hydraulic Conductivity (m/d)	0.1	1	10*	100		

*Baseline simulations parameters

Table 2.2. Simulations results specific to **Figure 4 (a-e)**

Model	Beach Slope	TDR	DDR	Max Average Velocity (m/d)	SPSG
a	**0.1**	62%	28%	1.24	0.129
b	**0.075**	59%	18%	1.14	0.122
c	**0.05**	56%	10%	0.784	0.114
d	**0.025**	42%	3%	0.411	0.039
e	**0.01**	17%	2.5%	0.253	0.0

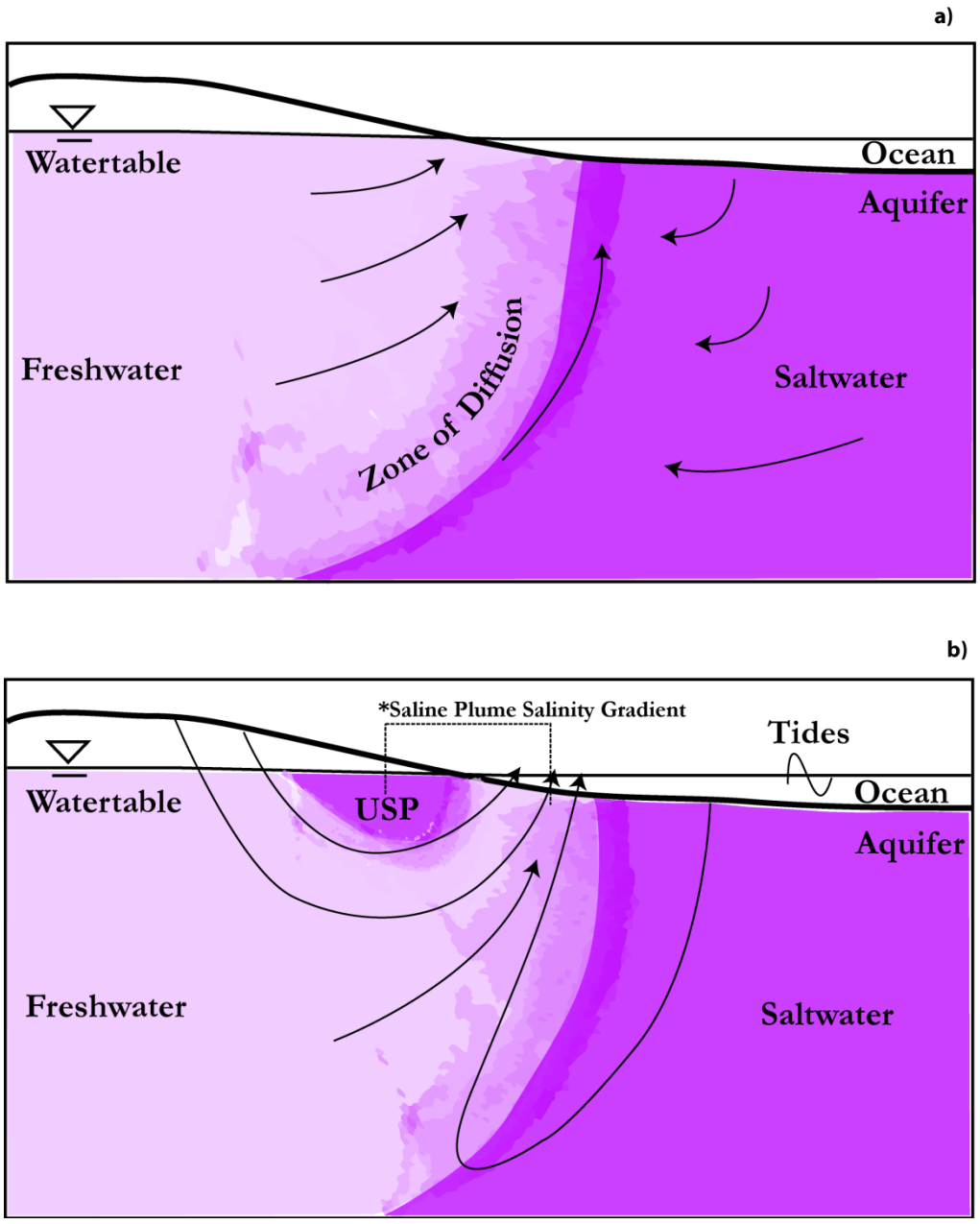

Figure 2.1. a) Conceptual model of the freshwater-saltwater interface in a beach. After Cooper (1959). **b)** The upper saline plume and associated flow paths. After Robinson et al. (2006b). A saline plume salinity gradient (SPSG) was measured from the center of the upper saline plume to the center of the adjacent seepage face in every simulation. The darker color indicates higher groundwater salinity.

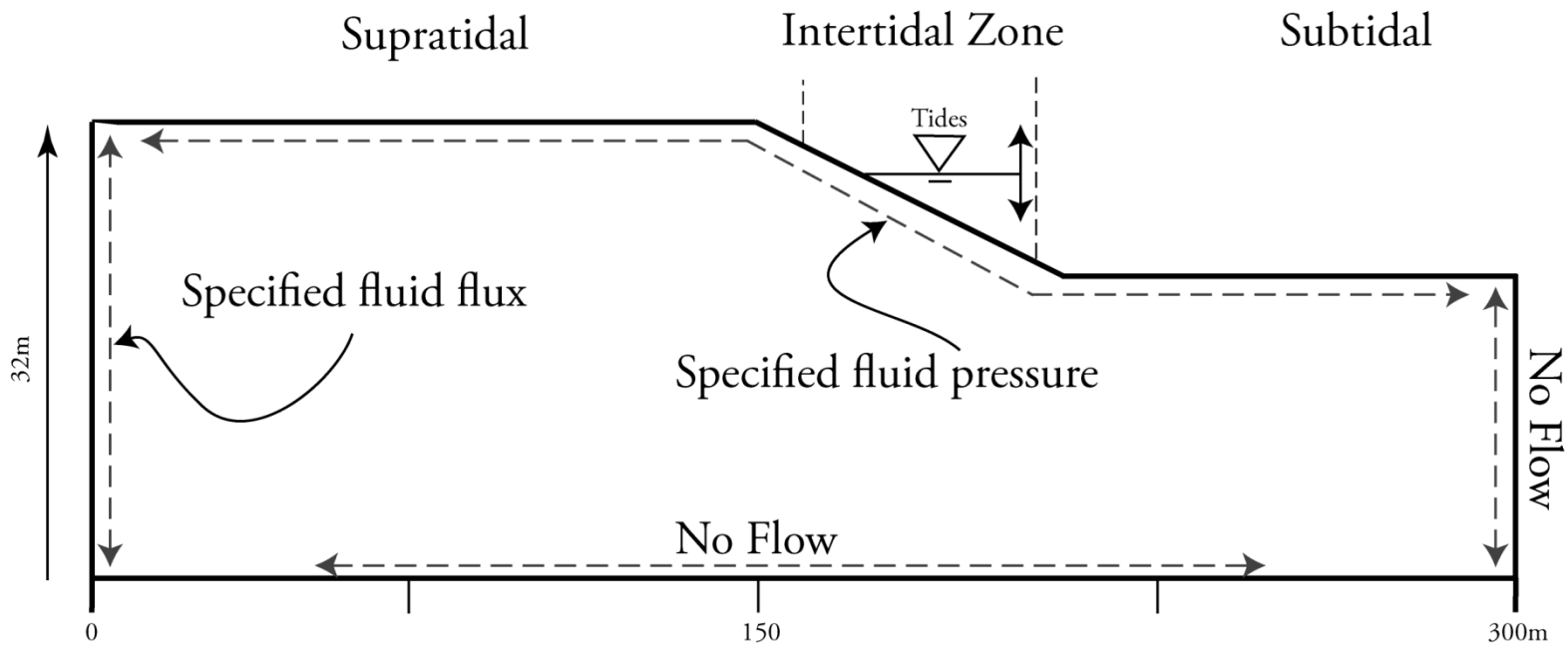

Figure 2.2. An example of one model domain (slope = 0.05) and the subsequent boundary conditions used for every beach simulation.

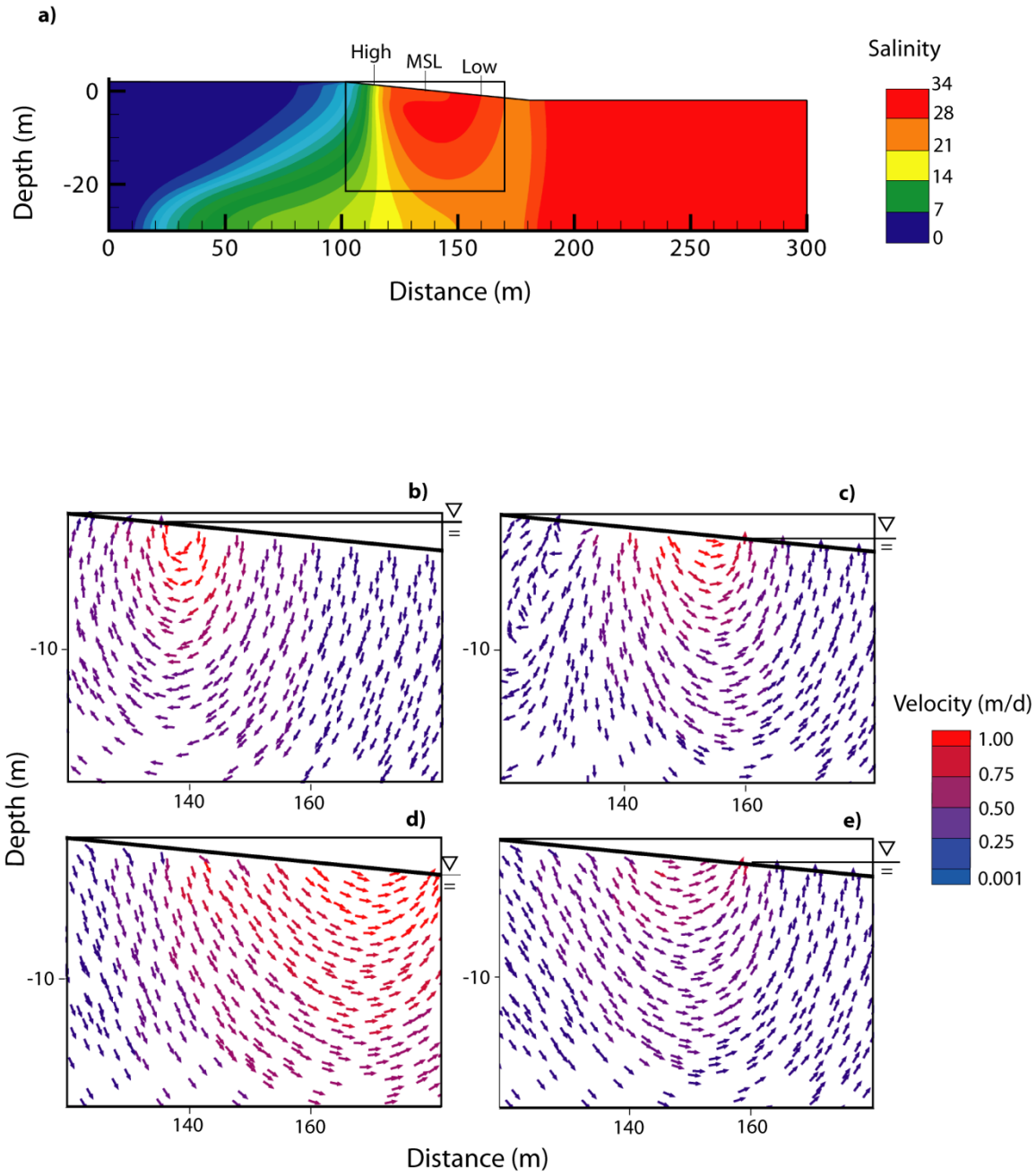

Figure 2.3. a) Salinity distribution for the baseline simulation. The salinity was normalized so that 1 = 34. The salinity gradient for this simulation was 0.114. Groundwater velocities for the baseline simulation during **b)** high tide, **c)** ebb tide, **d)** low tide and **e)** flood tide. Flow velocities were greatest during low tide and lowest during flood tide. Seawater circulated into the aquifer during rising tide.

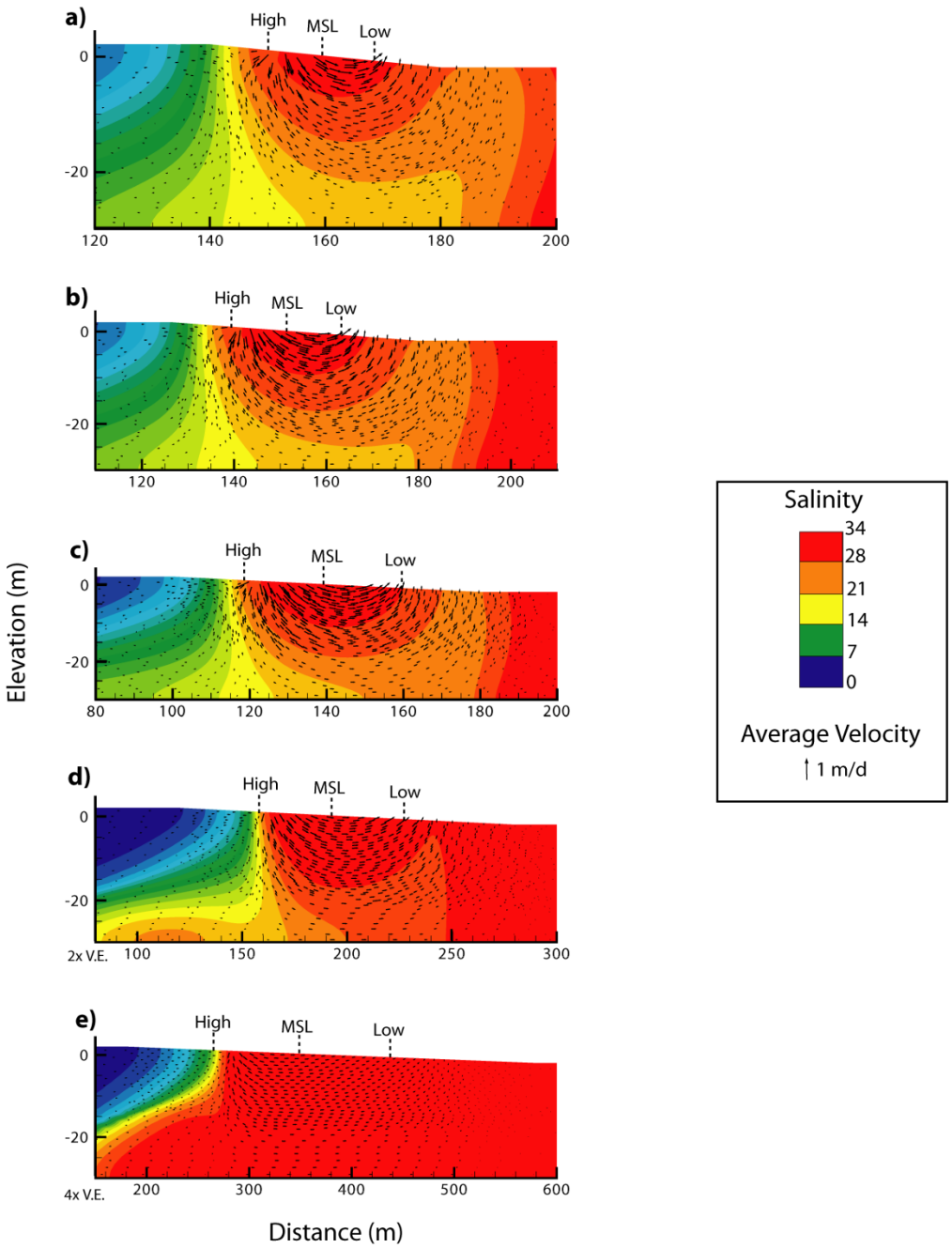

Figure 2.4. Salinity configuration and tide-averaged flow for beaches with intertidal zone slopes of **a)** 0.1, **b)** 0.075, **c)** 0.05, **d)** 0.025 and **e)** 0.01. The fresh groundwater flux in these simulations was 7.6 x 10-7 m/s, hydraulic conductivity was 10 m/d. The magnitude of the concentration gradient decreased with decreasing beach slope. As beach slope decreased, average flow rate decrease in magnitude, driving lower rates of TDR and DDR through the beach. Table 2 describes values for TDR, DDR, average velocity and salinity gradient for each simulation.

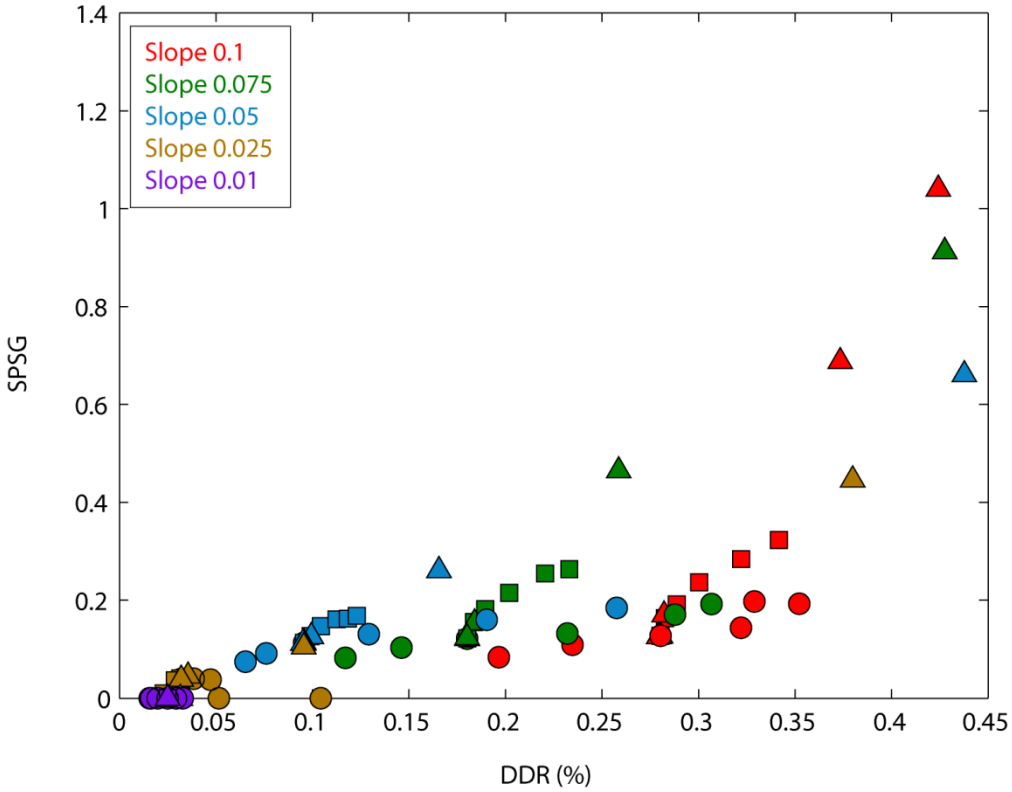

Figure 2.5. Plot of DDR versus SPSG for simulations with baseline hydraulic conductivity (10 m/d). The colors represent beach slope (0.1 to 0.01) and the symbols represent fresh groundwater inflow (triangle), dispersivity (square) and tidal amplitude (circle).

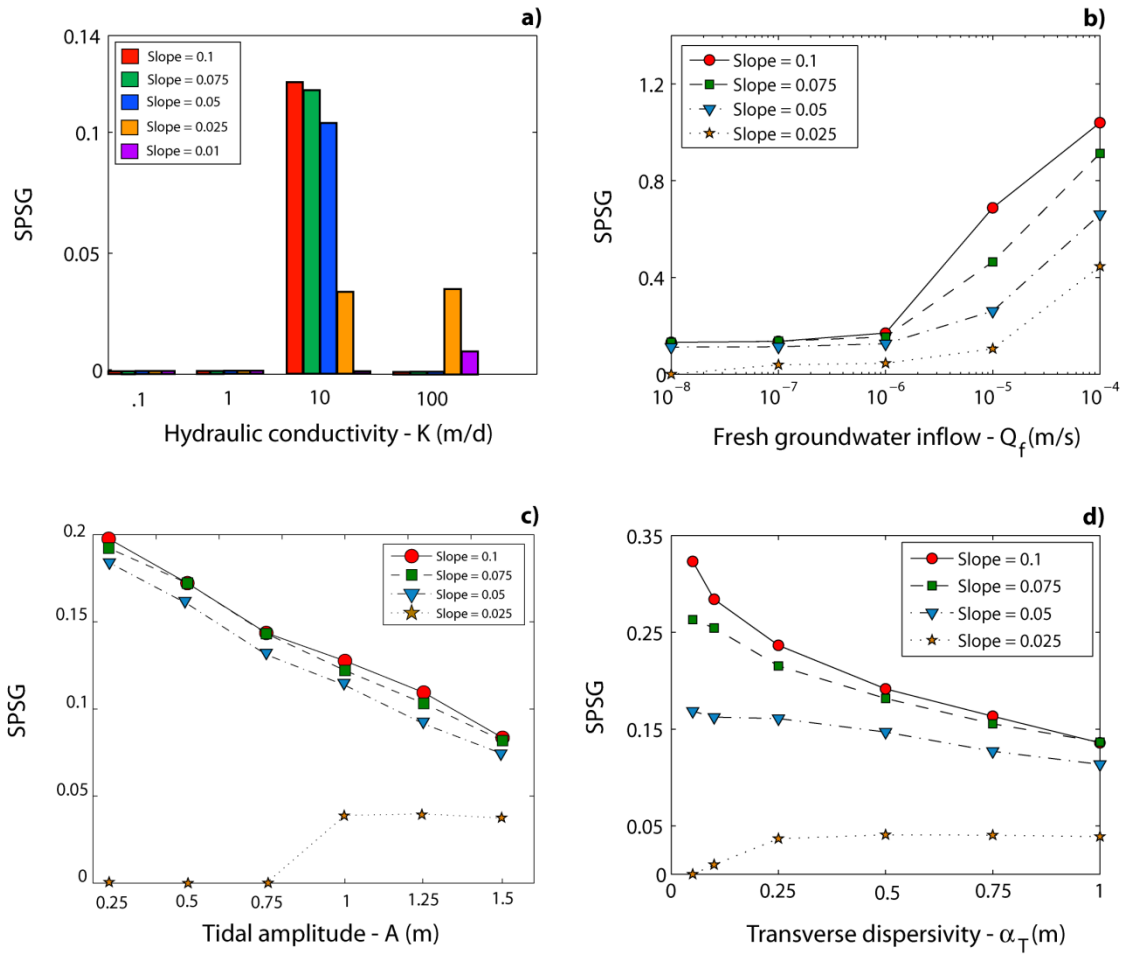

Figure 2.6. Simulation results for tested parameters vs. SPSG for each model domain. **a)** Hydraulic conductivity, **b)** Fresh groundwater inflow, **c)** Tidal amplitude and **d)** Transverse dispersivity.

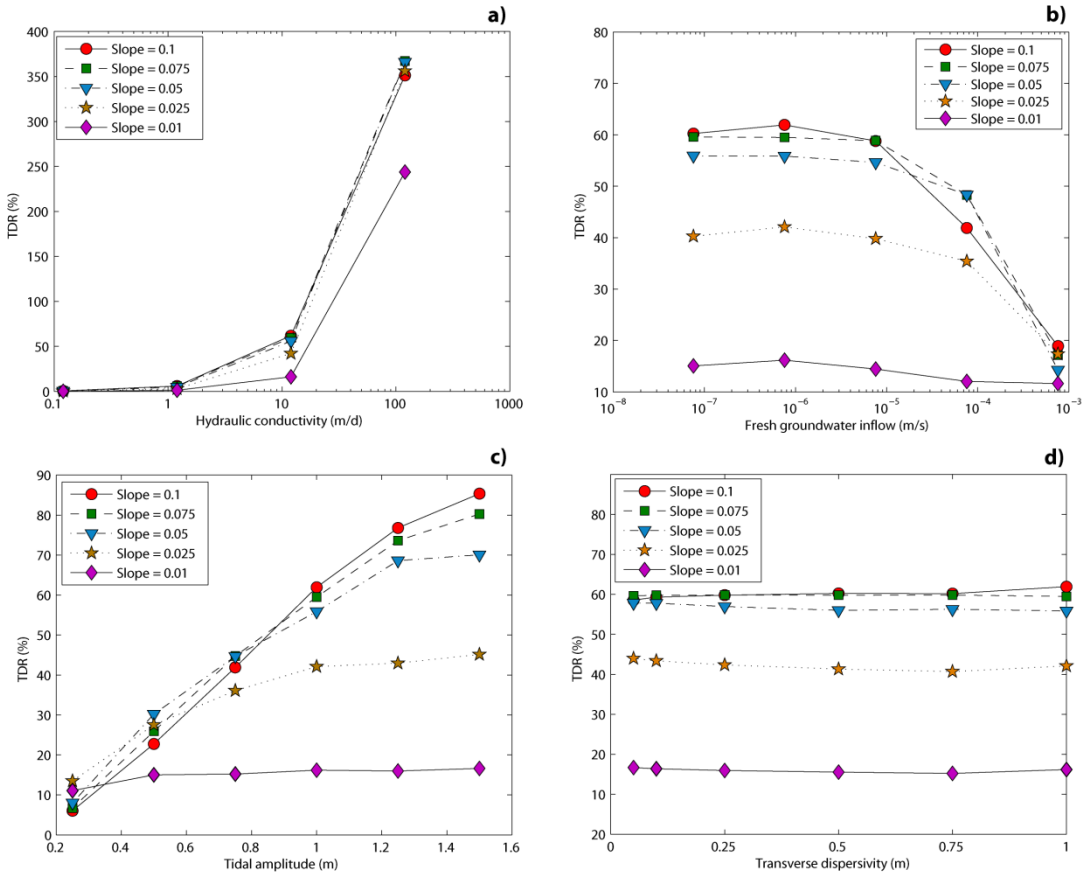

Figure 2.7. Simulation results for tested parameters vs TDR for each model domain. **a)** Hydraulic conductivity, **b)** Fresh groundwater inflow, **c)** Tidal amplitude and **d)** Transverse dispersivity.

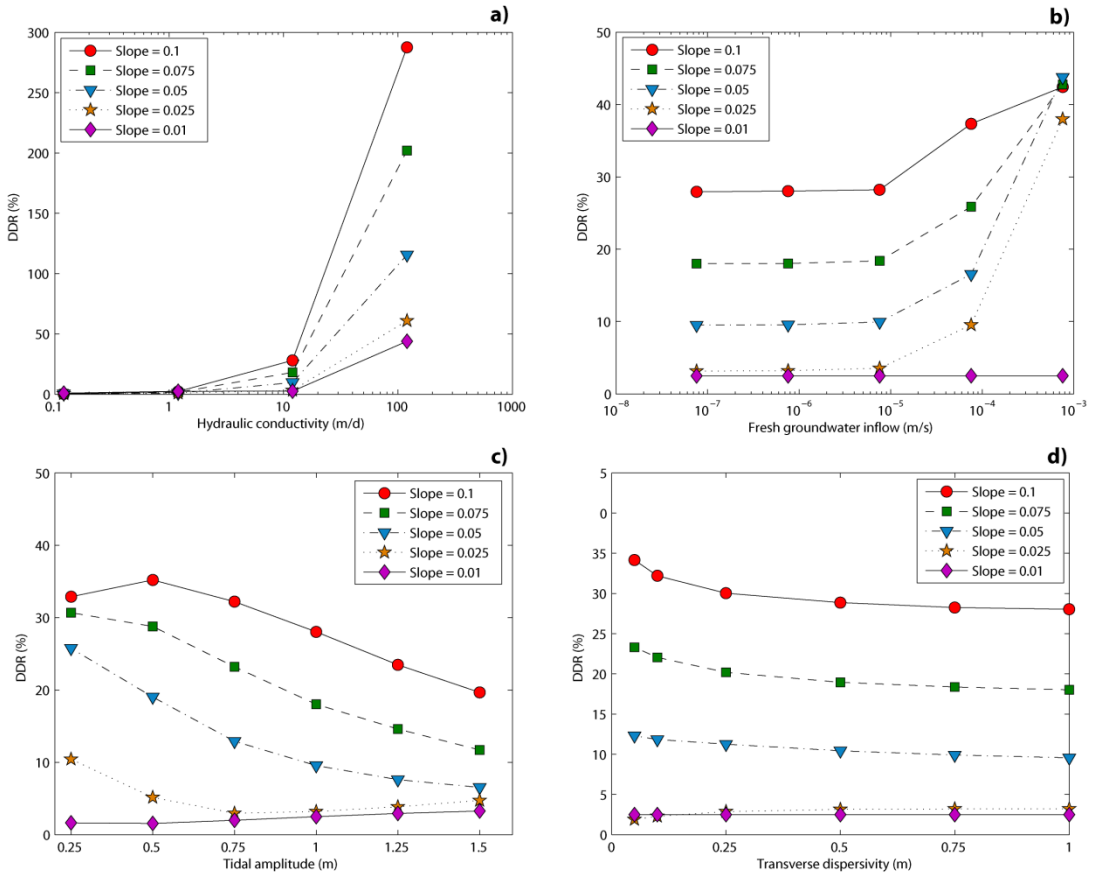

Figure 2.8. Simulation results for tested parameters vs DDR for each model domain. **a)** Hydraulic conductivity, **b)** Fresh groundwater inflow, **c)** Tidal amplitude and **d)** Transverse dispersivity.

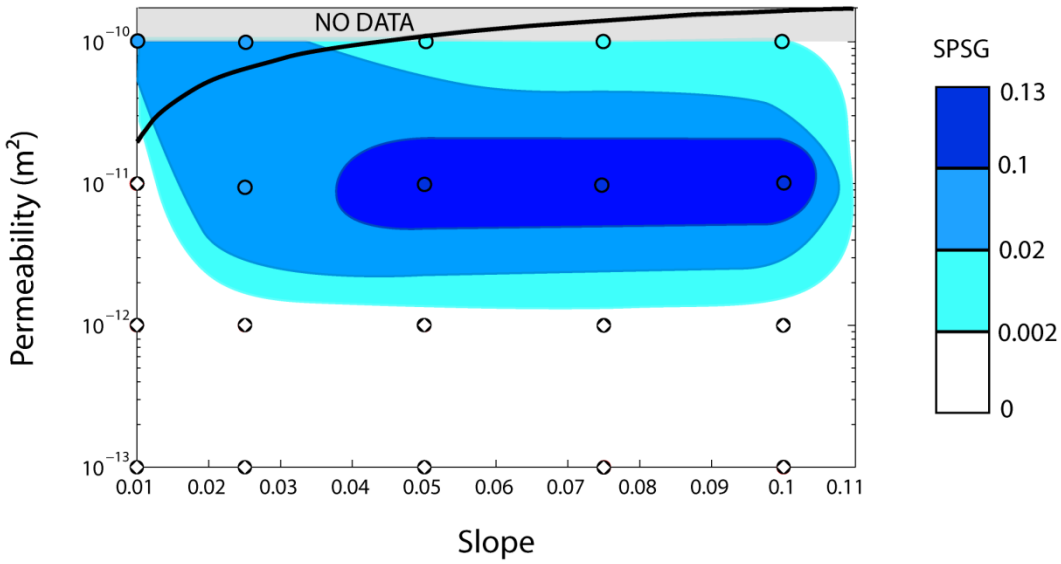

Figure 2.9. The strength an upper saline plume in a beach, as indicated by SPSG. Open circles represent simulation results. The trend line indicates permeability and beach slope calculated from median grain size (d50) based on empirical observations (Bascom, 1959; Wilson, 2008). Permeability is likely to vary significantly in beaches, and reasonable values may fall below the line. Only permeability and beach slope were varied in these simulation results; the remaining parameters were equivalent to the baseline simulation.

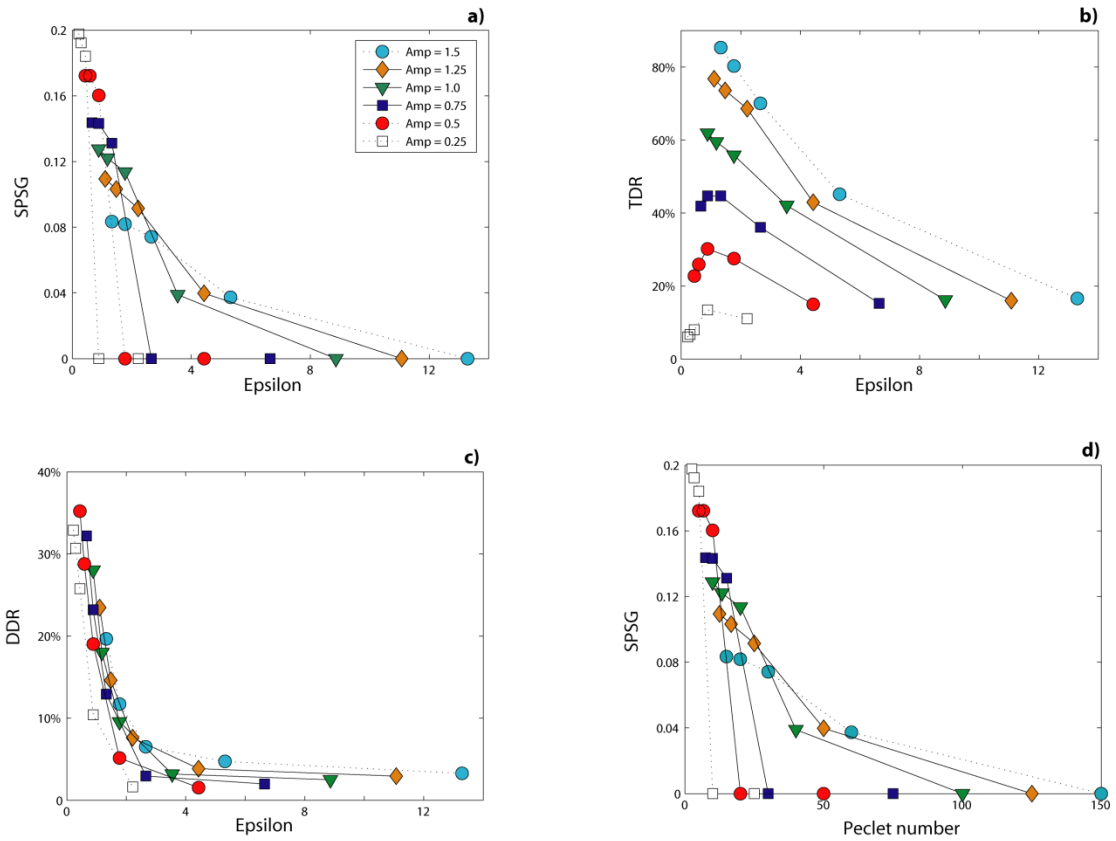

Figure 2.10. a) The ratio of horizontal shoreline excursion to tidal propagation distance (ε) versus SPSG. **b)** TDR vs. ε. **c)** DDR vs ε. **d)** Peclet number vs. SPSG. Hydraulic conductivity is 10 m/d for each case. Intertidal zone slopes (β) were 0.1, 0.075, 0.05, 0.025 and 0.01. Tidal amplitudes range from 0 to 1.5 m and transverse dispersivity was 1 m. Note that increasing slopes result in decreasing values of ε.

Chapter 3

Submarine Groundwater Discharge and Solute Transport under a Transgressive Barrier Island

3.1 Abstract

Many recent investigations of groundwater dynamics in beaches employed groundwater models that assumed isotropic, numerically-convenient hydrogeological conditions. Real beaches exhibit local variability with respect to stratigraphy, sediment grain size and associated topographic profile, so that groundwater flow may diverge significantly from idealized models. We used a combination of hydrogeologic field methods and a variable-density, saturated-unsaturated, transient groundwater flow model to investigate SGD and solute transport under Cabretta Beach, a small transgressive barrier island seaward of Sapelo Island, Georgia. We found that the inclusion of real beach heterogeneity drove important deviations from predictions based on theoretical beaches. Cabretta Beach sustained a stronger upper saline plume than predicted due to the presence of a buried silty mud layer beneath the surface. Infiltration of seawater was greater for neap tides than for spring tides due to variations in beach slope. The strength of the upper saline plume was greatest during spring tides, contrary to recent model predictions. The position and width of the upper saline plume was highly dynamic through the lunar cycle. Our results suggest that field measurements of salinity gradients may be useful for estimating rates of tidally and density driven recirculation through the beach. Finally, our results

indicate that several important biogeochemical cycles recently studied at Cabretta Beach were heavily influenced by groundwater flow and associated solute transport.

3.2 Introduction

Surface water-groundwater interactions at the land-sea interface drive significant chemical reactions and contribute dissolved metals, carbon and nutrients to the coastal ocean (Bowen et al., 2007; Burnett et al., 2003, 2001; Charette and Sholkovitz, 2002; D'Elia et al., 1981; Johannes, 1980; Krest, 2000; Paytan et al., 2006; Whiting and Childers, 1989). A major portion of these surface water-groundwater interactions occur in sandy beaches (Bokuniewicz et al., 2004; Li et al., 1999), which occupy about 75% of the world's ice-free coastlines (Brown and McLachlan, 2002). *Heiss and Michael* [2014] reviewed the four major driving forces for groundwater flow through beaches: (1) an inland hydraulic gradient and associated discharge of fresh groundwater (R. E. Glover, 1959; Kim and Hwang, 2002; Taniguchi and Iwakawa, 2004) seaward of a saline circulation cell (Boufadel, 2000; Michael et al., 2005; Robinson et al., 1998); (2) convective mixing due to density gradients between fresh and saline groundwater (Cooper, 1959; Groen, 2002; Kohout, 1960); (3) tidal pumping (Abarca et al., 2013; Li et al., 2000; Robinson et al., 2007b, 2007c; Sun, 1997; Vandenbohede and Lebbe, 2006); and (4) wave setup and swash (Bakhtyar et al., 2013; Heiss et al., 2014; Longuet-Higgins, 1983; Robinson et al., 2014; Sorensen, 2006; Xin et al., 2010; Fig. 3.1). This combination of driving forces in permeable beach sediments leads to rapid flow (0.1 – 10 m d^{-1}), which drives chemical transformations and exports dissolved constituents to the ocean (Huettel et al., 2014; Slomp and Van Cappellen, 2004).

Previous studies have reported a wide range of biogeochemical reactions in beach sediments. The mixing and chemical exchange that occurs in coastal aquifers, termed the subterranean estuary (Moore, 1998), is significant and has garnered much scientific interest. *Charette and Sholkovitz* [2002] observed iron oxide coated sands in the subterranean estuary at the freshwater-saltwater interface, where reduced pore water containing dissolved Fe(II) was in contact with oxidized seawater. These iron oxide coatings were shown to prevent phosphorus from discharging to the coastal ocean through adsorption, exemplifying the importance of groundwater mixing at the freshwater-saltwater interface for geochemical processes. *Ullman et al.* [2003] showed that beaches serve as reservoirs for particulate matter and remineralized reactive organic matter from the coastal ocean, which drives higher rates of nutrient fluxes from the beach than could be sustained by upland discharge alone. Furthermore, fluxes of dissolved organic matter and nutrients from the subterranean estuary to the coastal ocean are sensitive to tides (Santos et al., 2009). *Schutte et al.* [2015] hypothesized that a zone of rapid nitrogen cycling and subsequent nitrous oxide production in a beach in southern Georgia was controlled by periodic spring tide inundation. At the same field site, a confined aquifer system under the beach was hypothesized to facilitate methane export to the coastal ocean, but flow rates in this aquifer and the integrity of the confining unit were relatively unknown (Schutte et al., 2016). The hydraulic feasibility of these proposed groundwater dynamics in the beach requires further investigation. These biogeochemical processes, like those in other subterranean estuaries, are likely transport-limited and may be sensitive to salinity, which indicates the need for a better understanding of groundwater flow below beaches.

Groundwater salinity is simple field measurement and can be used to provide insight into the flow dynamics beneath the beach. In some beaches, two separate saline circulation cells develop: (1) The classic freshwater-saltwater interface (FSI) (Cooper, 1959; Ghyben, 1889; R. E. Glover, 1959; Henry, 1959; Herzberg, 1901); and (2) the upper saline plume (USP) (Boufadel, 2000; Lebbe, 1999; Robinson et al., 2006; Fig. 3.1). The FSI is present in all beaches and is the salinity configuration that forms at equilibrium between flowing land-derived fresh groundwater and circulating saline groundwater (Cooper, 1959; Kohout, 1964). Density-driven recirculation (DDR) of seawater into the beach aquifer occurs at this interface due to the presence of a sharp salinity gradient. The USP develops through tidally driven recirculation (TDR) of seawater into the beach above a body of discharging fresh groundwater that exits near the elevation of low tide (Boufadel, 2000; Robinson et al., 2006). The shallow beach aquifer fills with seawater during rising tide and discharges during low tide after mixing with land-derived fresh groundwater. After the initial discovery and description of the USP by *Boufadel* [2000] and *Robinson et al*. [2006], the established convention was that most beach aquifers contained a USP. Recent studies have shown that the USP may be transient in coastal aquifers and its presence is highly dependent lunar cycles, fresh groundwater head, beach slope and grain size (Abarca et al., 2013; Evans and Wilson, 2016; Heiss and Michael, 2014). The distribution of salinity in the beach is a direct consequence of the flow dynamics within the beach and can potentially be used to estimate rates of seawater recirculation (Evans and Wilson, 2016)

Evans and Wilson [2016] proposed a field measurement called the saline plume salinity gradient (SPSG) that was shown to vary with rates of TDR and DDR in

theoretical studies. The SPSG is calculated by determining the concentration gradient between two points perpendicular to the shore, 1 meter below land surface. The first measurement is made at the approximate center of the USP, and the second is collected near the center of the freshwater tube directly seaward. These locations roughly correlate with mean high and mean low water. Stronger USPs had higher SPSGs. Beaches with the strongest USPs had the highest rates of DDR (Evans and Wilson, 2016). TDR was more complex and was dependent on beach slope, tidal amplitude and inland hydraulic head (Robinson et al., 2007c). These hydraulic parameters can be simultaneously expressed in a nondimensional ratio of the width of the intertidal zone to tidal propagation distance (Li et al., 2000; Robinson et al., 2007c):

$$\varepsilon = A\cot(\beta)\lambda \qquad (3.1)$$

where A is tidal amplitude, β is beach slope and λ is the tidal propagation distance:

$$\lambda = \sqrt{\frac{n_e\omega}{2KH}} \qquad (3.2)$$

where n_e is effective porosity, ω is tidal period, K is hydraulic conductivity and H is aquifer depth. In beaches with moderate slopes (0.01 to 0.1), TDR decreased with increasing values of ε (Evans and Wilson, 2016). More interestingly, SPSG, TDR and DDR are all related to ε, which can be calculated for any beach. *Evans and Wilson* [2016] hypothesized that rates of TDR and DDR could be estimated using only a measured SPSG and calculated value for ε. Additionally, these theoretical models predicted that SPSG would be higher for lower tidal amplitudes, indicating that neap tides should support weaker USPs than spring tides. Rates of seawater recirculation should be higher during spring tides (Evans and Wilson, 2016). Although these relationships are valid in theoretical beaches, the viability of using a measured SPSG to estimate rates of TDR and

DDR in a real beach is unknown. Further study using numerical models calibrated to a real beach is required to test these hypotheses.

Most numerical studies of groundwater flow and solute transport processes in beaches assume homogenous, isotropic sand to depths as great as 30 m below land surface (Abarca et al., 2013; Ataie-ashtiani et al., 1999; Boufadel, 2000; Evans and Wilson, 2016; Heiss and Michael, 2014; Lebbe, 1999; Michael et al., 2005; Robinson et al., 2007c, 2006; Vandenbohede and Lebbe, 2006). The use of homogenous models to describe groundwater flow in beaches ignores interbedded sediments present in a large portion of the world's beaches. In addition, many of these models used a constant single slope for the intertidal zone of the beach. Real beaches have variable topography due to the dynamic impacts of waves and currents. We hypothesize that the inclusion of real-world heterogeneity in beach groundwater flow models will highlight important deviations from these theoretical models and chose a transgressive barrier island beach as a site to test this hypothesis and the potential for estimating TDR and DDR from the SPSG.

We chose a transgressive barrier island beach as a test beach because barrier islands cover 49% of the coastline of passive continental margins and are characterized by complex, heterogeneous stratigraphy (Glaeser, 1978). These environments are extremely dynamic, and their morphology is controlled by wave action and tidal energy (Hayes, 1979). As a result, the beach profile across a barrier island is non-uniform. These beaches are also commonly underlain by low permeability, silty mud from ancient marsh platforms, which could drive anisotropy in groundwater flow. We hypothesized that inclusion of a non-uniform beach profile, subsurface heterogeneity and real tidal

conditions would highlight significant deviations from theoretical conceptual models for beach groundwater flow and the USP. This hypothesis was tested using a combination of piezometer installation and hydraulic head monitoring, electrical resistivity tomography, and a two dimensional, variable-density, saturated-unsaturated, transient groundwater flow model.

3.3 Site Description

Cabretta Island is a small Holocene transgressive barrier island on the seaward side of Sapelo Island, Georgia (Fig. 3.2). The island experiences a semidiurnal tide with a range of ~2.5 m and average annual rainfall of 130 cm (Wilson et al., 2011). For the month of June 2012, mean sea-level was 0.24 m, MHW was 1.24 m and MLW was -0.93 m. The island is approximately 250 m in width by 2.1 km in length, and reaches a maximum elevation of ~3 m (MSL). The intertidal zone of the beach on the eastern side of the island has a slope of approximately 0.025. As described in *Wilson et al.* [2011], a transect extending from a tidal creek to the ocean was vibracored to depths of 3-4 m to determine the local stratigraphy in January 2008 (Fig. 3.3). On the marsh side of the island, a 1-2 m thick confining unit of marsh mud and silt was underlain by a permeable confined aquifer of fine sand. The forested upland, which was comprised of fine sand, made up the unconfined surficial aquifer. This aquifer was underlain by a low permeability confining unit made of interbedded silt and clay at approximately 2.5 m below land surface (Fig. 3.3). On the beach side, the sediments were fine sands with irregularly distributed mud and silt layers. Significant erosion of sand from the beach (~ 2 m) over this 4 year period was observed while surveying elevations in the summer of 2011. Additional vibracores were collected in the beach in February 2012. These cores revealed a confining unit made

of interbedded silts and clays at approximately 3 m below land surface on the beach. Below this confining unit was a confined aquifer comprised of fine sand. We focus this study on flow and solute transport from the forested upland, through the beach, to the ocean.

3.3.1 Biogeochemistry and Hydrogeology of Cabretta Island

Several investigations at Cabretta Island have been published in the last 6 years, but none were specific to groundwater flow in the beach. *Anderson* [2010] developed a groundwater flow model for the Cabretta Island transect, but groundwater flow dynamics and solute transport in the beach were simplified and the underlying low permeability mud layer was unknown at that time. *Wilson et al.* [2011] presented the effect of Tropical Storm Fay on groundwater dynamics at Cabretta Island but focused on the marsh side of the island. *Schutte et al.* [2015, 2016] focused on nitrogen and methane cycling on the beach side of Cabretta Island. They showed that both processes were largely groundwater transport-limited reactions. A simplified groundwater flow model was used to calculate tide-averaged flow velocities needed to calculate N_2O and methane fluxes from the beach. That model used a sinusoidal tide and annual average rainfall rate. The primary objective of the current study is to quantify seawater recirculation and to investigate the configuration of the freshwater-saltwater in the beach. A more detailed numerical model was required to accomplish these goals.

3.4 Methods

3.4.1 Field Methods

Elevation surveying was conducted in early June 2012 to collect a beach topographic profile. Precipitation records were also obtained from the nearby Sapelo Island National

Estuarine Research Reserve System (NERRS) weather station located at Marsh Landing. Tide water levels were obtained from the nearest NOAA tide gauge (Ft. Pulaski) from http://tidesandcurrents.noaa.gov. Ft. Pulaski is approximately 40 miles northeast of Sapelo Island and tidal records had a discrepancy of about -0.14 m and 27 min between our site at Cabretta and the tide gauge (Wilson et al., 2015).

As described in detail in *Wilson et al.* [2011], seven piezometer nests were installed along the transect in the summer of 2008 (Fig. 3.2). Piezometers were constructed using Schedule 40 PVC (3.2 cm) and Schedule 40 PVC slotted well screen (0.15 mm). The deeper wells had screened intervals of 30 cm and the shallow wells were 15 cm. Internal casings (2.5 cm) were installed in each well to limit wellbore storage and exchange across the screen during the tidal cycles (Wilson et al., 2011). In the salt marsh, 3 piezometers were installed at each nest (TT1-TT3), generally at depths of 1, 3 and 5 m below land surface (IE TT1-1, TT1-3, and TT1-5). Well nest TT3b was installed at the edge of the forested upland at depths approximately 1 and 3 m below land surface. At nest TT4, two piezometers were installed that were screened at depths of approximately 2 and 4 m below land surface (Fig. 3.3). TT5 was located at the top of the dunes when installed, reaching approximately 5 m below land surface. At the top of the beach, nest TT6 is comprised of 3 piezometers screened at depths 1, 3 and 5 m below land surface. The final piezometer nest (TT7) was installed near the low tide mark on the beach, comprised of two piezometers screened at 1 and 3 m below land surface respectively (Fig. 3.3). Four years of sustained beach erosion (2008-2012) led to the loss of TT6-1, TT6-3, TT7-1 and TT7-3. Three additional piezometers were installed in the beach in 2012: TT5a, TT7a and TT7b (Fig. 3.3).

Pressure loggers were installed in the wells to record water level and temperature data at 20 min intervals. A barometer was also installed at the site to correct water levels for barometric pressure. For this study, we focused on pressure data for wells TT4-2, TT5a-3, TT7a and TT7b from June 2012. Groundwater salinities were collected and compiled for all the wells at Cabretta Beach on a regular basis and are presented in *Schutte et al.* [2016].

We conducted a Wenner array resistivity 2D profile along the transect at Cabretta beach from TT3b to seaward 133 m in August 2012. Electrical resistivity is sensitive to groundwater salinity and is useful for delineating the freshwater-saltwater interface in coastal settings (Choudhury et al., 2001). The survey was conducted using an AGI Super Sting R1 automatic switchbox and a waterproof cable with 28 electrodes and 3 m electrode spacing. We measured apparent resistivities along a transect 133 m long (1 roll forward) to a target depth of approximately 9 m below land surface. The survey was conducted during low tide. The roll forward was overlapped on the mid beach by 30 m in order to increase the signal to noise ratio. Approximately 14% of the measured apparent resistivity dataset was either negative or anomalously high. Low signal-to-noise ratios in those areas were likely caused by signal attenuation in highly conductive saline pore water (beach) near the surface in the former case, and signal dampening in highly resistive dry quartz sand (upland) in the latter. These data points were discarded before performing the inversion. Inverse modeling was conducted using AGI EarthImager 2D to convert measured apparent resistivities to a 2D resistivity section (AGI, 2009).

3.4.2 Numerical Methods

Simulations of tidally influenced groundwater flow were conducted using SUTRA, which is a model for saturated-unsaturated, variable-density groundwater flow with solute transport (Voss and Provost, 2002). The governing equation for the calculations used in SUTRA is a form of the Richards equation. We modified this equation to account for changes in overlying stress associated with tidal loading (Wilson and Gardner, 2006):

$$\nabla \cdot [K(\Psi)\nabla h] = S_w S_s \frac{\partial h}{\partial t} + \varphi \frac{\partial S_w}{\partial t} - \alpha_s S_w \frac{\partial \sigma_T}{\partial t} \qquad (3.3)$$

where K is hydraulic conductivity, Ψ is negative pressure head, h is hydraulic head, S_w is water saturation, φ is porosity, σ_T is total stress and S_s is the specific storage,

$$S_s = \rho g(\alpha_s + \varphi\beta) \qquad (3.4)$$

where ρ is the density of water, g is gravity, α_s is sediment compressibility and β is fluid compressibility.

The model domain was constructed to simulate groundwater flow from the forested upland seaward through the beach (Fig. 3.4). The domain was 300 m in length, and extended from TT4, across the beach, to the nearshore environment. The surface of the domain was created using a topographic profile developed from elevation surveys, and it ranged in elevation from 2.75 to -2.5 m mean sea-level (MSL). The domain extended down through the subsurface to -10 m (MSL). Domain boundaries were chosen to ensure simulation results were not influenced by boundary effects.

A two-dimensional, finite element, irregular mesh with 16,058 nodes and 15,272 elements was used for all subsequent simulations. Elements ranged from a maximum size of 0.56 m^2 to a minimum of 0.01 m^2. Element size was refined near the surface, where

flow rates were the greatest and salinity changed rapidly, to ensure the Peclet and Courant criteria were met. Saturation fronts contained at least 5 nodes to prevent problems with numerical convergence in the unsaturated zone.

The model domain contained 3 distinct hydrostratigraphic units with respect to porosity and permeability: (1) surficial silty, fine sand of forested upland; (2) surficial, well-sorted, medium grained sand of the beach; and (3) buried, silty mud layers (Table 3.1). We tested a reasonable range of permeability values for coastal sand deposits (10^{-10} to 10^{-12} m^2), as presented in *Wilson et al*. [2008]. The permeability values used for the upland and beach sands (Table 3.1) were ultimately chosen after a sensitivity analysis was conducted to match simulated hydraulic head with observed values. The max permeability of the mud layer was determined iteratively by comparing simulated groundwater salinities of the confined aquifer to electrical resistivity results and piezometer samples. The ratio of longitudinal to transverse dispersivity was held constant at 10 (α_L= 2.5 α_T=0.25) (Gelhar et al., 1992; Smith, 2004).

The relative permeability of sediments in the unsaturated zone was calculated using the van Genuchten equation (van Genuchten, 1980):

$$S_w = S_{wr} + \frac{(S - S_{wr})}{[1+(\alpha|\psi|)^n]^m} \qquad (3.5)$$

where S_{wr} is the residual saturation of the sediment, ψ is suction pressure head, *n* and *m* are fit parameters, and α is the inverse of the capillary rise (m^{-1}):

$$\alpha = \frac{1}{h_b}\left(2^{1/m} - 1\right)^{1-m} \qquad (3.6)$$

where h_b is the air entry pressure. The fit parameters *m* and *n* are related by:

$$m = 1 - 1/n \qquad (3.7)$$

The van Genuchten parameters used in the model are presented in Table 3.1.

Boundary conditions were selected to simulate transient groundwater flow driven by tides and salinity gradients (Fig. 3.4). The western boundary was assumed to be a no-flow boundary due to the presence of a flow divide in the forested upland near well cluster TT4 (Anderson, 2010). The bottom boundary was assigned a no-flow boundary representative of an underlying low permeability layer. The eastern boundary was extended offshore sufficiently that flow rates were negligible and a no-flow boundary was appropriate. The upper boundary was assigned a combined specified fluid pressure and flux boundary condition depending on the elevation of the tide and saturation. For surface nodes that were never inundated by the tide, the boundary condition was a specified fluid flux representative of rainfall infiltration (130 cm/year). For nodes that were inundated by the tide, the boundary condition was specified according to the height of the tide (Wilson and Gardner, 2006). In order to accurately match measured hydraulic head peaks at high tide, an additional 20 cm of head was added to the tidal signal boundary condition to account for wave-runup (Nielsen, 1990). These nodes were assigned a pressure representative of the weight of the overlying column of seawater. Surface nodes that were exposed above the height of the tide and were fully saturated developed a seepage face.

Initial conditions for tidal simulations were obtained by first running a simulation without tides. Initial pressure for every node was set to be equal to hydrostatic pressure. Initial salinity was equal to 35 for the entire model domain. Salinity is reported here using the Practical Salinity Scale of 1978 (UNESCO, 1981). Mean sea level was set to the average for June 2012 (0.23 m). The simulation ran for 30 years with 3-day time steps

until quasi-equilibrium was reached. The results from this preliminary simulation were used as the initial conditions for the subsequent tidal simulations.

An initial tidal simulation using a simplified tide (sine wave) was then performed to calculate initial conditions for a final simulation. Tidal amplitude was 1.5 m and the period was 12.4 hours. This run required 550 days at 5 minute time steps to reach quasi-equilibrium with respect to pressure and salinity.

Next, a simulation was conducted using observed tide and precipitation data from June 2012 over two spring-neap tide cycles (28 days). When surface nodes were not inundated by the tide, a specified flux representative of either precipitation or evaporation was applied based on the rainfall record. During periods of no rainfall, a constant evaporation rate of 4 mm/day was applied to the surface nodes. Time steps of 1 minute were required to achieve numerical convergence during rapidly changing pressure and salinity conditions in the shallow subsurface.

Finally, we repeated this sequence of simulations with a second model domain where the buried, silty mud layers were removed and replaced with sand. The model was otherwise identical with respect to boundary conditions and hydrogeological parameters. These simulations were used to quantify the influence of the low permeability sediments on the configuration of the freshwater-saltwater interface and SGD in the beach.

The strength of the simulated USP that developed in the beach was determined by measuring a saline plume salinity gradient (SPSG) according to the method detailed in *Evans and Wilson* [2016]. In these theoretical models, the strength of the gradient is a function of density and tidally driven recirculation through the beach aquifer (Evans and Wilson, 2016).

Rates of SGD and saline water recirculation (Q_{SGR}) into the beach aquifer were measured in the tidal simulations for the month of June 2012. The total volumes of water infiltrating (Q_{TOT}) and discharging (SGD_{TOT}) from the surface boundary of the model were calculated for each time step by summing the groundwater flow velocity in each surface element and multiplying by porosity and element area. Infiltrating seawater was separated into density (Q_{DDR}) and tidally driven recirculation (Q_{TDR}) as described in *Evans and Wilson* [2016]. Q_{DDR} was seawater that infiltrated below the elevation of low tide and Q_{TDR} was seawater that infiltrated above. These fluxes were then normalized by dividing by the freshwater flux ($Q_{F)}$ and multiplying by 100 to yield TDR and DDR as percentages to remain consistent with the literature (Robinson et al., 2007c). This technique works well for idealized simulations with a sinusoidal tide and specified freshwater flux boundary condition. Q_F and the position of low tide are harder to determine in simulations calibrated to real tide data and observed hydraulic head. We categorized TDR and DDR based on the elevation of mean low water (MLW) in this study. SGD was categorized by salinity using the USGS guidelines: fresh (SGD_F) (0 to 1); brackish (SGD_B) (1 to 10); and saline (SGD_S) (> 10). This allowed SGD rates to be reported with respect to proportions of fresh/brackish/saline water. All infiltrating seawater was 34 and rainwater was 0.

3.5 Results

3.5.1 Field Data

An electrical resistivity tomography survey to a target depth of approximately -10 m (MSL) suggested the presence of a complex salinity configuration under Cabretta Beach (Fig. 3.5). The root-mean-square error (RMSE) of the inversion between the measured

and modeled resistivity was 11.5%. A small brackish-to-freshwater lens (10- 50 Ohm-m) near TT3b was modeled in the inversion under the forested upland of Cabretta Island. A brackish body of groundwater (3 -10 Ohm-m) was modeled in the confined aquifer beneath the mud layer in the beach. The unconfined aquifer in the beach was modeled to be saline (< 1.5 Ohm-m) except near the low-tide mark on the beach (TT7) where the water was slightly brackish about a meter below land surface (~3 Ohm-m) (Fig. 3.5). Using the resistivity survey and stratigraphic data, we interpreted the groundwater system to be strongly influenced by the presence of a buried mud/silt layer under the forested upland and beach. Fresh groundwater from the upland is diverted below the surficial beach aquifer, into the confined aquifer, where it discharges near the elevation of low tide on the beach. In order for fresh groundwater from the forested upland to flow into the confined beach aquifer, the confining mud layer must be incised somewhere beneath the freshwater lens. We estimated that this break in the confining unit was located approximately beneath the upper beach, near TT5a (Fig. 3.3).

Groundwater salinity was periodically sampled from the wells along the transect from September 2011 through the summer of 2012 (Table 3.2) Wells in the forested upland and dune field were fresh to brackish, wells in the mid beach were saline, and wells near the average elevation of low tide were still saline, but slightly fresher (~24). No fresh groundwater was measured below the beach during our study. Groundwater in the confined beach aquifer below the mud layer in the beach was sampled in the winter of 2012, between wells TT5 and TT6. We measured the salinity to be approximately 25, but the well was abandoned the same day after it filled with silt.

Hydraulic head records for wells TT4-2, TT5a-3, TT7b and TT7a for the month of June 2012 showed that variability in groundwater levels was mostly driven by daily tidal pumping and the spring/neap cycle (Fig. 3.6). TT4-2 was outside the propagation distance of the tidal energy. Thus hydraulic head was controlled by freshwater flux, drainage and evapotranspiration only. Water levels in the beach wells were approximately ~0.2 m higher than the elevation of the tide at high tide (Fig. 3.6). As previously indicated, this surplus head was most likely driven by wave-runup on the sloping beach face of the intertidal zone (Nielsen, 1990). The magnitude of the hydraulic gradient between the wells was greatest during falling and low-tide, when the majority of groundwater flow occurred in the beach. However, large spring tides and dry conditions during the first week of the month nearly reversed the hydraulic gradient over the transect at high tide. Hydraulic head at well TT7a was slightly higher than the head at well TT4-2, and was 30-50 cm greater than the head at TT5a-3 (Fig. 3.6).

3.5.2 Numerical Model Calibration

We calibrated the groundwater model to salinity measured in the field by adjusting permeability values for the hydrostratigraphic units (Table 3.1; 3.2). In general, our model successfully reproduced observed groundwater salinities from the piezometers at Cabretta Beach. The largest difference between simulated and observed groundwater salinity was at well TT4-4 (~3.8). Deviations between simulated and observed groundwater salinities were all within a reasonable range of variability for a beach system. The distribution of groundwater salinity in the beach model was mostly controlled by the permeability of the buried, silty mud layers, for which a value of 5 x 10^{-}

^{15} m^2 best reproduced the observed salinities. This permeability was also required to accurately simulate groundwater head in the forested upland region of the model.

We also attempted to calibrate the model to observed hydraulic head data. Due to the dynamic nature of the beach at Cabretta Island, we estimate that our measurements of elevation were accurate to within ± 25 cm for the study period. Highly precise calibration between simulated and measured hydraulic head was not possible. The average head at well TT4-2 over the study period was 1.85 m, with two prominent peaks above 2 m during periods of sustained rainfall (Fig. 3.7a). A permeability of 1 x 10^{-14} m^2, representative of silty sand, was required to sustain this head at the western boundary of the model. The location of well TT4 was a boundary node in our model. Minor edge effects caused the model to be less sensitive to precipitation at TT4 than the measured data suggested. There may have also been a discrepancy between the actual rainfall at the field site and the rain gauge, which was located approximately 2 miles away. A permeability of 5.8 x 10^{-11} m^2 best reproduced hydraulic head at well TT5a. Simulated and measured hydraulic head were in close agreement except for a period of approximately 7 days, where the model results under-predicted head during low tide (Fig. 3.7b). The modeled results were slightly higher during the first few high tides of the month compared to the field data (Fig. 3.7b). These differences were probably caused by a small discrepancy between the actual elevation of land surface and that used in the model, which affected the location of well TT5a in the tidal frame.

Groundwater head for beach wells TT7a and TT7b was calibrated using a permeability of 5.8 x 10^{-11} m^2 (Fig. 3.7c-d). We were unable to reproduce the troughs in hydraulic head during periods of no rainfall in the measured data (Fig. 3.7c-d). Van

Genuchten fit parameters did not impact the model significantly enough to reproduce the observed head at low tide. Results were much more sensitive to permeability. In order to force the model to reproduce the measured hydraulic head at low tide, a permeability of 9 x 10^{-10} m^2 was required. This value is unrealistic for a beach with a median grain size of approximately 0.3 mm. Test simulations that reached quasi-equilibrium using this permeability in the beach resulted in uniform groundwater salinities of 34 throughout the entire domain in the tidal range. We propose that the discrepancy between the measured and simulated hydraulic head at low tide was caused by uncertainty in the total thickness of overlying sediment above the screened interval of the well (erosion), uncertainty in elevation datum, and evaporation in the beach during periods of drought. Although the model was unable to exactly reproduce the observed hydraulic head data for the lower beach, the general impact of spring/neap tides and precipitation on groundwater flow was captured.

3.5.3. Model Results

Our simulation results showed that a moderate strength USP developed under the upper beach around mean high water (MHW), adjacent to a zone of slightly fresher, but still saline groundwater discharge at the elevation of mean low water (MLW). A standard FSI developed seaward of this zone of discharge (Fig. 3.8a). The salinity of the groundwater within the upper saline plume was approximately 31.5, and the salinity of the groundwater that discharged near MLW was 24. The average SPSG (Evans and Wilson, 2016) for June 2012 was 0.075 (Table 3.3) No fresh groundwater was present under the beach, existing only in the freshwater lens beneath the upland.

Groundwater flow paths were greatly impacted by subsurface heterogeneity. In general, groundwater flowed downward under the forested upland and into the confined aquifer where it mixed with saline groundwater and eventually discharged at the terminus of the silty mud layer (Fig. 3.8b). Some groundwater discharged slightly above the elevation of the highest spring tides, near well TT5a (x = 25 m). Above the confining unit in the beach, a flow divide developed between wells TT5 and TT6, at the approximate elevation of MHW (Fig. 3.8b). West of this flow divide, infiltrating seawater flowed slightly landward, where it eventually flowed downward and through the break in the confining unit and mixed with fresh groundwater from the upland. East of the divide, groundwater flowed rapidly seaward and discharged at changes in beach slope and at the elevation of MLW. Density-driven convection drove seawater to infiltrate the subsurface seaward of the FSI (Fig. 3.8b). Groundwater flow ranged from 1 to 2 cm/day in the forested upland, 5 to 100 cm/day in the permeable beach sands, 1 to 2 cm/day in the silty mud layers, and less than 1 cm/day offshore where the sediment surface was always inundated by the sea (Fig. 3.8b).

We calculated total fluxes of SGD and SGR from Cabretta Beach. The total volume of SGD over a single tide was 5.7 m^3 per meter of shoreline (Table 3.3). The total volume of seawater to infiltrate the beach aquifer over one tide (Q_{SGR}) was 2.6 m^3 per meter of shoreline (Table 3.3). Recirculated seawater accounted for approximately 46% of the total SGD from Cabretta Beach in one tide. The remainder originated as fresh water that became saline through mixing below the beach.

Simulation results for the month of June 2012 were further examined with respect to the spring/neap lunar cycle. A large spring tide occurred during the first week of June,

reaching MHHW of approximately 1.5 m and MLLW of -1.3 m. Groundwater salinities and flow velocities were averaged over the spring tide period (Table 3.3; Fig. 3.9a). Impacted by the higher high tides associated with the spring lunar cycle, the center of the upper saline plume was transported up the beach approximately 10 m and was shortened about 35% compared to the June 2012 average. The salinity of the center of the upper saline plume increased from about 31.5 to 32.7, and the salinity at the seepage face near MLW decreased slightly to 24. The width of this seepage face increased 200% (10 to 30 m) for the spring tide cycle compared to the month average (Fig. 3.7a; Fig. 3.9a). The location of the FSI did not change. The magnitude of the SPSG increased from the month average of 0.075 to an average of 0.084 for the spring tide cycle.

Groundwater flow directions for the spring tidal cycle were mostly unchanged when compared to the monthly average results. The only significant change was a landward shift of the flow divide in the upper beach approximately 10 m, from MHW to MHHW (Fig. 3.9a). Groundwater flow velocities increased significantly during spring tides in the upper beach and confined beach aquifer. Shallow groundwater flow above the buried mud layer in the beach increased from an average of about 30 – 60 cm/day to 60-100 cm/day. Velocities in the confined beach aquifer increased from an average of about 40 cm/day to approximately 65 cm/day (Fig. 3.9a).

Following the spring tide cycle, a neap tide cycle lasted through the second week of June 2012. During this period, MHW decreased to about 0.9 m and MLW increased to about -0.75 m. Groundwater salinities and flow velocities were averaged over the neap tide cycle and reported (Table 3.3; Fig. 3.9b). Driven by the shift in the tidal range, the center of the USP migrated down the beach approximately 15 m compared to the spring

tide location (~5 m below the month average). The total width of the USP increased 40% (~10 m) from the spring tide and salinity remained constant (Fig. 3.9b). The salinity in the upper 1 m of the seepage face adjacent to the USP increased by about 2 as compared to the spring tide. The location of the FSI did not change. The magnitude of the SPSG decreased from 0.084 for the spring tide cycle to 0.072 for the neap cycle (Table 3.3).

Groundwater flow paths for the neap tide cycle were unchanged compared to the spring tide results except that the flow divide in the upper beach migrated seaward approximately 15 m (Fig. 3.9a-b). Groundwater flow velocities decreased significantly compared to the results for the spring tide cycle in the upper beach and confined beach aquifer. Above the confining mud layer, groundwater velocities decreased from approximately 60-100 cm/day for the spring tide cycle to about 20-50 cm/day for the neap cycle (Fig. 3.9b)

Total fluxes of SGD and SGR were calculated through the spring/neap tide cycle (Table 3.3). The SGD flux during a spring tide cycle at Cabretta Beach was 5.8 m^3 per meter of shoreline per tide. Over 99% of this SGD was saline groundwater. The total volume of Q_{SGR} over a single tide was 2.5 m^3 per meter of shoreline. Recirculated seawater accounted for approximately 43% of the total SGD during this period. The SGD flux during the neap tide cycle at Cabretta Beach was 5.5 m^3 per meter of shoreline per tide. Virtually the entire volume of SGD was saline. Brackish and fresh groundwater discharge made up less than 1% of the total SGD. The total volume of Q_{SGR} was 2.7 m^3 per meter of shoreline per tide. Recirculated seawater accounted for approximately 49% of the total SGD over the neap cycle.

The configuration of the freshwater-saltwater interface was significantly different when the buried silty mud layers were removed (Fig. 3.10a). Most notably, the depth to which the USP extended beneath the beach surface increased approximately 4 m. The width of the USP beneath the beach remained the same, approximately 90 m. Beneath the forested upland, the freshwater lens extended the entire depth of the model domain. Groundwater salinities were overall much higher for the simulation without confining units. The average salinity of groundwater in the center of the USP was approximately 33 and the salinity in the adjacent seepage face near MLW was 28. The location of the FSI remained around x = 150 m. The average SPSG over the simulation was 0.063 (Table 3.3).

Groundwater flow paths were also significantly different for the simulation without buried mud beneath the beach. Average groundwater flow paths for the month showed a large convection cell across the freshwater-saltwater interface that developed approximately below the dune ridge (x = 20 m) (Fig. 3.10b). This convection reversed the direction of groundwater flow beneath the forested upland from downward to upward, where it eventually discharged on the high beach (x = 25 m). Slightly seaward of this seepage face, a large tidally-driven circulation cell developed where groundwater generally flowed downward from the upper beach and discharged near the elevation of MLW (Fig. 3.10b). The flow divide that was present in the previous simulations did not develop here, suggesting this phenomenon was controlled by the presence of a buried mud layer beneath the beach. Groundwater flow velocities were relatively similar in the two simulations for the forested upland, shallow beach subsurface and offshore. Beneath

the beach, velocities were higher (75 – 100 cm/d). Total volumes of SGD and SGR were very similar whether the mud layer was included or not (Table 3.3).

The flux of seawater that infiltrated the beach aquifer over the month of June 2012 was separated into tidally driven and density driven recirculation (TDR and DDR) (Table 3.3). We only report average values for the month of June 2012 for the simulations with and without a buried mud layer. For the simulation containing the buried mud layer, Q_{TDR} into the beach over a single tide was 1.8 m^3 per meter of shoreline. Q_{DDR} was 0.8 m^3 per meter of shoreline per tide. Normalized using $Q_{F,}$ TDR and DDR were 60% and 25% respectively. Q_{TDR} and Q_{DDR} were 1.9 and 0.6 m^3 per meter of shoreline per tide for the simulation without the mud layer. Normalized using Q_F, TDR and DDR were 64 % and 21% respectively. TDR increased slightly in the simulation without the buried mud, which drove a decrease in the magnitude of the SPSG. DDR also decreased in this simulation due to a lower salinity gradient in the beach.

3.6 Discussion

Accounting for heterogeneities in a beach groundwater model caused significant deviations from results based on theoretical studies involving only uniform, isotropic beach sand, and a constant beach slope. Real beaches, especially on barrier islands, contain buried layers of silt and mud in the shallow subsurface, and they have a variable topographic profile. Multiple slopes along the beach profile caused mean sea-level to fall asymmetrically on the beach surface between MHW and MLW. At Cabretta Beach, this asymmetry resulted in neap tides encountering a slightly higher average intertidal zone slope (~0.3) than spring tides (~0.25). Beach slope in the intertidal zone is an important control on the strength of the USP and on rates of TDR and DDR. We found subsurface

heterogeneity at Cabretta Beach also controlled the development of a complex freshwater-saltwater interface.

Cabretta Beach supported a wide, dispersed, moderate-strength USP (SPSG = 0.075) with an average beach slope of approximately 0.03. Based on estimates from *Evans and Wilson* [2016], a theoretical beach similar to Cabretta Beach should contain a weaker USP. A beach with a SPSG of 0.075 required a beach slope of approximately 0.05. The strength of the plume was enhanced because the relict marsh mud layer under the beach decreased mixing between tidally-driven infiltrating seawater and the land-derived groundwater below. This confined aquifer system under the beach also permitted fresher groundwater to discharge near the elevation of MLW. Therefore, the inclusion of geologic heterogeneity in the shallow subsurface of the beach increased the strength of the USP actually supported under Cabretta Beach.

The inclusion of a realistic topographic profile in numerical simulations also led to deviations from theoretical predictions for groundwater flow associated with tidal amplitude and spring/neap tidal cycles. Spring tides at Cabretta Beach during June 2012 had tidal amplitudes of approximately 3 m, and neap tides about 2 m. Using theoretical predictions from the literature as guidelines, spring tides should have higher rates of SGR (sum of Q_{TDR} and Q_{DDR}) into the beach than neap tides, and spring tides should have a lower SPSG (weaker upper saline plume). However, our results indicated the contrary: spring tides had a slightly lower flux of SGR into the beach, and a higher SPSG. This deviation was caused by variation in slopes across the beach profile at Cabretta. TDR and DDR increase with increasing beach slope when beach slopes are less than or equal to 0.1 (Evans and Wilson, 2016). The total flux of SGR increased at Cabretta Beach during

neap tides because the average slope of the intertidal zone for neap tides was slightly higher than it was during spring tides. Furthermore, the magnitude of the SPSG was lower for neap tides even though the tidal amplitude decreased.

The location of the freshwater discharge tube (FWT) is controlled by the elevation of MLW, which is a product of the average elevations of low tide through the semi-diurnal and spring/neap tidal cycles. The average elevation of low tide during the neap cycle was only slightly further down the beach than the position of the FWT. During spring tides, low tide was nearly 50 m further down the beach. Therefore, the location of the FWT on the beach was inundated by the sea for a longer portion of the tidal cycle during neap tides than during spring tides. This more frequent inundation period and associated SGR increased the salinity in the FWT, which decreased the magnitude of the SPSG. If the tidal amplitude were to remain equal to the neap tide amplitude (2 m), the system would re-equilibrate and the position of the FWT would shift landward, and the resultant SPSG would likely be higher. The neap tidal period of one week is not long enough to induce this change. The position of the FWT and USP in the beach are the product of the combination of dynamic tidal cycles and beach topographic profile. Clearly a difference exists between theoretical beach models with a static tidal amplitude and uniform beach slope, and beach models that include these heterogeneities.

Although our results suggest that theoretical numerical models of groundwater flow may not fully capture the dynamic processes that occur in beach aquifers, they are still very useful for providing broad, general predictions for SGD. The SPSG in Cabretta Beach was approximately 0.075 for the month of June 2012. According to *Evans and Wilson* [2016], a SPSG of 0.075 would lead to a value of approximately 3.5 for the ratio

of the width of the intertidal zone to tidal propagation distance (ε) in a beach, given a tidal amplitude of 1.25 m and a hydraulic conductivity of 10 m/d. Furthermore, their study suggested that a value of 3.5 for ε would result in a TDR of ~55% and a DDR of ~9%. Our model results indicate that for the month of June 2012, TDR and DDR were equal to 60% and 25% respectively. Although not perfect, these results for TDR and DDR in Cabretta Beach are similar to what *Evans and Wilson* [2016] predicted using theoretical, numerically convenient beaches. The magnitude of ε decreases with increasing values of hydraulic conductivity, which could explain why the predicted theoretical values for TDR and DDR are lower than those calculated in this study. *Evans and Wilson* [2016] used a hydraulic conductivity of 10 m/d. We found a hydraulic conductivity of ~50 m/d ($k = 5.8 \times 10^{-11}$ m^2) to best represent Cabretta Beach. These comparisons suggest that first-order estimates for TDR and DDR could be obtained using a simple field measurement in the beach and the numerical relationships of *Evans and Wilson* [2016] and *Robinson et al.* [2007b].

Our results indicate that the average SGD flux for Cabretta Beach is equal to approximately 5.7 m^3 per meter of shoreline per tide. Expanded to the total coastline length of Sapelo Island (22 km), the SGD flux is approximately 2.6×10^5 m^3/d. Georgia has a total coastline length of approximately 160 km, which suggests a total SGD flux of approximately 1.9×10^6 m^3/d. To put this volume of water into context, the Altamaha River, which discharges to the Atlantic Ocean just south of Sapelo Island, has an average discharge of 1.8×10^7 m^3/d (USGS 84 year mean statistic). This river is the third largest contributor of freshwater to the Atlantic from eastern North America (Frangiamore and Gibbons, 2016). When compared directly, SGD from the beaches of Georgia contribute

approximately 10% as much water to the Atlantic as the Altamaha River. The average width of the beaches on Sapelo Island is about 200 m, and the length of shoreline is about 22,800 m. This gives a total beach surface area of about 4.6 km^2. The total area of the Altamaha River drainage basin is about 36,000 km^2. When accounting for total discharge per unit area, the beaches of Sapelo Island discharge approximately 120 times more water to the Atlantic Ocean than the Altamaha River (~6 x 10^{-2} $m^3/m^2/d$; ~5 x 10^{-4} $m^3/m^2/d$). Beaches clearly have the potential to discharge large volumes of water to the coastal ocean that could have significant impacts on nearshore chemistry and biogeochemical cycles.

Groundwater dynamics at Cabretta Beach moderated significant biogeochemical processes (Schutte et al., 2015, 2016). Our results support the published hypothesis that a nitrous oxide hotspot on the upper beach at Cabretta was supported by infrequent inundation by high spring tides (Schutte et al., 2015). This zone became unsaturated during neap tidal cycles, when the concentration of N_2O decreased. During high spring tides, this zone was recharged with a mixture of infiltrating seawater and fresh groundwater from the upland that could potentially supply enough NO_3^- to maintain rates of N_2O production (Schutte et al., 2015). Moreover, *Schutte et al.* [2016] showed that methane export from a zone of methanogenesis in the freshwater lens under Cabretta Island was largely controlled by methanotrophy in the buried coastal sediments. They showed that in the unconfined, surficial aquifer of the beach, rates of methanotrophy were high enough to act as a sink for CH_4, preventing significant export to the ocean. They indicated that a more plausible transport pathway for CH_4 to the coastal ocean was down through the confined aquifer buried under the beach. *Schutte et al.* [2016] used a

groundwater flow velocity estimate from a previous version of the Cabretta groundwater flow model that predicted an average flow rate (~0.025 m/d) in the confined beach aquifer. This model did not include a break in the confining unit, and as a result, groundwater flowed much more slowly beneath the beach. They used this velocity to calculate an average residence time of greater than 10 years. Our new results suggest a much higher representative average flow velocity in the beach confined aquifer of ~0.4 m/day, and an average residence time of closer to 1 year. Higher velocities and therefore a shorter residence time could allow the confined aquifer under the beach to export higher concentrations of CH_4 to the coastal ocean than previously considered.

Although we attempted to calibrate our numerical model to data collected in the field as closely as possible, truly verifying and validating a numerical model of natural Earth systems in not possible (Oreskes et al., 1994). As a result, numerical models at their best can only provide a rough conceptual framework for groundwater dynamics and SGD fluxes at the coast. Real beach systems can exhibit extreme local heterogeneities with respect to the subsurface sedimentology, topographic profile, sediment transport, and dynamic forces such as waves, tides and storms, which could potentially drive extreme variability in local groundwater flow systems. As a result, numerical models are useful mostly for providing best estimates of how beach groundwater systems behave despite the inherit assumptions and non-uniqueness that models themselves contain. However, SGD is extremely difficult to measure in the field, especially at large spatial scales, and numerical models currently provide one of best methods for quantifying these fluxes.

3.7 Conclusion

We found that a calibrated numerical model of beach groundwater flow that included observed heterogeneities, such as layered stratigraphy and variable beach topography, differed in some ways from conceptual models developed using theoretical, numerically convenient beaches only. Real beaches are unlikely to be comprised solely of isotropic, well-sorted permeable sands to depths of 10-30 m, or to have uniform slopes. At Cabretta Beach, a buried, silty mud layer allowed the beach to support a stronger USP than a similar beach that consisted of only permeable sands. Variations in slope across the beach profile allowed slightly larger fluxes of SGR to occur during neap tides than during spring tides. The elevation of mean sea-level did not fall symmetrically between MHW and MLW on the surface of the beach, which caused significant variability in the size and extent of the upper saline plume between spring and neap tidal cycles. This asymmetry is probably common in real beaches.

Our results show that Cabretta Beach had an average flux of 5.7 m^3 per meter of shoreline per tide for the month of June 2012. Virtually all of this SGD to the coastal ocean was saline. The average flux of SGR was 2.6 m^3 per meter of shoreline per tide, and approximately 69% of this flux was due to TDR and 31% was due to DDR. After replacing the buried mud layer with permeable sand, the total SGD and SGR fluxes were constant, but TDR increased 4% and DDR decreased 4%. This shift in the proportions of TDR and DDR that made up the total SGR was consistent with a decrease in the magnitude of the SPSG.

Additionally, we note that our results support the hypothesis in *Evans and Wilson* [2016] that a simple field measurement (SPSG) could be used to develop preliminary

estimates for SGD and SGR in a beach. We found the calibrated Cabretta Beach groundwater model results to be very similar to the predicted values for the SPSG, TDR/DDR, and ε in *Evans and Wilson* [2016] for theoretical beaches with similar hydrologic properties. Although our results were in close agreement with studies using theoretical beaches only, more extensive investigation into the reliability of using SPSG measurements to calculate rough estimates for TDR/DDR fluxes is required.

Finally, our results confirmed that flow systems hypothesized to support biogeochemical cycling are hydrologically feasible. Our results support a conceptual model in which flow through a dynamic unsaturated-saturated zone under the upper beach, which was controlled by the spring-neap tidal cycle, could allow rapid nitrogen cycling and subsequent nitrous oxide production to occur (Schutte et al., 2015). This N_2O hotspot was located at the interface between land-derived meteoric groundwater and seawater that infiltrated the shallow subsurface during high spring tides. Additionally, the confined aquifer beneath the beach potentially facilitated transport of CH_4 from a zone of high methanogenesis under the island upland, out to the coastal ocean (Schutte et al., 2016). We calculated average flow rates through the confined aquifer of approximately 0.4 m/d, which resulted in a revised residence time calculation of approximately 1 year. This lower residence time could result in higher fluxes of CH_4 from the beach to the coastal ocean. Our results from Cabretta Beach suggest that important biogeochemical cycles in coastal sediments are largely influenced by the complex groundwater flow dynamics under the beach.

Table 3.1. Model parameters used for Cabretta Beach.

Model Parameter	Upland Silty Sand	Beach Sand	Silty Mud Layer
Porosity φ	0.35	0.425	0.7
Permeability k (m^2)	1×10^{-14} (5×10^{-15}- 5×10^{-12})*	5.8×10^{-11} (1×10^{-11} – 9×10^{-10})*	5×10^{-15} (1×10^{-16} – 1×10^{-14})*
Longitudinal Dispersivity α_L (m)	2.5		
Transverse Dispersivity α_T (m)	0.25		
Van Genuchten Fit Parameters m, n	0.875, 8	0.6, 2.5	Never exposed
Capillary Rise α (kPa^{-1})	9.5×10^{-5}	1.0×10^{-4}	Never exposed

*Range of values tested

Table 3.2. Salinity measurements for Cabretta Beach. For the *Schutte et al.* [2016] column, values represent the median, followed by the interquartile range in parenthesis.

Location	Depth msl (m)	*Schutte et al. 2016*	Field Data	Model Data *(June 2012 Average)*
TT4	0.97	1.0 (0.8-1.1)	1.5 *(9/16/11)*	0.0 (-1.5)
TT4	-1.01	3.8 (3.1-6.4)	-	0.0 (-3.8)
TT5a	1.36	-	26.0 *(7/2/12)*	25.0 (-1.0)
TT5a	-0.39	-	27.5 *(7/2/12)*	25.5 (-2.0)
TT5	0.38	4.7 (4.4-4.9)	33.6 *(11/15/12)*	30.8 (-2.8)
Confined Beach Aquifer	-2.1	-	25.2 *(2/3/12)*	26.0 (+0.8)
TT6	-0.94	22.1 (16.2-26.3)	31.5 *(9/16/11)*	32.0 (+0.5)
TT7b	-0.29	-	28.3 *(7/2/12)*	31.5 (+3.2)
TT7a	-0.65	-	29.5 *(7/2/12)*	30.2 (+0.7)
TT7	-1.97	22.3 (21.0-24.0)	27.2 *(7/2/12)*	28.6 (+1.4)
Ocean		32.0 (30.7-34.0)	35.7 *(7/2/12)*	34.0

Table 3.3. Volumetric fluxes, tidally driven and density driven recirculation (TDR/DDR), and saline plume salinity gradient (SPSG) for each simulation. Fluxes are in units of cubic meters per meter of shoreline per tide *($m^3/m/tide$)*.

	Spring Tide	Neap Tide	June 2012	No Mud
Q_F	3.2	2.9	3.1	3.1
Q_{SGR}	2.5	2.7	2.6	2.6
SGD_F	2.2×10^{-2}	9.9×10^{-3}	2.02×10^{-2}	8.9×10^{-3}
SGD_B	4.7×10^{-3}	2.4×10^{-3}	7.3×10^{-2}	3.2×10^{-3}
SGD_S	5.8	5.5	5.6	5.6
Q_{TOT}	5.7	5.6	5.7	5.7
SGD_{TOT}	5.8	5.5	5.7	5.7
Q_{TDR}			1.8	1.9
Q_{DDR}			0.8	0.6
TDR (%)			60	64
DDR (%)			25	21
SPSG (unitless)	0.084	0.072	0.075	0.069

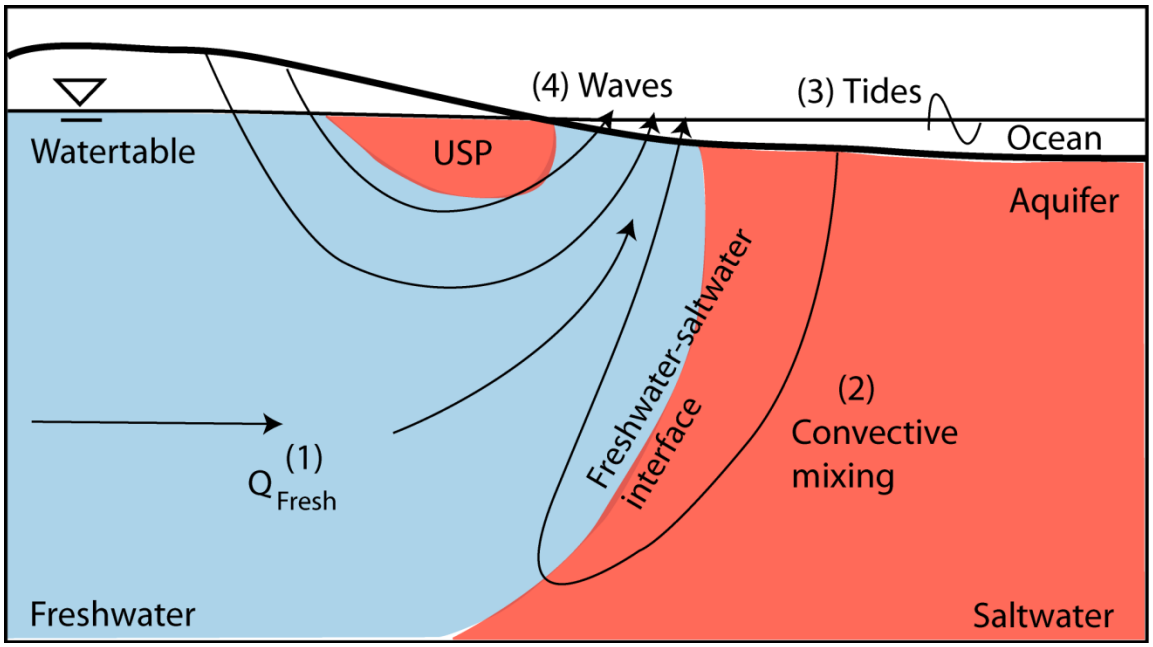

Figure 3.1. Conceptual model of the driving forces for groundwater flow under a beach.

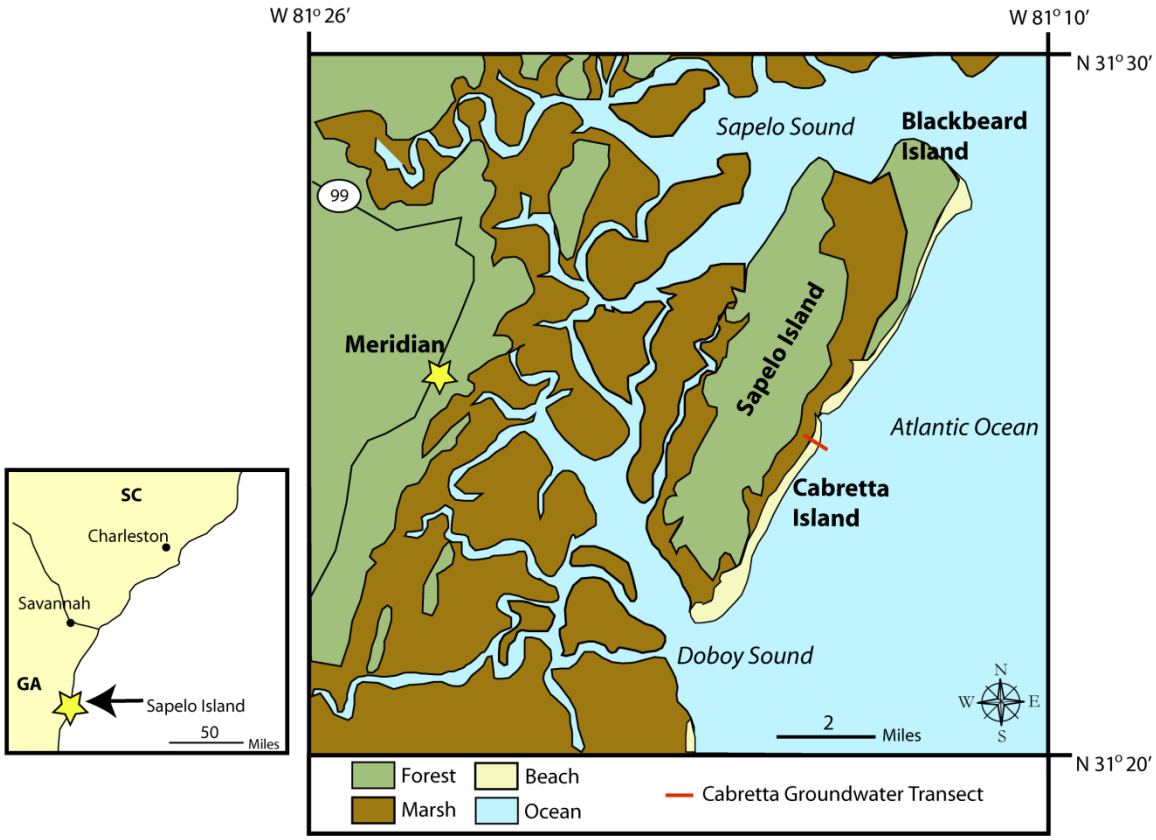

Figure 3.2. Location map of Sapelo Island and adjacent Cabretta Island, Georgia. The red line indicates the location of the Cabretta Island groundwater transect.

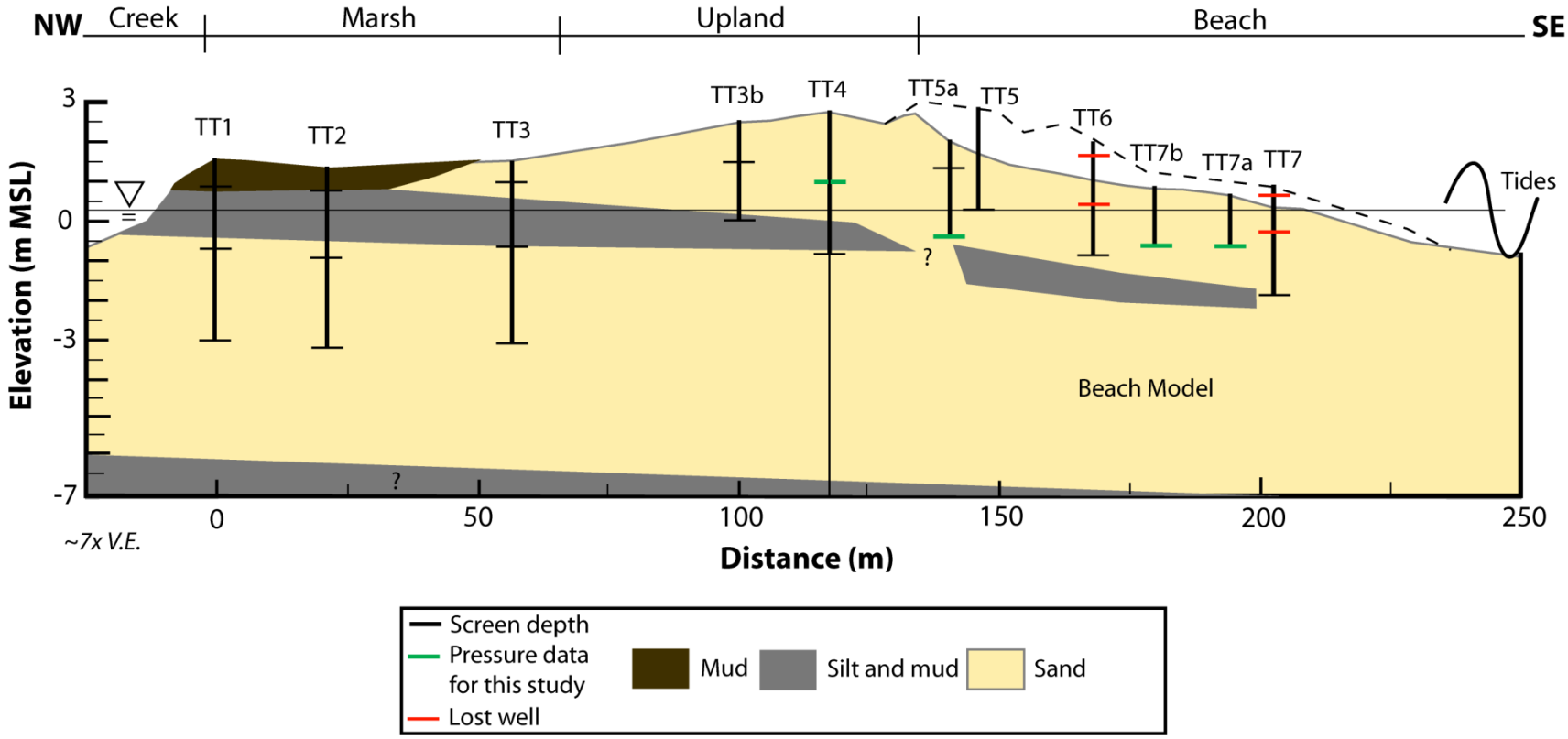

Figure 3.3. Stratigraphic cross section showing well locations and sediment types under Cabretta Island. This study focuses on the beach side of the transect, east from well TT4 to offshore. The dashed line represents the topographic profile of Cabretta Beach reported in *Wilson et al.* [2011]. Green lines represent the wells and associated data that were used in this study. Red lines represent wells that were lost to beach erosion.

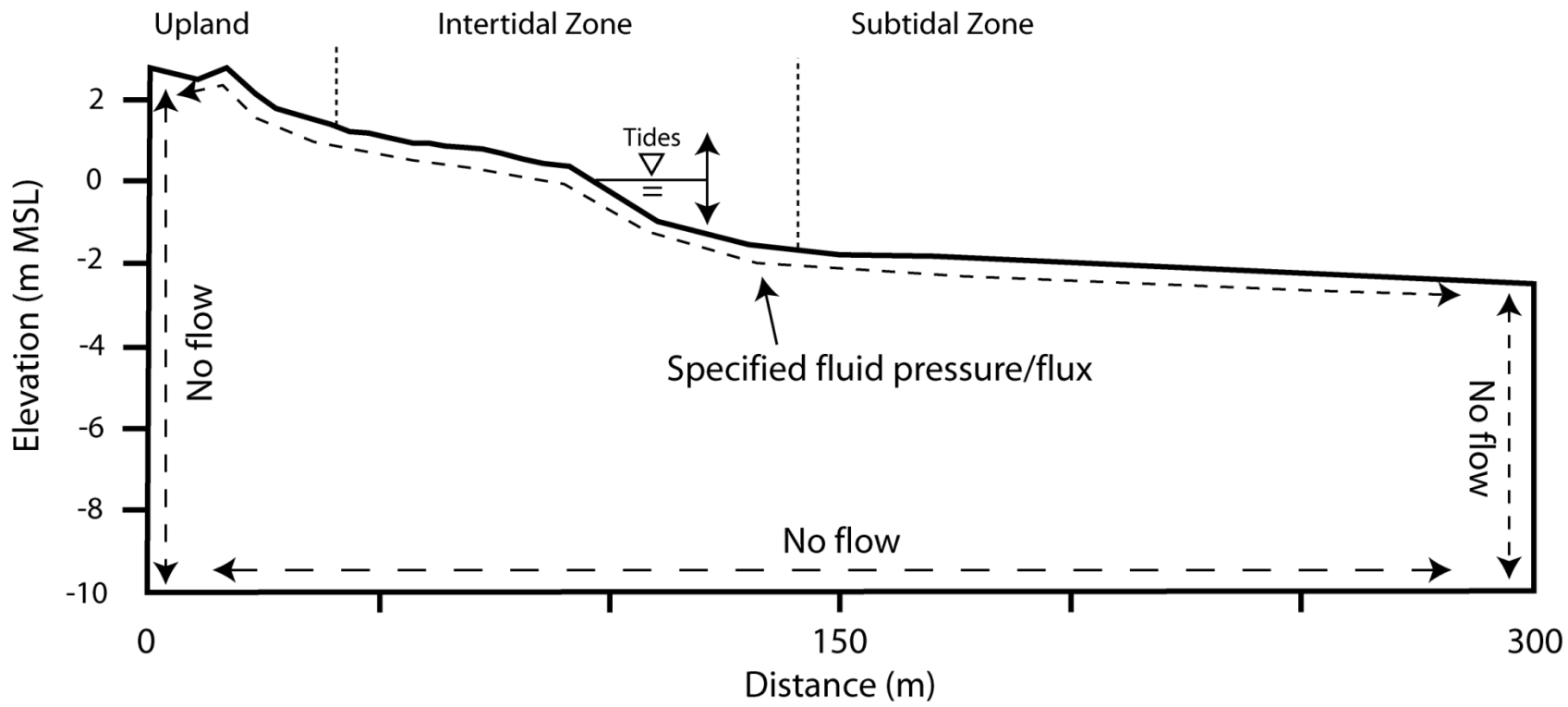

Figure 3.4. The Cabretta Beach groundwater model domain and boundary conditions.

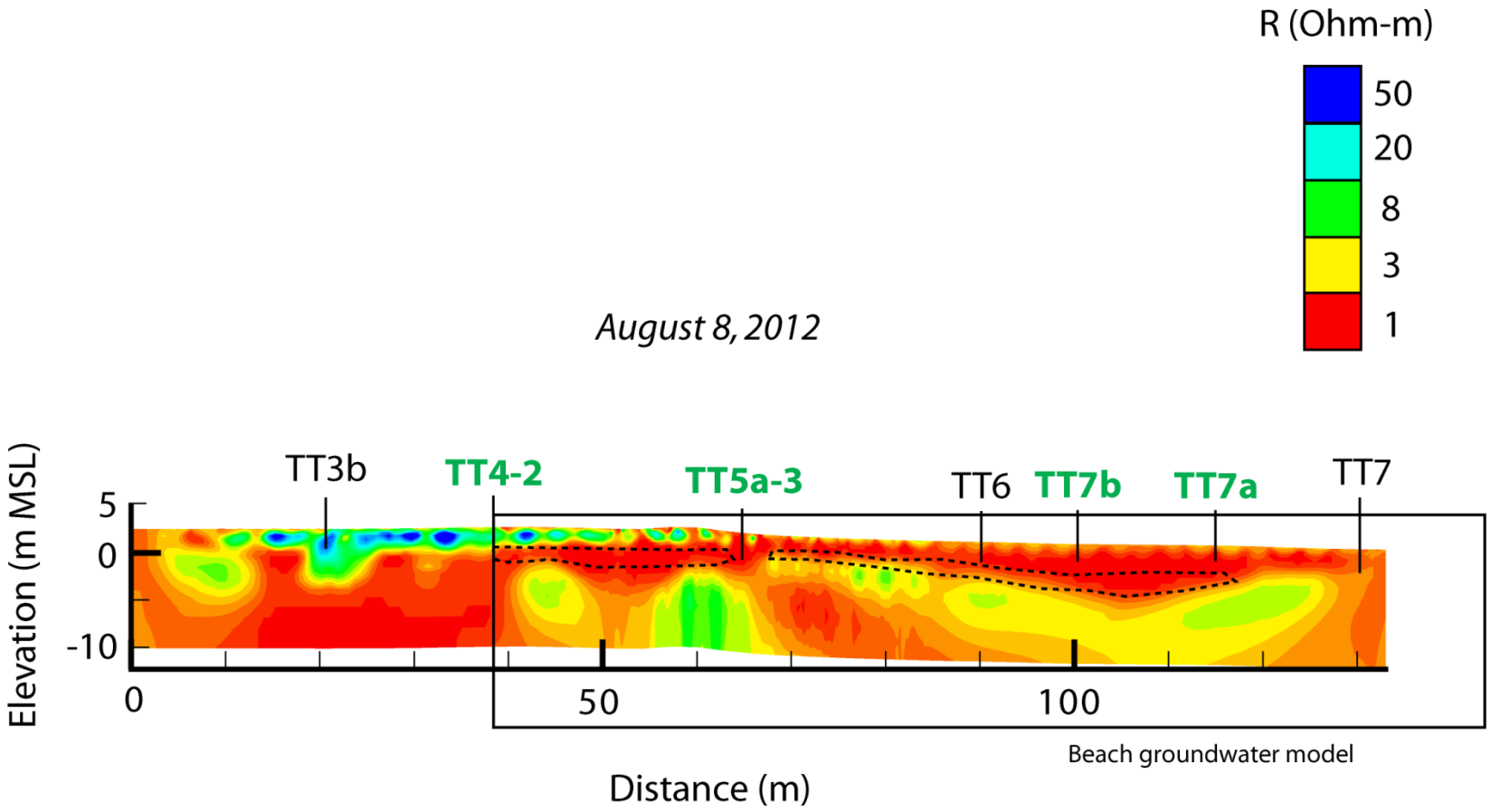

Figure 3.5. Electrical resistivity tomography results from Cabretta Beach at low tide on August 8, 2012. Warm colors represent low apparent resistivity and therefore more saline groundwater. Cool colors represent high apparent resistivity and therefore brackish or fresh groundwater. The box represents the extent of the Cabretta Beach groundwater model and the dashed line represents the location of the mud layer beneath the beach. For this study, we used data from wells TT4-2, TT5a-3, TT7b and TT7a. RMSE = 11.5%.

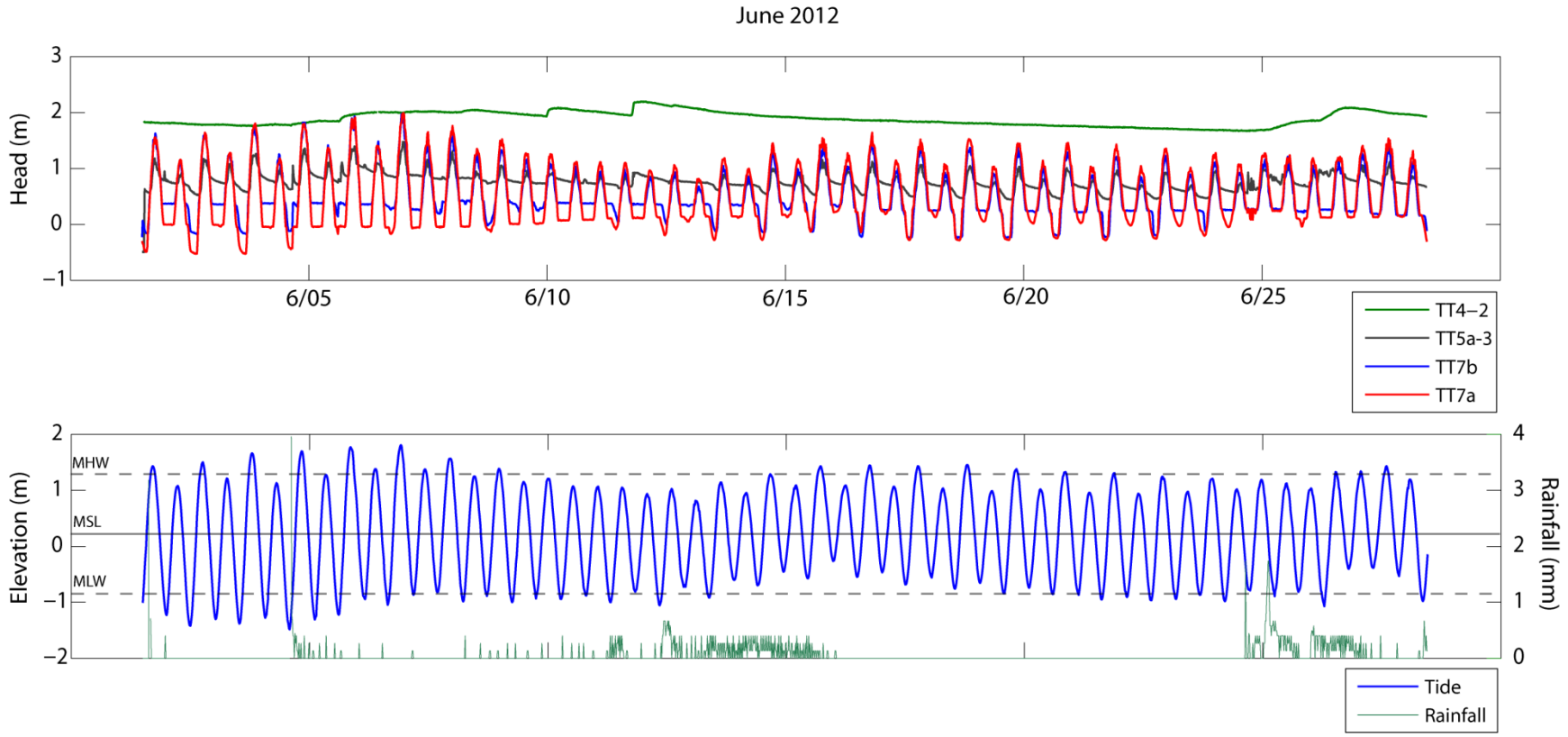

Figure 3.6. Field hydraulic head data for wells TT4-2, TT5a-3, TT7b and TT7a, tidal height, and precipitation data for the month of June 2012 at Cabretta Island.

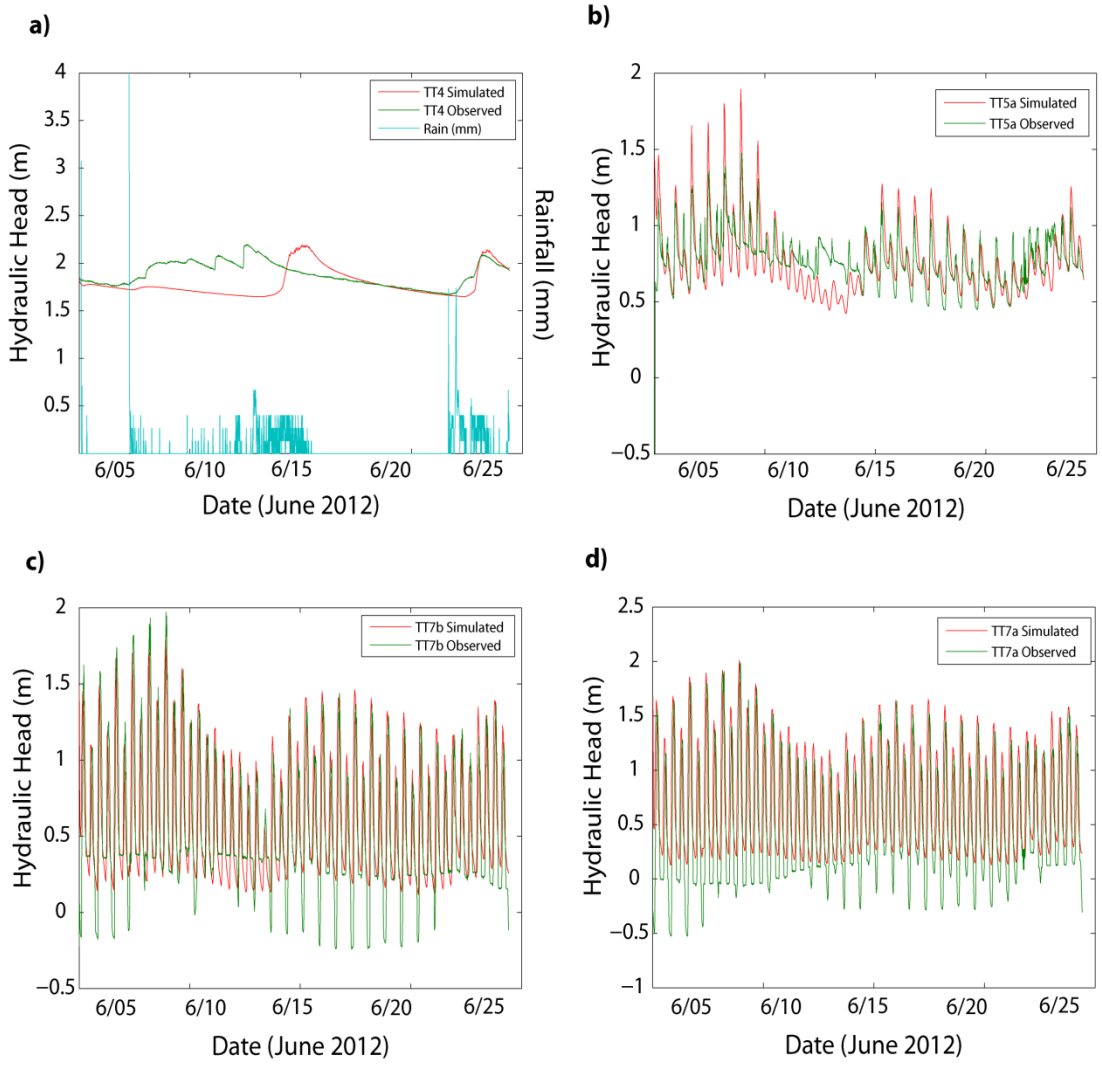

Figure 3.7. a) Simulated hydraulic head, observed hydraulic head, and precipitation for well TT4-2 for June 2012. **b)** Simulated hydraulic head vs. field data for well TT5a. **c)** Simulated hydraulic head and observed hydraulic head for well TT7b. **d)** Simulated hydraulic head and observed hydraulic head for well TT7a.

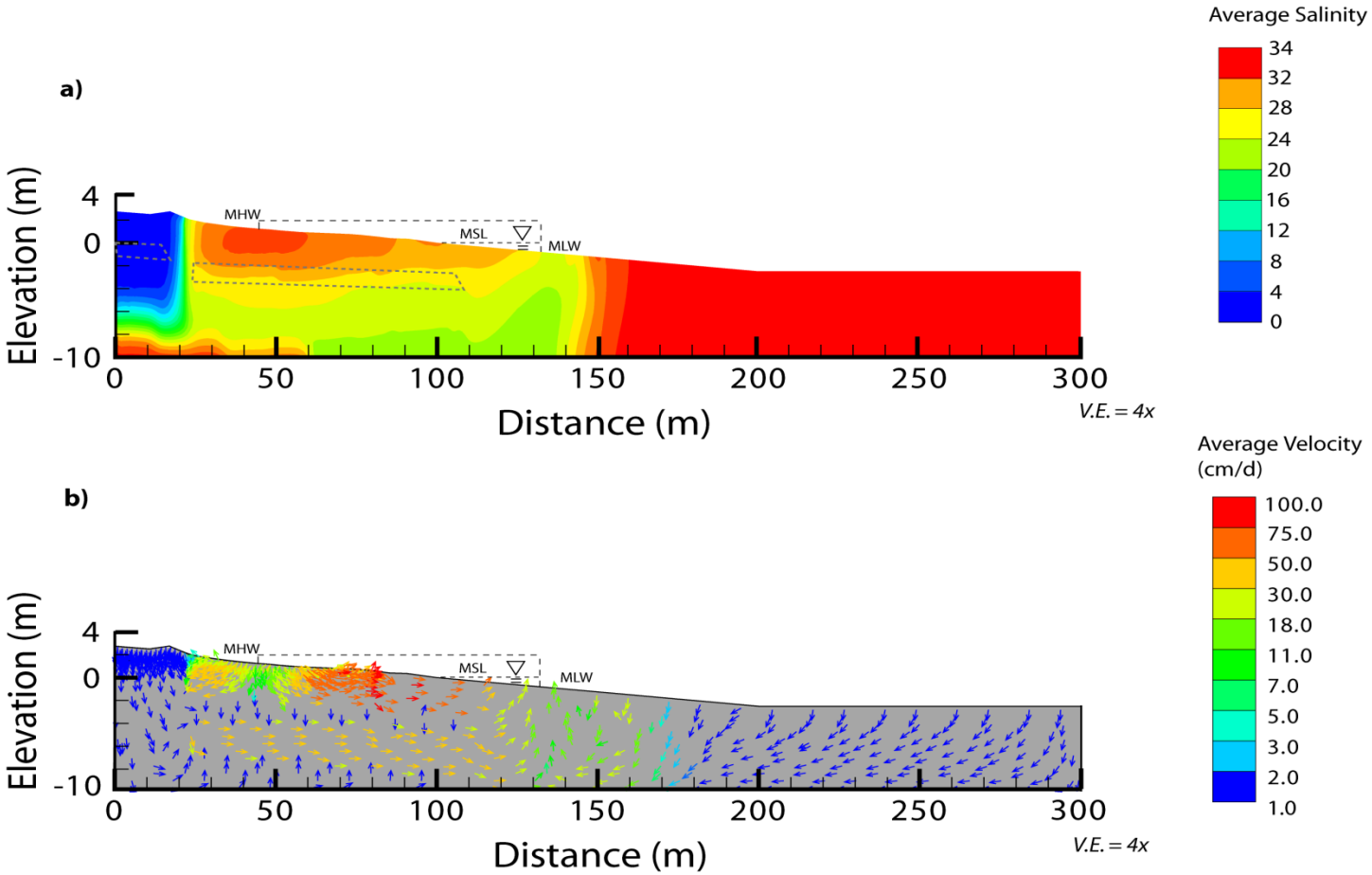

Figure 3.8. a) Average simulated groundwater salinity beneath Cabretta Beach for the month of June 2012. Vertical exaggeration is 4 times. **b)** Average groundwater flow velocity and direction beneath Cabretta Beach for the month of June 2012. Vertical exaggeration is 4 times.

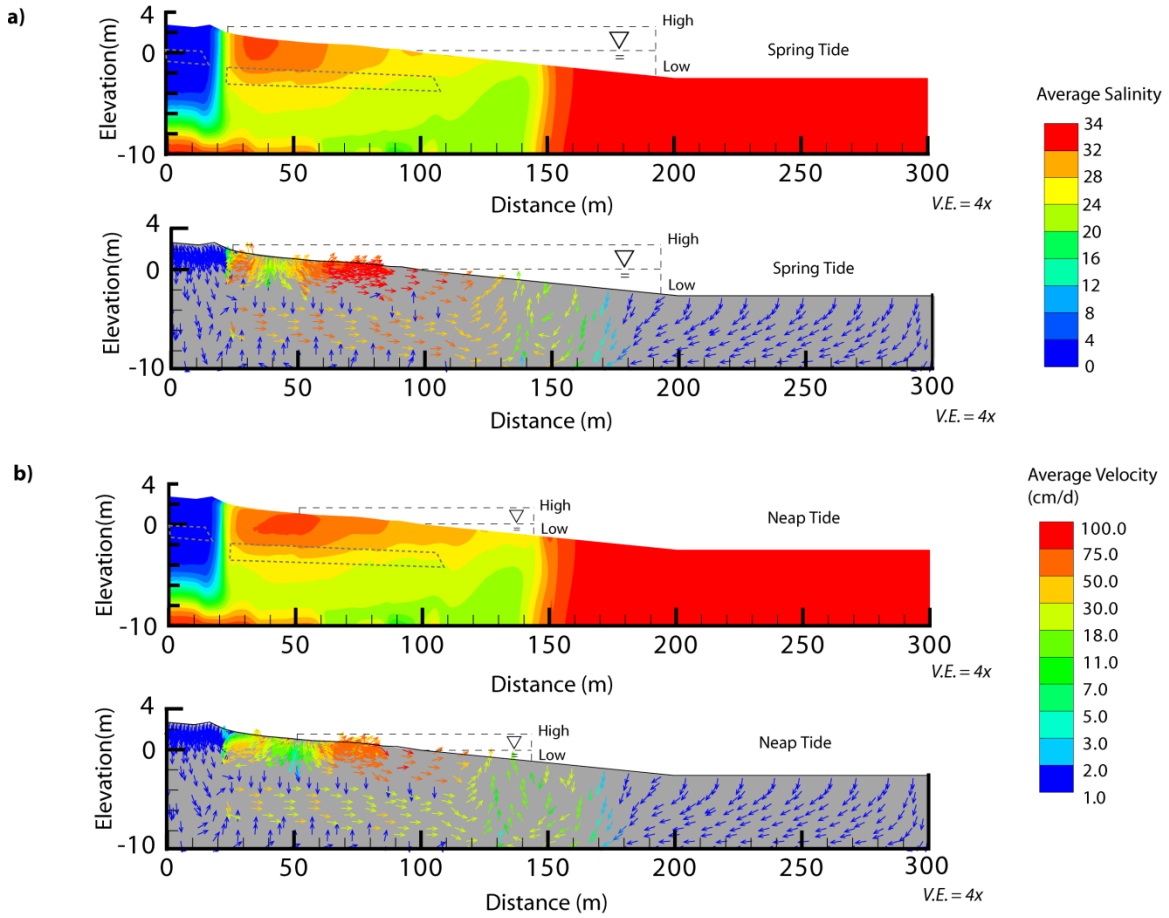

Figure 3.9. a) Average simulated groundwater salinity and flow velocity over the spring tide cycle that occurred from June 2 to June 8 2012. **b)** Average simulated groundwater salinity and flow velocity over the neap tide cycle that occurred from June 9 to June 14. Vertical exaggeration is 4 times.

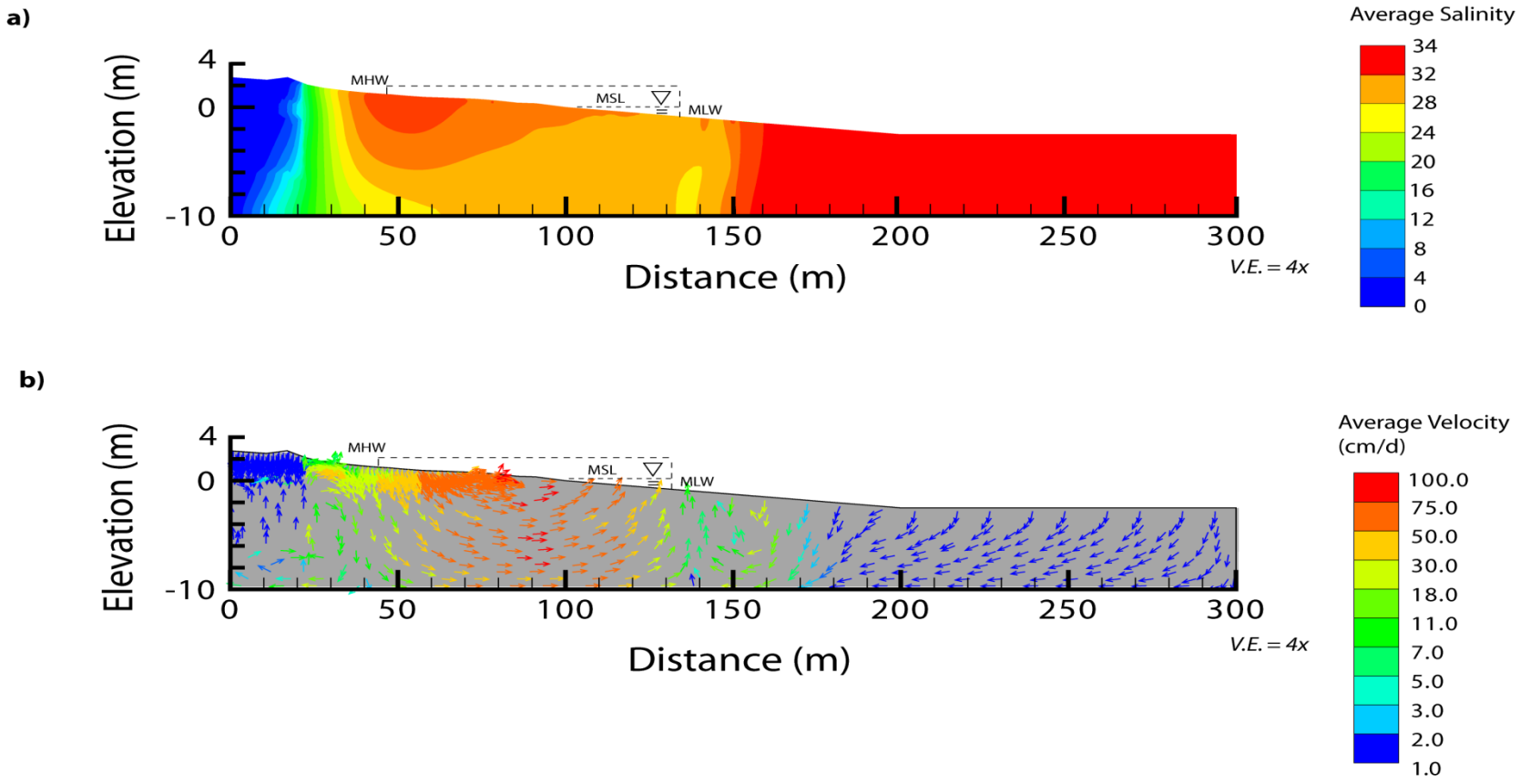

Figure 3.10. a) Average simulated groundwater salinity in the Cabretta Beach model where the buried mud layers were replaced with permeable beach sand. Vertical exaggeration is 4 times. **b)** Average groundwater flow velocity and direction in the Cabretta Beach model without mud. Vertical exaggeration is 4 times.

Chapter 4

The Impact of Future Sea-Level Rise on Coastal Groundwater Systems at the Nearshore and Embayment Scales

4.1 Abstract

Shallow coastal groundwater flow in beaches and salt marshes has been widely studied over the past 20 years, but far less is known about groundwater flow dynamics or the configuration of the freshwater-saltwater interface in the first major confined aquifer under the coastal environment. The impact of future sea-level rise on this system is even further understudied at this scale, termed the embayment scale. We used a combination of hydrogeologic field methods at Waccamaw Neck, SC, and numerical models to develop a revised conceptual model for groundwater flow and transport at an integrated nearshore-embayment scale. We also investigated the impact of future predicted rates of sea-level rise on this system. We found that the nearshore and embayment scale aquifers were hydraulically independent. A complex distribution of groundwater salinity developed in the first major confined aquifer, driven by continual diffusion of salt from overlying permeable sediments as sea-level rose through the mid to late Holocene. A plume of ancient fresh-to-brackish groundwater discharged near the terminus of the major confining unit offshore. Modern tidal simulations showed that the nearshore groundwater flow system contributed much higher fluxes of submarine groundwater discharge (SGD) to the coastal ocean than the embayment scale per unit area. We found

the North Inlet salt marsh to contribute total SGD flux of ~298 L/m^2/yr, and the inner shelf to contribute ~25 L/m^2/yr. For the inner shelf, this rate is equal to about 365 m^3/m/yr. Rates of submarine groundwater recirculation (SGR) were also greater for the nearshore scale. Our results suggest that predicted rates of future sea-level rise will have a much more significant impact on nearshore SGD and salinization than on the embayment scale. In general, total fluxes of SGD and SGR decreased significantly with future sea-level rise at the nearshore scale, but were relatively constant at the embayment scale.

4.2 Introduction

Coastal groundwater is important because it embodies two highly active fields of research: (1) offshore fresh groundwater reserves; and (2) submarine groundwater discharge (SGD). A significant portion of the world's population lives within 100 km of a coastline (Nicholls and Small, 2002), and these communities are largely dependent on fresh groundwater. Recently, studies have shown that significant reserves of fresh groundwater exist in continental shelves which could be potentially used in the future (Bakken et al., 2012; Edmunds, 2001; Krantz et al., 2004; Manheim et al., 2004; Post et al., 2013). The complex flow dynamics at the land-sea interface that control the distribution of fresh groundwater in continental shelves also drive SGD. SGD is defined as the flow of all water on continental margins from the seabed to the coastal ocean, regardless of fluid composition of driving force (Burnett et al., 2003). This flow is significant, and in the South Atlantic Bight (SAB) SGD is estimated to contribute three times more water to the coastal ocean than riverine input based on radium isotope budgets (Moore, 2010b). Studies on fresh groundwater reserves and SGD are both

concerned with the dynamics of the freshwater-saltwater interface (FSI). Numerous investigations have focused on the interface between land-derived fresh groundwater and saline groundwater from the late 1800's to present (Abarca et al., 2013; Ataie-ashtiani et al., 1999; Bakhtyar et al., 2013; Boufadel, 2000; Cooper, 1959; Ghyben, 1889; R.E. Glover, 1959; Heiss and Michael, 2014; Henry, 1959; Herzberg, 1901; Kohout, 1964, 1960, 1967; Robinson et al., 2006). When studying coastal groundwater reserves, the FSI represents the dynamic boundary between available fresh groundwater and encroaching saline water. In SGD studies, the FSI is important because it provides an indicator for the degree of mixing between fresh groundwater and seawater (Galeati et al., 1992; Lebbe, 1999; Yuqun Xue et al., 1995). Furthermore, future sea-level rise driven by climate change will have significant impacts on the availability and sustainability of fresh groundwater reserves, as well as on the dynamics of SGD. A better understanding of the FSI and the impact sea-level rise will have on coastal groundwater systems is necessary to develop more comprehensive conceptual models for groundwater flow and SGD.

Bratton [2010] identified the need to categorize SGD concepts and processes by spatial scale in order to improve clarity and understand in the literature. He classified SGD into three distinct spatial scales for passive margins: (1) the nearshore scale, which includes the surficial unconfined aquifer and extends offshore tens of meters; (2) the embayment scale, which includes the first major confined aquifer and its terminus, and extends offshore tens of kilometers; and (3) the shelf scale, which includes the total areal extent and thickness of permeable sediments on the continental shelf. As reviewed by *Heiss and Michael* [2014], the driving forces for SGD at the nearshore scale include freshwater discharge due to an inland hydraulic gradient, density-driven circulation at the

freshwater-saltwater interface, saltwater exchange driven by wave setup and swash infiltration, and tide-induced recirculation. Topographically driven regional flow in shallow confined aquifers beneath salt marshes and shallow offshore environment dominate SGD at the embayment scale (Bratton, 2010). At the shelf scale, *Moore and Wilson* [2005] hypothesized that SGD fluxes are mostly driven by flushing of saline water shallow permeable shelf sediments. The proportion of SGD through shelf sediments that is driven by regional flow is relatively unknown. Significant SGD fluxes are also caused by geothermal convection which induce buoyancy-driven flow through the shelf (Hughes et al., 2007; Kohout, 1967; Wilson, 2003), sediment compaction (Santos et al., 2012) and thermohaline convection associated with salt domes (Wilson and Ruppel, 2007). Overall, the majority of the scientific investigations of coastal groundwater have focused on the nearshore and shelf scales.

Current conceptual models for the impact of sea-level rise on coastal groundwater and the FSI are either too idealized, focus on the shelf scale, or involve groundwater pumping (Fig. 4.1a). The potential effects of sea-level rise on embayment and nearshore scale coastal aquifers under natural conditions are poorly understood (Fig. 4.1b). Recent studies have focused on the position of the FSI far offshore in confined aquifers with respect to past or future sea-level rise. Using analytical solutions, *Kooi and Groen* [2001] predicted that ancient fresh or brackish water typically exists around the terminus of thick, low permeability confining units, tens of kilometers off shore. These results, along with other studies, suggest that the FSI in submarine aquifers is out of equilibrium with respect to modern sea-level (Hathaway, 1979; Kohout et al., 1977). *Hughes et al*. [2009] showed that under changing sea-level conditions, chloride concentrations were the last to

equilibrate after pressure and temperature. *Werner and Simmons* [2009] developed a simple conceptual framework to provide first-order assessments for sea-level rise and salinization of theoretical coastal aquifers that were either freshwater flux or head-controlled systems. These results suggest that at steady state, systems with specified head boundary conditions are most susceptible to salinization. *Michael et al*. [2013] use similar criteria to assess the vulnerability of more realistic coastal groundwater systems to future sea-level rise. They showed that topography-limited systems, where the water table is essentially at land surface, are the most vulnerable to sea-level rise and make up approximately 70% of the world coastlines. Significant volumes of relatively fresh water have also been documented ~100 km offshore of the New England continental shelf (Hathaway, 1979; Kohout et al., 1988). *Person et al.* [2003] used a combination of analytical and numerical models to show that these plumes of fresh water offshore were most likely driven by elevated hydraulic gradients due to the Laurentide Ice Sheet and associated meltwater. *Cohen et al.* [2009] revisited this hypothesis with more detailed numerical models. They confirmed that these large reserves of fresh groundwater were most likely emplaced through enhanced recharge due to ice sheet loading, and facilitated by discharge through springs in submarine canyons. Offshore reserves of fresh groundwater also exist in the southeastern U.S. (Manheim, 1968), but they are too far south to have been impacted by ice sheet loading. These aquifers are topography-controlled systems which suggests that increased meteoric recharge during sea-level low stands is insufficient as a sole explanation for the presence of offshore brackish/fresh plumes. The development and sustainability of these relatively fresh plumes in the continental shelf at low latitudes are poorly understood. Finally, other studies have

focused on the combined effects of future sea-level rise and over extraction of groundwater (Loáiciga et al., 2011; Oude Essink et al., 2010). These studies showed that confined aquifers that are subject to over pumping experienced significant saline water intrusion with progressive sea-level rise. Aquifers at the embayment scale are not commonly used as groundwater resources (Bratton, 2010), and therefore the primary mechanism of salinization will probably not be saline water intrusion. Further investigation is required to understand the major drivers for salinization of both the nearshore aquifers and the confined aquifers of the embayment scale. Finally, additional knowledge pertaining to the extent of exchange between aquifers at the different scales of SGD and the dynamics of the freshwater-saltwater interface is required to develop a broad understanding of the potential impacts of future sea-level rise on coastal groundwater.

Conventional wisdom for groundwater flow at the land-sea interface assumes that multi-scale approaches will yield a more comprehensive understanding. *Bratton* [2010] identified the need to integrate the three spatial scales of SGD in order to more effectively address scientific and societal issues such as global sea-level rise and associated salinization of coastal aquifers. He also noted that due to compartmentalization created by stacked confining units and associated aquifers, SGD that spans multiple spatial scales is likely discontinuous. Further investigation is required to determine if SGD and related processes are in fact influenced by flow over multiple SGD scales through a compartmentalized system, or if the scales of SGD can effectively be studied independently.

The goal of this study is twofold: (1) to present a modern conceptual model for coastal groundwater flow, the distribution of salinity, and exchange across aquifers that spans the integrated embayment and nearshore scales; and (2) to investigate how this system will respond to predicted future sea-level rise driven by climactic warming. We used a combination of geologic coring, piezometer installation and monitoring, electrical resistivity tomography, and a two dimensional, variable-density, saturated-unsaturated, transient groundwater model to describe the embayment and nearshore scale SGD systems at Waccamaw Neck, SC. We then used projected rates of sea-level rise to model the effects of rising sea-level on groundwater flow and salinity distribution at the embayment and nearshore scale.

4.3 Methods

4.3.1 Field Methods

We conducted our study at Waccamaw Neck, SC, a large peninsula between Winyah Bay and the Atlantic Ocean. This study focused mostly on a large relict beach terrain, commonly referred to as Baruch Island, and the adjacent North Inlet salt marsh (Fig. 4.2a). This site was chosen because it provided remarkable access to embayment-scale aquifers that reach ~30 m below land surface, due to the presence of well-maintained dirt roads that extend out over the marsh. A unique challenge for studying SGD at the embayment scale is the difficulty and expense of drilling wells to reach the first major confined aquifer (10-30 m) in environments that are either inundated several times a day (intertidal wetlands), or permanently inundated (inner shelf). At North Inlet, SC, truck-mounted drilling rigs can drive approximately 1.25 km out over the marsh.

The North Inlet salt marsh is located in Georgetown County, SC, and is bounded to the west by a low relief, forested, relict beach-ridge terrain that trends SW to NE (Baruch Island), to the south by Winyah Bay, and to the east by modern barrier islands (Gardner and Porter, 2001). North Inlet is part of the North Inlet-Winyah Bay National Estuarine Research Reserve, which encompasses about 32 km^2 of tidally-dominated salt marsh and wetlands. The basin experiences a semidiurnal tide with an average range of 1.5 m and a period of 12.4 hours.

North Inlet basin evolved through mid-Holocene time (~6500 years BP) as sea-level gradually rose from a level at least 4 m lower than present (Gardner and Porter, 2001). As seawater invaded low lying areas, marsh deposits transgressed over Late Pleistocene beach-ridge sediments and formed the modern distribution of intricate tidal creek systems within sub-basins that are separated by relict beach ridges (Gardner and Porter, 2001). This retrogradational sequence built the nearshore scale hydrostratigraphic framework, comprised of a sandy, confined aquifer under salt marsh mud, incised by tidal channels that drain the wetlands (Gardner and Porter, 2001; Thibodeau et al., 1998) (Fig. 4.3).

We determined the local stratigraphy to ~12 m below land surface through Auger drilling conducted by the South Carolina Department of Natural Resources (SCDNR). 10 boreholes were drilled along the eastern forest-marsh boundary of Baruch Island and 2 boreholes were drilled on Goat Island (Fig. 4.2b). Each borehole was drilled until refusal was met in limestone, which generally occurred 12 m below land surface. Sediment from each borehole was logged in the field with respect to color, grain size, sorting, rounding, matrix or clast support, and composition. The thickness of the limestone aquifer was

determined from inspection of the core collected from SCDNR borehole GEO-380, which fully penetrated the unit. All boreholes sampled along the forest-marsh boundary were fresh. Salinity will be reported here using the Practical Salinity Scale of 1978 (UNESCO/ICES/SCOR/IAPSO, 1981), in which the salinity of fresh water is 0 and the salinity of seawater is 35.

We determined the distribution of groundwater salinity at North Inlet using Wenner array resistivity surveys using an AGI Super Sting R1 IP automatic switcchbox and 28 electrodes. In order to achieve maximum electrical penetration, surveys were conducted on dry ground when possible and were powered using dual 12-volt batteries, wired in parallel. Resistivity surveys 270 m long were conducted on relict beach-ridges along the long-axis of Bly and Goat Island (Fig. 4.2b). We used an electrode spacing of 10 m with a target depth resolution of approximately 30 m. An additional 135 m resistivity array was measured in Crabhaul Creek Basin near transect D, which has been detailed in numerous investigations (Gardner and Porter, 2001; Gardner and Reeves, 2002; Thibodeau et al., 1998) (Fig. 4.2b). In order to compensate for the attenuation of signal in saturated saline marsh sediment in Crabhaul Creek basin, we used a waterproof electrode cable with spacing of 5 m and a target depth resolution of approximately 15 m. Inverse modeling was conducted using AGI EarthImager 2D to convert measured apparent resistivity from the field to spatially correct resistivity cross-sections (AGI, 2009). These cross-sections were used to develop an initial conceptual model for local stratigraphy and groundwater salinity distribution.

A broad hydrostratigraphic framework was developed from the integration of the electrical resistivity results, borehole sediment logs and shallow stratigraphic data from

Thibodeau et al. [1998] and *Gardner and Porter* [2001] (Fig. 4.3). In general, a continuous, unconfined sand aquifer on the main upland and relict beach-ridge became a confined sand aquifer under the marsh basins, where the aquifer was typically capped by 1-2 m of marsh mud. We will refer to this aquifer as the marsh aquifer. Below the marsh aquifer, a silty, matrix supported shell-hash layer, approximately 3 m thick acted as a confining unit for an underlying continuous, silty-sand confined aquifer. This confined aquifer was approximately 4 m thick and was present at depths of approximately -7 to -11 m (MSL) (Fig. 4.3). We refer to this aquifer as the second confined aquifer. This aquifer was underlain by a dark-grey to black laminated clay and mudstone confining unit, referred to as the Lower Bridge Member, approximately 3 – 4 m thick. Beneath this regionally continuous confining unit was a bioturbated, moldic limestone aquifer, referred to as the Chicora Member, that is approximately 17 – 18 m thick (Fig. 4.3). The combination of the two deepest hydrostratigraphic units described here is referred to as the Williamsburg Formation (Fig. 4.3). The Chicora Member aquifer is underlain by low permeability silt and mudstones of the Crouch Branch confining unit (not shown). Topography was obtained from the 2005 Georgetown County lidar dataset (GIS Department, 2016).

This hydrostratigraphic framework was extrapolated offshore more than 10 km to capture the intersection of the Chicora Member aquifer with the seafloor. The Chicora was extended horizontally offshore because there was no significant dip measured between wells GEO-0385 and GEO-0387. Bathymetry was obtained from the Florida Fish and Wildlife Conservation Commission – Fish and Wildlife Research Institute at http://myfwc.com/research/ and National Oceanic and Atmospheric Administration

(NOAA) nautical charts (National Oceanic and Atmospheric Administration; National Ocean Service; Coast Survey, 2016). The regional relief ranges from a maximum elevation of 7.3 m (MSL) on Baruch Island to a minimum of -14.5 m (MSL) offshore.

Four groundwater monitoring wells were installed at North Inlet by the SCDNR as a part of the South Carolina Long-Term Groundwater Monitoring Network. Monitoring wells were installed at two locations: (1) Goat Island, located at 33°20'06.08" N and 79°11'39.72" W; and (2) along Marsh Road on Baruch Island, located at 33°20'28.40" N and 79°12'12.04" W (Figs. 4.2 and 4.3). At each site, we targeted the second confined aquifer at approximately –7 m (MSL) and the Chicora Member limestone aquifer at approximately -14.5 m (MSL). The shallow wells had a screened interval of 0.61 m, and the deep wells had a screened interval of 1.5 m. All four monitoring wells were constructed using 4-inch diameter, Schedule-40, flush-joint PVC. After emplacement of the well into the borehole, the screened intervals were packed with filter sand. The remainder of the borehole was filled with a 5-ft plug of bentonite and grouted with cement to land surface. At Goat Island, well GEO-0384 was screened at -8.41 m (MSL) and well GEO-0385 was screened at -27.61 m (MSL). On Marsh Road, well GEO-0386 was screened at -10.36 m (MSL) and well GEO-0387 was screened at -27.43 m (MSL). The wells were fully developed by blowing with air until a clear, sand free discharge was achieved. All four wells were then instrumented with an In-Situ Aqua TROLL conductivity logger and a Solinst Levelogger Edge water level logger, which continuously record data at 60 min intervals. A barometric pressure data logger was also installed at the Goat Island site used to correct recorded water levels.

4.3.2 Numerical Methods

Groundwater simulations of sea-level rise, tidally influenced flow and solute transport processes were conducted using SUTRA (Voss and Provost, 2002). SUTRA is a 2D, finite element groundwater transport model that simulates variable-density, saturated-unsaturated fluid flow and transport of either energy or dissolved substances in the subsurface environment. *Wilson and Gardner* [2006] modified the governing Richards equation in SUTRA to account for changes in total stress associated with tidal loading:

$$\nabla \cdot [K(\Psi)\nabla h] = S_w S_s \frac{\partial h}{\partial t} + \varphi \frac{\partial S_w}{\partial t} - \alpha_s S_w \frac{\partial \sigma_T}{\partial t} \qquad (4.1)$$

where K is hydraulic conductivity, Ψ is negative pressure head, h is hydraulic head, S_w is water saturation, φ is porosity, σ_T is total stress and S_s is the specific storage,

$$S_s = \rho g(\alpha_s + \varphi\beta) \qquad (4.2)$$

where ρ is the density of water, g is gravity, α_s is sediment compressibility and β is fluid compressibility.

The model domain extends 25 km from the Waccamaw River to the Atlantic Ocean inner continental shelf (Fig 4.4.). The model reaches ~2 km beyond the terminus of the Chicora Member aquifer to prevent boundary effects in the simulations. The bottom of the model domain represents the contact of the Chicora Member limestone with the Crouch Branch confining unit.

A 2D finite element mesh with 15,277 nodes and 14,256 elements was constructed using ModelMuse (Winston, 2014). All elements were 25 m in length and

ranged from approximately 4.5 m to less than 50 cm in depth. The mesh was refined near the surface of the model, where flow rates were the greatest, to ensure the Peclet and Courant criteria were met. An additional grid with 12.5 m spacing (32,534 nodes and 30,512 elements) was used to test whether simulation results varied significantly with discretization. The two meshes produced nearly identical results. All subsequent simulations were conducted using the 25 m grid to balance computational efficiency and accuracy of results.

Hydrologic parameters were chosen for 5 distinct hydrostratigraphic units (Table 4.1): (1) fine grained sand; (2) marsh mud; (3) silty shell hash confining unit; (4) clay confining unit; and (5) limestone. Initial model permeabilities were assigned based on available field and modeling studies (Campbell and Coes, 2010; Hughes, 2016; Wilson et al., 2008). Layers with unknown permeabilities were calibrated manually using reasonable ranges for values based on sediment type (Freeze and Cherry, 1979). Permeability values for the confining units were determined iteratively by comparing simulated groundwater salinities to field measurements. The ratio of longitudinal to transverse dispersivity ($\alpha_L/\alpha_{T)}$ was held constant at a value of 10, with α_L equal to 10 m and α_T equal to 1 m (Gelhar et al., 1992; Smith, 2004). Smaller dispersivity values (5, 0.5 m) were tested on the 12.5 m discretization mesh, and the results were nearly identical.

Boundary conditions for the groundwater model were chosen to simulate transient groundwater flow and solute transport processes influenced by tidal forcing and sea-level rise (Fig. 4.4). The bottom and seaward vertical boundaries of the model domain were assigned a no-flow boundary condition. The landward vertical boundary was assigned a no-flow boundary above the Williamsburg and a specified hydraulic head boundary

below.. Within the Williamsburg Formation, the landward boundary nodes were assigned a hydraulic head (3.2 m above MSL), calculated by projecting the average hydraulic gradient measured in the confined aquifer between wells GEO-0385 and GEO-0387 (2.76 x 10^{-4} m/m). Surface nodes inundated by the Waccamaw River were assigned a specified hydraulic head equal to the average head of the river (0.33 m above MSL). The upper boundary landward of the Waccamaw River was assigned a combined specified fluid pressure and flux for every surface node. Areas that were inundated by the sea were assigned a pressure based on the weight of the overlying water column (Wilson and Gardner, 2006). Surface nodes that were not inundated by the sea were assigned boundary conditions depending on the saturation. Surface nodes with saturations less than one were assigned a specified fluid flux to simulate rainfall (Q_F), and surface nodes with saturations equal to one developed a seepage face (pressure equals zero). We did not simulate evapotranspiration in our model, which led to a slight under-approximation of salinity in the marsh basins.

Four sequential simulations were performed to investigate groundwater flow and solute transport associated with sea-level rise and tidal fluctuations. We simulated (1) past sea-level rise from 6.47 ka BP to present; (2) tidally-driven flow under modern conditions; (3) future sea-level rise from the present to the year 2100; and (4) tidally-driven flow under conditions projected for 2100. We separated the sea-level rise and tidally-driven flow simulations to maximize computational efficiency. Small time steps are required to simulate tidally-driven flow. Attempting to simulate such small time steps over thousands of years led to infeasible total simulation times.

The initial simulation ran for 6,470 years, from the mid-Holocene to present, with 1 month time steps. Sea-level was approximately -6.6 ± 1 m lower ~6.6 ka BP than the AD 1900 sea-level for the northern South Carolina coast (Engelhart and Horton, 2012; Gardner and Porter, 2001). Initial conditions were handled by assigning all nodes in the domain a hydraulic head equal to hydrostatic pressure. Initial conditions for salinity were assigned based on results from preliminary simulations in which the freshwater-saltwater interface in the Chicora aquifer was set at several distances seaward of the modern coastline, including a simulation where the initial salinity in the entire domain was set to 0. These initial conditions reflect the fact that sea-level had been rising for thousands of years prior to the start of our simulation, and the position of the freshwater-saltwater interface 6.5 Kya was unknown. Results showed that position of the freshwater-saltwater interface was insensitive to the initial conditions, developing slightly seaward of the terminus of the Lower Bridge confining unit. Sea-level rose at a rate of 1.3 mm/year from 6.6 ka BP to 4 ka BP and at a rate of 0.8 mm/year from 4 ka BP to AD 1900 (Engelhart and Horton, 2012). The results of this simulation were used as the initial conditions for the subsequent modern tidal simulation.

The second simulation incorporated tidal fluctuations and was used to investigate SGD and solute transport under modern conditions. A semi-diurnal lunar tide with an amplitude of 0.75 m and a period of 12.4 hours was imposed on the upper boundary seaward of Baruch Island. Mean sea-level was constant in this simulation, and a quasi-equilibrium solution for salinity and pressure was reached after approximately 25 years. Time steps were 5 minutes long. Mean sea-level was set to 0.068 m, the average MSL of the tide data over the study period.

The impact of future sea-level rise on SGD was investigated by a third simulation of sea-level rise through the year 2100. Future rates of sea-level rise remain uncertain, so we simulated three sea-level rise scenarios based on predictions of *Rahmstorf* [2006; 2012], using rates of sea-level rise of 4, 6 and 9 mm/yr. Simulations covered 100 years with time steps of 1 day. Mean sea-level rose from 0.068 to 0.468, 0.668, and 0.968 m, respectively, for the three separate sea-level rise scenarios.

The final simulation included tidal fluctuations for conditions projected for the year 2100, to investigate future nearshore/embayment scale SGD after various rates of sea-level rise. Mean sea-level was constant in these simulations and a quasi-equilibrium solution for salinity and pressure was reached after approximately 25 year, using 5 minute time steps. The amplitude and period of the tide remained the same.

The total volume of groundwater discharging to the coastal ocean (SGD) and the total volume of seawater recirculation (SGR) were calculated in each simulation. We distinguished between the embayment and nearshore scales of SGD and SGR by dividing the surface nodes into two spatial categories: a salt marsh zone, which included all nodes from the forested upland-marsh boundary to the center of the seaward-most relict beach-ridge, and an inner shelf zone, which included all nodes seaward of the marsh zone. Total volumes of SGD and SGR were calculated for the marsh and inner shelf zones in all simulations, with one exception. Volumes of SGD and SGR were not calculated for the salt marsh in the simulation of past sea-level rise because the salt marsh did not exist at its current location. SGD and SGR were calculated for each time step by summing velocities in and out of surface elements and multiplying by porosity and element area. Fluxes in and out of the groundwater model were further grouped based on salinity.

Salinity was grouped using USGS guidelines, into fresh (0 to 1), brackish (1 to 10) and saline (>10). All recharge into the model at surface nodes that were not inundated by the ocean was fresh (rain). All recharging water at surface nodes inundated by the ocean was saline (35).

Recent studies investigating the impact of accelerated sea-level rise on salt marshes have shown that the relative elevation of these marshes increases with the accretion of organic and inorganic material (Baustian et al., 2012; Kirwan and Murray, 2007; Morris et al., 2013, 2002). We chose not to include salt marsh accretion in our future sea-level rise groundwater models for simplicity and because we assumed the marsh in its current location would become fully inundated by the year 2100. *Alizad et al.* [2016] showed that a similar salt marsh system in northeastern Florida would be unable to keep up with rapid sea-level rise through the year 2080 using a coupled Marsh Equilibrium Model (Morris et al., 2002) and hydrodynamic-physical model. Therefore, although the marsh likely drowns prematurely in our models, our calculations of tidally-driven flow are realistic for the year 2100. Additionally, the bathymetry of the shallow seafloor and hydrostratigraphy would be different in 2100 after continued erosion of the salt marsh, but flow in the second and third confined aquifers would be relatively unaffected.

4.4 Field Results

Electrical resistivity tomography surveys provided an initial conceptual model for the distribution of pore water salinity and hydrostratigraphy at North Inlet (Fig. 4.5a-c). All three surveys showed a clear transition at approximately -12 m below land surface, from low (~1 Ohm-m) to moderate/high resistivities (15 – 100 Ohm-m; Fig. 4.5a-c). This

depth corresponds to the contact between the overlying unconsolidated sediments and the Lower Bridge confining unit. These results suggest that the Chicora Member aquifer transmits fresh groundwater at least 1.5 km from the mainland under the salt marsh.

Hydraulic head data collected at each monitoring well were used to estimate the dominant groundwater flow direction and the magnitude of the hydraulic gradient. In general, the average hydraulic head in the second confined aquifer and the Chicora Member decreased across the transect from NW to SE (Table 4.2). The average hydraulic gradient in the second confined aquifer (GEO-0386 to GEO-0384) was -9.9×10^{-4} (m/m) and for the Chicora Member aquifer (GEO-0387 to GEO-0385) it was approximately -2.8×10^{-4} (m/m). A tidal signal was present in every well except GEO-0386, which was located outside the tidal propagation distance in the second confined aquifer. The flow direction was always seaward between the two wells in the second confined aquifer. Groundwater flow was seaward in the Chicora aquifer at all times except high tide, when a weak positive hydraulic gradient ($\sim 6.0 \times 10^{-6}$) drove groundwater landward for a short period of time (2-3 hours) twice daily.

Groundwater salinities did not vary significantly in any well over the period of available data (*7/15 – 1/16*) (Table 4.2). Groundwater was fresh in all of the wells except in well GEO-0384 on Goat Island. A single in-situ measurement made at the location of well GEO-0384, 10 m below land surface, was taken during geoprobe collection. This measurement showed the salinity to be ~2.0 in the confined sand aquifer where we later screened GEO-0384. We also physically tasted the water sample to confirm it was fresh. Thereafter, groundwater salinity was continually monitored in-situ in the well, and the

average salinity was 50 (Table 4.2). We used the numerical model to further investigate groundwater salinity at this location.

4.5 Numerical Results

4.5.1 Model Calibration.

We calibrated the model to salinity data collected from the resistivity surveys and to observed salinity, hydraulic head, and tidal amplitude in the four monitoring wells. In the second confined and Chicora Member aquifers, we matched tidal amplitude, which decreased with decreasing permeability, and matched hydraulic head, which increased with decreasing permeability. We found a permeability of 5×10^{-12} m^2 to best match the data from wells GEO-0384 and 0386 in the second confined aquifer. The hydraulic head was less sensitive to the permeability of the Chicora Member, where the hydraulic head was very near steady-state. In general, the hydraulic gradient between wells GEO-0385 and 0387 increased with decreasing values of permeability. Permeability values in the Chicora Member were constrained to between 1×10^{-11} and 5×10^{-12} m^2. Simulation results are reported for both values.

The model was able to accurately reproduce measured groundwater salinity and hydraulic head in wells GEO-0385, 0386, and 0387. The model was unable to reproduce saline groundwater conditions measured under Goat Island, in well GEO-0384, under reasonable hydraulic circumstances. To accurately simulate the hydraulic head measured on Goat Island, rates of precipitation always dictated that groundwater here was fresh. These simulated fresh groundwater results matched the in-situ salinity data we collected from the geoprobe core and the resistivity results for Goat Island (Table 4.2; Fig. 4.4c).

4.5.2 Model Results

Our results suggest that the nearshore and embayment scale SGD systems at Waccamaw Neck are hydraulically independent. The presence of a 3-4 m thick confining unit prevented groundwater exchange between the Chicora Member confined aquifer and the overlying permeable sediments over the time scales investigated in this study (Fig. 4.6). Diffusion was the dominant mechanism for solute transport across the nearshore and embayment scale aquifers. Although the average flow direction was upward in the Lower Bridge confining unit, the average velocity was approximately 0.001-0.002 m/yr over the all the simulations, too slow to counteract diffusion (Fig. 4.6). Due to the lack of groundwater exchange between the nearshore and embayment scale SGD systems, flow and salinity configuration at these two scales reacted differently to driving forces such as tidal fluctuations and sea-level rise.

Groundwater flow paths were variable between the nearshore and embayment scale SGD systems. In the salt marsh zone, flow under modern and future conditions was controlled mostly by tidal fluctuations and flow divides set up by local topography. Above the Lower Bridge Member confining unit, all meteoric groundwater from the upland generally discharged to the nearest tidal creeks (Fig. 4.6). Seawater that infiltrated the salt marsh basins circulated through the marsh aquifer then also discharged to the tidal creeks (Fig. 4.6). Above the Lower Bridge confining unit, each salt marsh basin and nearby uplands were isolated systems, with little or no hydraulic connection to adjacent groundwater systems (Fig. 4.6). For the nearshore scale, groundwater salinity increased in the entire salt marsh basin due to increased exchange with the seawater at high tide. Groundwater flow in the Chicora Member aquifer was mostly unaffected by tidal

fluctuations. The only change was that the direction of the hydraulic gradient reversed for a short period of time (2-3 hours) below areas that were inundated at high tide (Fig. 4.7b-c), but the net effect of this twice-daily flow reversal was not significant with respect to the dominant flow pattern. Groundwater generally flowed from the landward boundary of the model out to sea. Different driving forces for flow between the nearshore and embayment-scale led to significant spatial variability in the distribution of salinity.

Simulations of groundwater flow during past and future sea-level rise showed that multiple freshwater-saltwater interfaces developed at different scales (Fig. 4.7). Over the late Holocene, salt water intruded into the entire section of sediments above the Lower Bridge confining unit between x = 6,250 and 17,500 m (Fig. 4.7c). The nearshore-scale aquifers were highly susceptible to progressive saline water intrusion and subsequent landward migration of the FSI. Sea-level rise through the Holocene was insufficient to drive significant saline water intrusion into the Chicora Member confined aquifer. Instead, fresh groundwater continually flowed seaward along the regional hydraulic gradient, maintaining the position of the offshore FSI (Fig. 4.7e). Salinization of the Chicora Member aquifer occurred by diffusion over thousands of years. This diffusion of salt into the fresh Chicora aquifer created a complex lateral transition zone of salinities in the Chicora Member from land to sea (Fig. 4.7b-e). At the conclusion of the past sea-level rise simulation, groundwater was fresh to brackish (0.5 – 8) in the Chicora Member in the landward 11 km of the domain (Fig. 4.7a-c). The Chicora Member contained saline water (> 10) under the ocean from x = 11 to 18 km (Fig. 4.7c-d). Seaward of this saline zone, brackish groundwater discharged from the confined aquifer into the coastal ocean in a large, dispersed plume extending from x = 18.5 to 22 km (Fig. 4.7e). This discharge

zone corresponded with the terminus of the Lower Bridge confining unit. Seaward of this zone was a classic FSI where density-driven convection caused seawater to circulate through the Chicora Member aquifer (Fig. 4.7e). Simulations of sea-level rise through the year 2100 showed that the nearshore scale continued to be highly susceptible to saline water intrusion (Fig 4.8a-b). Salinization of the permeable sediments above the Lower Bridge confining unit was geologically instantaneous with respect to the three rates of predicted sea-level rise (4, 6 and 9 mm/yr). The width of relict beach ridges decreased as mean sea level increased, which decreased the surface area for meteoric recharge into the marsh. Groundwater salinity increased significantly for the entire salt marsh basin. The total thickness of freshwater lenses beneath the uplands in the salt marsh decreased, and the position of the freshwater-saltwater interface above the Lower Bridge confining unit migrated landward an average of 354 m, from Bly Creek to the forest-marsh boundary of Baruch Island (Fig. 4.8a-b). The Chicora Member aquifer was mostly unsusceptible to salinization under natural conditions. Groundwater salinity in the Chicora Member only increased slightly beneath the marsh basin, where diffusion transported salts from the overlying sediments (Fig. 4.8b). Groundwater flow stagnated here due to density-driven convection caused by differences in groundwater salinity (Fig. 4.8b). Fresh groundwater was unable to make it under the marsh further than x = 6250 m (Bly Island).

The extent of hydraulic independence between the nearshore and embayment scale aquifers can be further investigating by examining fluxes of SGD and SGR (Tables 4.3 and 4.4). For the salt marsh zone, modern tidal fluctuations drove about 84% of the total SGR flux and 35% of the total SGD flux. Tidal fluctuations under future projected conditions in the salt marsh drove an average of 40% of the total SGR flux and an

average of 22% of the total SGD flux. Our results showed that SGR decreased by 16%, 27%, and 29% for the respective future mean sea-level elevations compared to modern conditions (0.47, 0.67, 0.97 m). Total SGD decreased by 24%, 34%, and 43% respectively (Table 4.3; Fig. 4.9a). At the nearshore scale, rising sea-level decreased both SGR/SGD, as well as the proportion of flow driven by tidal fluctuations. These results assumed that the salt marsh could not accrete fast enough to keep up with rising sea-level. The majority of the salt marsh platform did not drain during low tide when mean sea-level was greater than 0.67 m. This zone required daily flooding and draining by the tide to support hydraulic gradients that drove significant fluxes of SGD and SGR. For the inner shelf zone, tidal fluctuations did not drive significant fluxes of SGR/SGD except where tidally-driven recirculation occurred in newly inundated land surface. The regional hydraulic gradient was the primary driving force for groundwater flow at the embayment scale under modern and future conditions. In contrast to the salt marsh zone, SGR and SGD were higher for future conditions in the inner shelf zone (Table 4.4; Fig. 4.9b). Comparing between modern and future conditions, SGR increased slightly. These increases were driven by flow through newly inundated land surface, and by slightly higher rates of flow at the offshore FSI associated with density-driven convection.

The total volumes of SGR/SGD and the proportion of fresh to saline groundwater were highly variable between the nearshore and embayment scales. Under modern conditions, the salt marsh zone contributed about an order of magnitude more SGD to the ocean than the inner shelf zone (Tables 4.3 and 4.4). Approximately 31% of the total SGD from the salt marsh was fresh (Fig. 4.9a). By the year 2100, the salt marsh contributed only about 5 times more SGD to the ocean than the inner shelf zone. The

total proportion of the salt marsh SGD that was fresh decreased to 12% (Fig. 4.9a). For the inner shelf zone, a significant shift from a majority of fresh SGD (84%) during past sea-level rise to present to a majority of saline SGD for future sea-level rise (64%) occurred (Table 4.4; Fig. 4.9b). This pattern suggests that total embayment scale SGD is mostly fresh during initial transgression and progressively becomes saltier through continued sea-level rise over thousands of years. Comparing between the salt marsh and inner shelf zones, the total proportion of fresh SGD is much larger for the inner shelf zone under present and future conditions. Fresh groundwater that discharged from the embayment scale aquifers was also significantly older than fresh groundwater that discharged from the salt marsh.

Estimates of residence times for the nearshore and embayment scales under North Inlet emphasize their hydraulic independence. Under modern conditions, average flow rates for the salt marsh and second confined aquifer were approximately 20 m/yr. Groundwater paths under the salt marsh basin were heavily influenced by local flow divides, which generally prevented groundwater from flowing more than 100-200 m. Using these approximations, we calculated an estimate for the residence time of the nearshore-scale aquifers to be on the order of tens of years. In the Chicora Member aquifer, average flow rates were approximately 2 m/yr, and groundwater flowed horizontally approximately 22 km before discharging to the sea. These approximations indicate residence time estimates for the embayment scale system to be on the order of tens of thousands of years. This indicates that groundwater flow and solute transport processes are likely out of equilibrium with modern sea-level at the embayment scale.

Our results suggest that the brackish groundwater plume located near the terminus of the Lower Bridge confining unit was remnant from the previous FSI and associated sea-level low stand. Although the permeability of the Chicora Member confined aquifer is relatively high, the hydraulic gradient that drives flow is low. Slow groundwater flow rates resulted in a salinity configuration that is out of equilibrium with modern hydrologic conditions. This offshore brackish plume was unable to discharge to the ocean as fast as sea-level rose over the Holocene, resulting in an isolated plume that is no longer resupplied with fresh groundwater from the mainland under modern conditions. Continual diffusion of salt into the Chicora Member aquifer beneath the salt marsh and shallow nearshore environment prevented fresh groundwater from flowing out to sea without becoming significantly saltier. The brackish groundwater plume continued to slowly discharge to the ocean through the year 2100, decreasing in width approximately 175 m, to a total width of about 3 km.

4.6 Discussion

Our simulations indicate that groundwater flow and solute transport processes are different between the nearshore and embayment scale. With respect to sea-level rise and tidal fluctuations, we found the nearshore scale to be much more sensitive. Future sea-level rise did not drive significant salinization of the embayment scale aquifer. The embayment scale was largely independent from the overlying nearshore scale. This hydraulic independence is important because it suggests that investigations of SGD do not necessarily need to be spatially integrated to achieve a more comprehensive understanding. Groundwater studies that focus on one scale of SGD need not include the potential effects of the underlying/overlying scales of SGD. In our simulations, no

significant groundwater exchange occurred between the aquifers of the nearshore and embayment scales due to a thick confining unit. SGD fluxes calculated in our study are in close agreement with those from prior investigations at North Inlet salt marsh.

For the modern tidal simulations, we calculated a SGD flux of approximately 298 $L/m^2/yr$. *Wilson and Morris* [2010] calculated a range of SGD fluxes at North Inlet of between 0.44 to 8.4 L/m^2 per tide, equal to 321.2 to 6132 $L/m^2/yr$. Our results fall on the low side of this reported range likely because our model was a two-dimensional transect through the salt marsh. Our SGD/SGR fluxes were calculated over the entire horizontal extent of the salt marsh basin across the transect. We calculated an average SGD flux specific to the tide creeks in our groundwater model of 0.15 m^3 per meter of creek bank per tidal cycle. Using the marsh island creek density at North Inlet of 0.013 m/m^2 (Novakowski et al., 2004), we calculated an SGD flux of ~4.3 L/m^2 per tide, equal to 3139 $L/m^2/yr$. Adjusted for tide creek density at North Inlet, our SGD flux is in close agreement with the values reported by both *Morris* [1995] (~5 L/m^2 per tide) and *Krest et al.* [2000] (10-20 L/m^2 per tide).

Modern groundwater simulations and the respective flux of SGD at the embayment scale can be used to estimate the proportion of total SGD through the inner shelf that is caused by regional flow and density-driven convection. *Moore* [2010a] calculated SGD fluxes to the South Atlantic Bight (SAB) using radium isotope fluxes and concentrations of radium in coastal groundwater. He showed that in order to support measured radium isotope activities, a SGD flux of ~2.1×10^{14} L/yr was required. He assumed a coastline length of 600 km, and an approximate shelf width of 100 km, resulting in a normalized SGD flux of 3500 $L/m^2/yr$ to the South Atlantic Bight. He suggested that this flux could

be generated by flushing a layer of sand 2 m thick continuous across the entire shelf. This reservoir must be flushed 3 times a year, requiring an average upward flow rate of 5 m/yr (Moore, 2010b). Our simulations predict an approximate SGD flux of 32 $L/m^2/yr$, equal to ~365 $m^3/m/yr$ to the SAB. This flux is less than 1% of the SGD flux calculated by *Moore* [2010a]. Upward flow velocities of 4-7 m/yr were located in the offshore brackish discharge zone, but flow velocities were minimal for the remainder of the inner shelf. Also, fresh or relatively brackish groundwater cannot carry significant concentrations of radium. Our model only extended 15 km offshore, instead of 100 km, and only contained the first major regional confined aquifer. A full shelf-scale model would lead to higher calculated SGD fluxes, but it's improbable they would increase by ~10,000% to 3.5 $m^3/m^2/yr$. The coastal aquifers in this region are high-permeability systems, but the regional hydraulic gradients are very low at the embayment scale. Hydraulic gradients could be more significant in the deeper, regional confined aquifers, but these aquifers are the principal drinking water aquifers in the Southeastern United States. These systems suffer from significant over-pumping and associated cones of depression, and likely do not drive high fluxes of SGD to the coastal ocean. Our results strongly support the hypothesis that episodic flushing through surficial sands on the shelf is the most significant driver for SGD through the shelf.

A revised conceptual model for integrated nearshore/embayment scale SGD is presented in Figure 4.10. At the nearshore scale, SGD and SGR are driven mostly by waves, lunar tides, seasonal variations in mean sea-level and density-driven convection. Meteoric water and seawater infiltrate the surficial, unconfined aquifer and mix across local freshwater-saltwater interfaces. We estimate the nearshore scale SGD flux (per unit

area) to be at least an order of magnitude greater than embayment scale SGD flux. Groundwater flow and solute transport in the nearshore scale are independent from the aquifers of the embayment scale. Groundwater pressure and the distribution of salinity at the nearshore scale require time scales of tens of years to reach quasi-equilibrium. At the embayment scale, equilibrium likely requires time scales of tens of thousands of years. SGD is driven by hydraulic gradients associated with changes in regional topography. SGR is caused mostly by density-driven convection across major freshwater-saltwater interfaces (Fig. 4.10). Meteoric water recharges these confined aquifers up-dip where they outcrop on land, and groundwater flows continually seaward along a steady gradient. Low hydraulic gradients drive groundwater flow under the nearshore and inner shelf environments at velocities on the order of tens of centimeters to a couple meters per year. At the embayment scale for the Southeastern U.S., the first major confined aquifer (Chicora Member: ~55 Ma; Floridan Aquifer: 20 – 60 Ma) most likely predates the most recent sea-level transgression (~10,000 Kya to present). These aquifers have been influenced by continued sea-level rise over the Holocene, but have not been subjected to direct saline water intrusion for millions of years. Salinization of these aquifers occurs through slow diffusion from adjacent salty sediments (Fig. 4.10). The low hydraulic gradients of these systems prevent fresh groundwater from the mainland from flowing directly out to sea unaltered. Instead, this freshwater mixes with salts diffusing from adjacent aquifers, and creates a large brackish-to-saline plume of groundwater that undergoes slight density-driven convection, which reduces the magnitude of the hydraulic gradient out to sea. Further seaward, a plume of fresh-to-brackish paleo-groundwater discharges at the terminus of the embayment scale confining unit (Fig.

4.10). This paleowater discharge zone has been identified offshore of the Northeastern U.S. (Cohen et al., 2010; Person et al., 2003), and in analytical studies of the continuation of SGD systems offshore (Kooi and Groen, 2001).

A significant difficulty in studying SGD at both the embayment and shelf scales is uncertainty surrounding the underlying stratigraphy and geologic variability. Our results confirm that breaks in confining units control the outflow point for fresh groundwater. The location of major breaks in underlying confining units, as well as their terminuses, could be determined using tow-behind electrical resistivity tomography. Long, wide, shore-parallel plumes of high resistivity could likely signal the terminus of these major confining units offshore. Anomalous plumes of high resistivity would likely demarcate breaks in confining units. Determining the offshore extent and integrity of the major confining units of coastal aquifers would greatly aid in developing more accurate groundwater models and SGD studies in general. Locating offshore plumes of fresh or brackish groundwater bodies could also be helpful to mitigate future pressures on drinking water supply.

The depletion of potable groundwater in coastal communities is a major concern for many coastal communities due to accelerated rates of sea-level rise and continued over-pumping of principal groundwater aquifers. Several studies have begun to identify potential sources of fresh/brackish groundwater that could be exploited to mitigate future drinking water shortages (National Research Council, 2008; Post et al., 2013). Our results suggest that embayment scale aquifers that are not currently over-pumped could have significant volumes of fresh or brackish volumes 10-50 km offshore. These plumes have a much lower salinity than seawater, and would be much less expensive to treat and

process (Bakken et al., 2012). Our model suggests a total volume of about 1.6 x 10^4 m^3 per meter of coastline of slightly brackish groundwater offshore. Using a shore length of approximately 600 km and an average porosity of 30%, a rough, upper-bound estimate for the total volume of this offshore fresh/brackish plume in the South Atlantic Bight is 96 km^3. For reference, the total U.S. water demand in 2010 was about 1.3 km^3/day (355 billion gallons per day) (Maupin et al., 2010). After simulating sea-level rise through the year 2100, this zone only decreased in width by approximately 5%, implying these paleo-groundwater reserves could be a significant source of potable water in the future.

4.7 Conclusion

Our results indicate that SGD and solute transport are complex processes at the land-sea interface. Groundwater systems at the nearshore and embayment scales were not in significant hydraulic communication due to the presence of the Lower Bridge confining unit. As a result, the dominant driving forces for groundwater flow were largely different between the two scales. At the nearshore scale, SGD and SGR were controlled by tidal pumping and variations in mean sea-level. At the embayment scale, SGD and SGR were mostly driven by the regional hydraulic gradient and density-driven convection through zones of differing salinity. Groundwater systems at the nearshore scale contributed an order of magnitude more SGD to the coastal ocean per unit area than those at the embayment scale. SGD at the embayment scale was concentrated at the terminus of the Lower Bridge confining unit offshore. Estimates for groundwater residence times at the nearshore scale were on the order of tens of years. At the embayment scale, residence times were estimated to be on the order of tens of thousands of years. Due to the

hydraulic independence between the nearshore and embayment scales, the impact of future sea-level rise was variable between the two.

Salinization driven by sea-level rise was much more significant at the nearshore scale than at the embayment scale. At the nearshore scale, salinization of the shallow aquifers was driven by progressive saline water intrusion that tracked with sea-level rise. By the year 2100, the entire North Inlet salt marsh system was salty. The dominant mechanism for salt transport into the Chicora Member aquifer was diffusion over thousands of years. Salinity was largely unchanged in the Chicora Member aquifer after future sea-level rise, except directly under the salt marsh where salinity increased slightly. The distribution of salinity in the Chicora Member aquifer was out of equilibrium with modern sea-level. Total fluxes of SGD and SGR decreased with increasing sea-level at the nearshore scale. The proportion of this flow that was driven by tidal fluctuations also decreased under future sea-level conditions at the nearshore scale. The total volume of fresh and brackish SGD decreased significantly under future sea-level conditions. In general, SGD and SGR were not significantly impacted by future sea-level rise at the embayment scale through the year 2100. The total volume of fresh SGD at the embayment scale decreased significantly from the mid Holocene to the year 2100.

Finally, our simulation results strongly suggest the presence of an offshore brackish plume of discharging groundwater is a remnant from the FSI during the last sea-level lowstand. Although this reservoir of groundwater offshore of North Inlet, SC is purely theoretical, offshore plumes of fresh or brackish groundwater have been reported in the Atlantic continental margin in other studies. The possibility for significant volumes of easily-treatable groundwater at the embayment scale could help mitigate future

shortages of potable water in coastal communities as traditional aquifers become progressively more saline. Future studies investigating the integrity and extent of confining units and their potential to trap fresh or brackish paleo-groundwater offshore are warranted.

Table 4.1. Model parameters used for the North Inlet groundwater model.

Model Parameter	Fine Sand	Marsh Mud	Silty Shell Hash	Silty Clay (*Lower Bridge Member*)	Limestone (*Chicora Member*)
Porosity φ	0.4	0.72	0.4	0.35	0.3
Permeability k (m^2)	5×10^{-12} (1×10^{-10} 1×10^{-12})*	4×10^{-13} (1×10^{-13} – 1×10^{-15})*	1×10^{-13} (1×10^{-13} – 1×10^{-15})*	1×10^{-16} (1×10^{-15} – 1×10^{-17})	1×10^{-11} m^2 (1×10^{-11} – 5×10^{-13})
Longitudinal Dispersivity α_L (m)	10	10	10	10	10
Transverse Dispersivity α_T (m)	1	1	1	1	1
Van Genuchten Fit Parameters m, n	0.875, 8	0.6, 2.5	*Never exposed*		
Capillary Rise α (kPa^{-1})	2.05×10^{-4}	3×10^{-3}			

*Range of permeability values tested for each sediment unit

Table 4.2. Hydraulic head and salinity data collected a North Inlet.

Measured Data	GEO – 0384 (*Goat Island*)	GEO – 0385 (*Goat Island*)	GEO – 0386 (*Marsh Road*)	GEO – 0387 (*Marsh Road*)
Average Hydraulic Head (m) *Continuous logger (7/15 – 1/16)*	0.71 ± 0.12[Ŧ]	1.63 ± 0.21	1.77 ± 0.07	1.93 ± 0.09
Average Salinity (PSU) *Continuous logger (7/15 – 1/16)*	50.6 ± 0.2	0.59 ± 0.003	0.46 ± 0.01	0.48 ± 0.007
Salinity Point Measurement (PSU)	2.0[*] (*2/5/14*)	0.5 *(1/27/16)*	0.5 *(1/27/16)*	0.3 *(1/27/16)*

[*]Salinity measured in-situ from a geoprobe core collected at approximately 10 m below land surface; at the exact location GEO-0384 was later installed.
[Ŧ] Values presented here are the average and standard deviation of the observed data.

Table 4.3. Marsh zone groundwater fluxes for the various simulations.

Flux ($L/m^2/yr$)	Tide 1 (msl = 0.07 m)	Sea-level rise 2 (4 mm/yr)	Sea-level rise 2 (6 mm/yr)	Sea-level rise 2 (9 mm/yr)	Tide 2 (msl = 0.47 m)	Tide 2 (msl = 0.67 m)	Tide 2 (msl = 0.97 m)
Q_F	211.1	151.8	144.9	130.5	146.8	125.1	104.5
Q_{SGR}	96.2	44.2	41.5	39.7	80.7	70.2	68.5
SGD_F	-91.1	-102.3	-97.9	-78.7	-25.1	-48.7	-3.28
SGD_B	-47.1	-23.5	-19.3	-20.5	-39.0	-9.7	-24.8
SGD_S	-159.6	-73.9	-72.5	-71.3	-161.3	-137.0	-142.6
Q_{TOT}	307.3	195.9	186.4	170.21	227.5	195.3	173.0
SGD_{TOT}	-297.8	-199.7	-189.7	-170.6	-225.4	-195.5	-170.9

Table 4.4. Inner shelf groundwater fluxes for the various simulations.

Flux ($L/m^2/yr$)	Sea-level rise 1 ǂ	Tide 1 ǂ	Sea-level rise 2 *	Tide 2 *
$\mathbf{Q_F}$	31.5 ± 0.02	31.9 ± 0.001	29.8 ± 0.06	28.5 ± 0.003
$\mathbf{Q_{SGR}}$	2.46 ± 0.51	11.2 ± 0.48	9.09 ± 2.5	14.9 ± 1.6
$\mathbf{SGD_F}$	-21.1 ± 0.01	-10.1 ± 0.001	-9.54 ± 0.07	-10.1 ± 0.001
$\mathbf{SGD_B}$	-0.31 ± 0.08	-3.53 ± 0.003	-2.16 ± 0.13	-2.81 ± 0.003
$\mathbf{SGD_S}$	-3.56 ± 0.60	-18.7 ± 0.54	-16.9 ± 2.6	-22.9 ± 1.7
$\mathbf{Q_{TOT}}$	33.8 ± 0.53	43.1 ± 0.48	38.9 ± 2.6	43.4 ± 1.6
$\mathbf{SGD_{TOT}}$	-25.0 ± 0.69	-32.4 ± 0.54	-28.6 ± 2.7	-35.8 ± 1.7

ǂValues presented here are the average and standard deviation of the results from the simulations using Chicora Member permeabilities of 1×10^{-11} and 5×10^{-12} m^2.

*Values presented here are the average and standard deviation of the results from three separate sea-level rise scenarios, using the two Chicora permeabilities listed above.

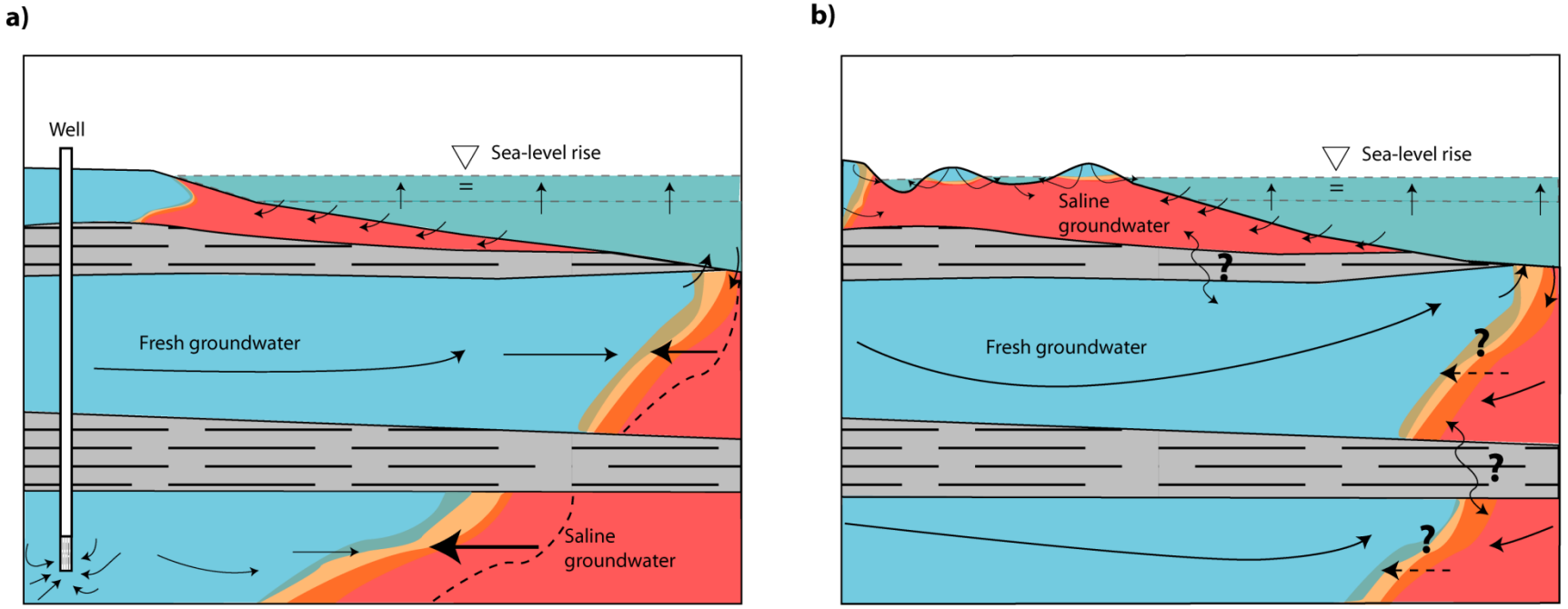

*Not drawn to scale

Figure 4.1. a) Conceptual model for saline water intrusion (SWI) due to the combined effects of sea-level rise and over pumping from a water supply well. Seawater intrudes the shallow aquifers of the nearshore scale as sea-level progressively rises. In the major confined aquifers, hydraulic head drops due to over withdrawal of groundwater, causing the freshwater-saltwater interface to migrate landward as saline water intrudes the fresh aquifer. **b)** Hypothesized effects of sea-level rise on coastal groundwater in a system not subject to over pumping.

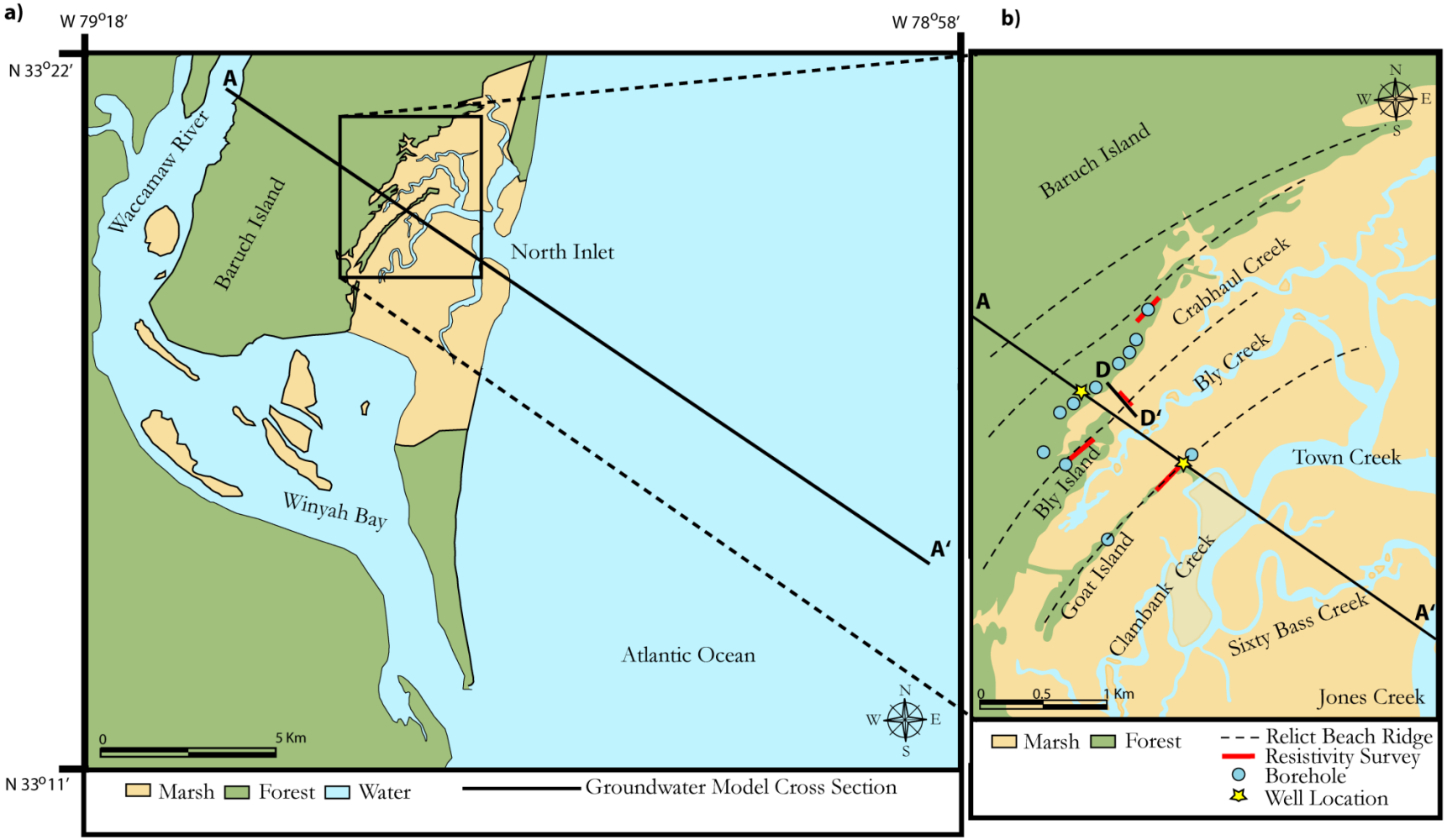

Figure 4.2. a) North Inlet site location map. **b)** North Inlet salt marsh basin and the location of groundwater wells, coreholes and resistivity surveys.

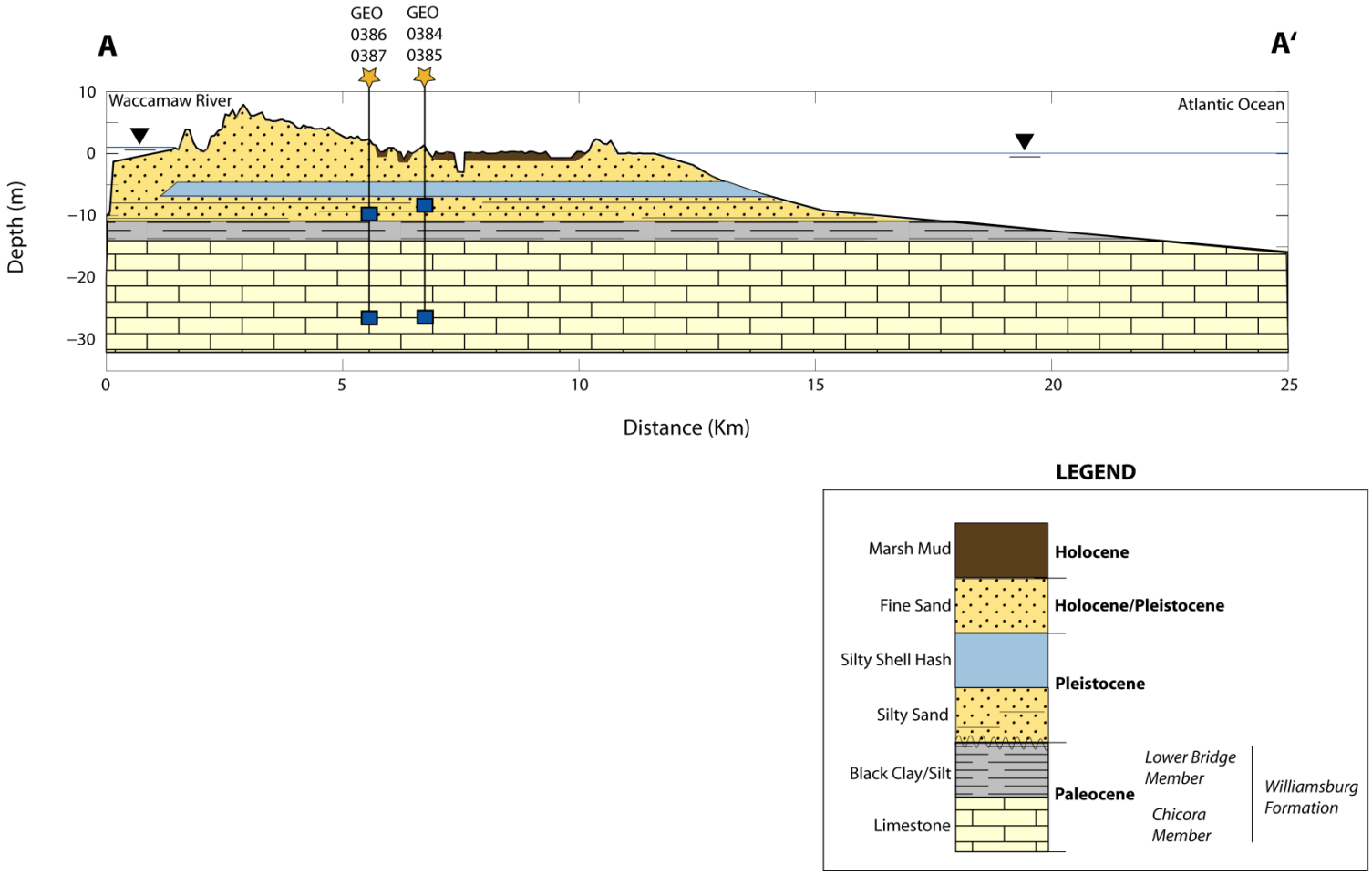

Figure 4.3. North Inlet hydrostratigraphy and the location of the four groundwater wells (GEO – 0384, 0385, 0386 and 0387). Vertical exaggeration is approximately 100x.

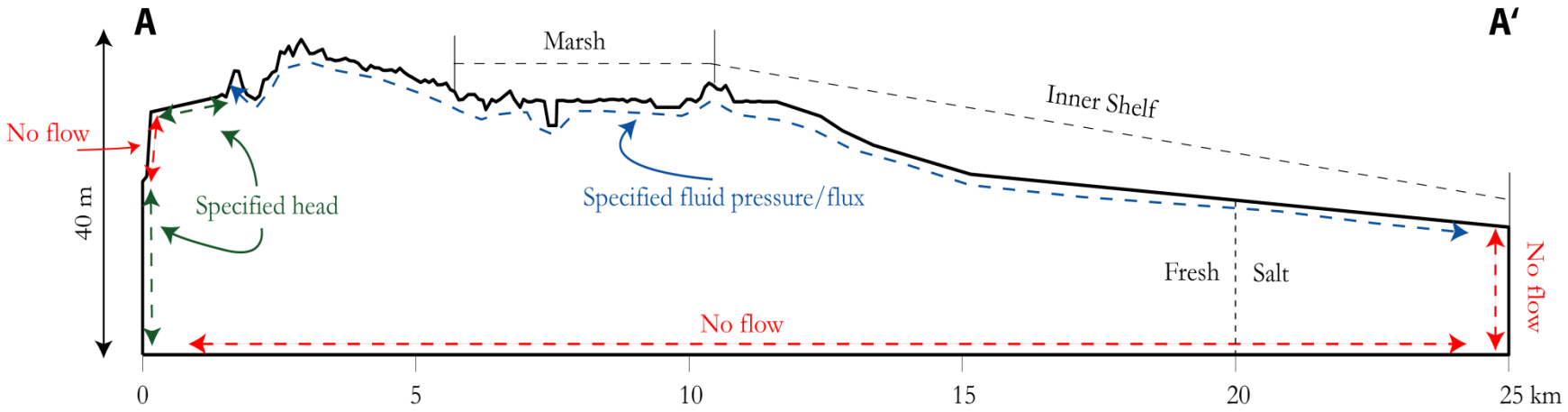

Figure 4.4. Model domain, boundary conditions, and salinity initial conditions. Vertical exaggeration is approximately 100x.

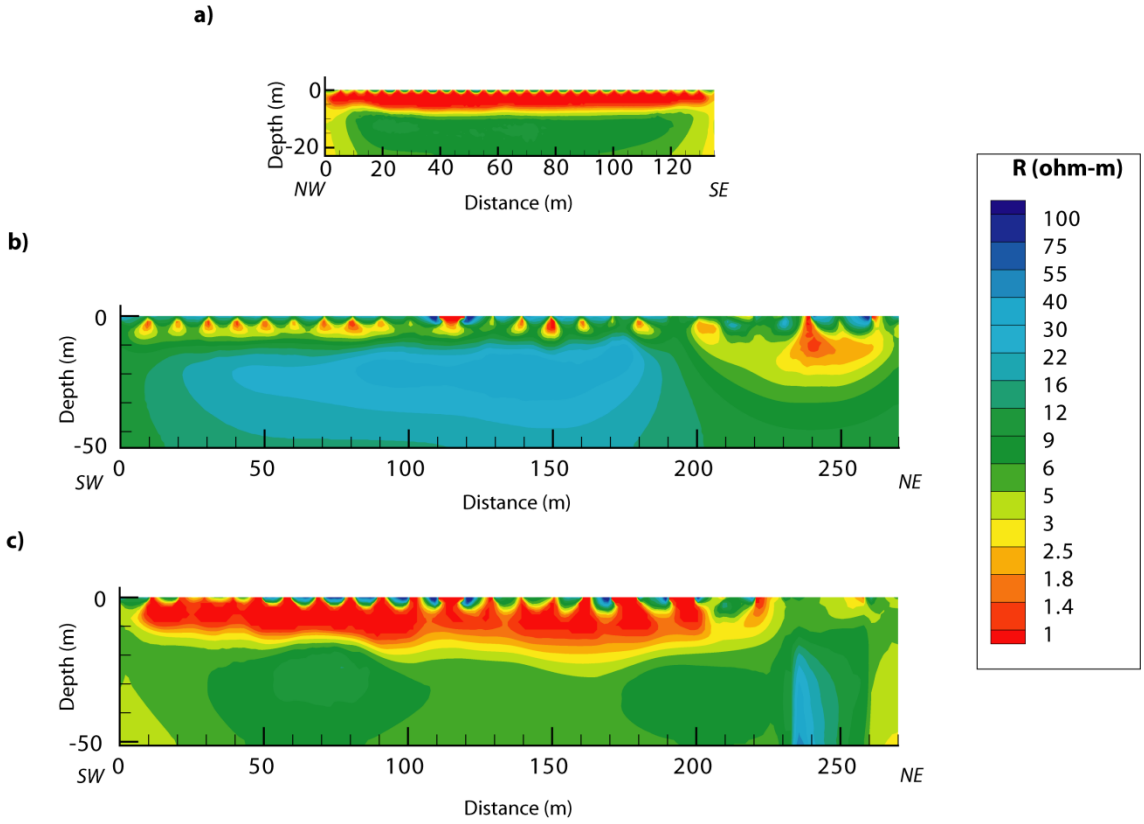

Figure 4.5. Electrical resistivity tomography surveys collected at **a)** the Crabhaul Creek Basin, **b)** Bly Island and **c)** Goat Island. Warm colors indicate low apparent resistivities, and therefore saline groundwater. Cool colors indicate high apparent resistivities, and therefore fresh groundwater

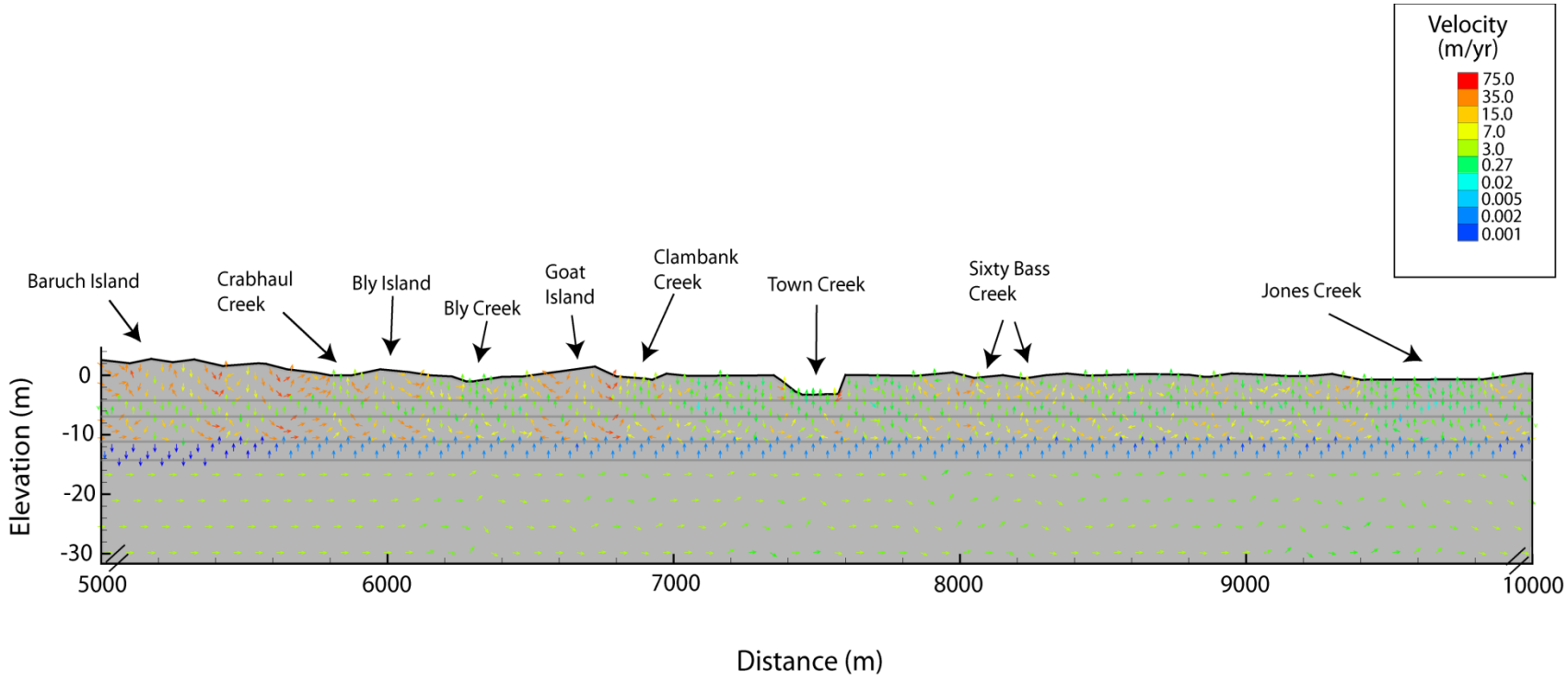

Figure 4.6. Tidally-averaged groundwater flow velocity under modern conditions for the North Inlet salt marsh. This panel represents a single 5 km sub-section of the model domain. Vertical exaggeration = 20x.

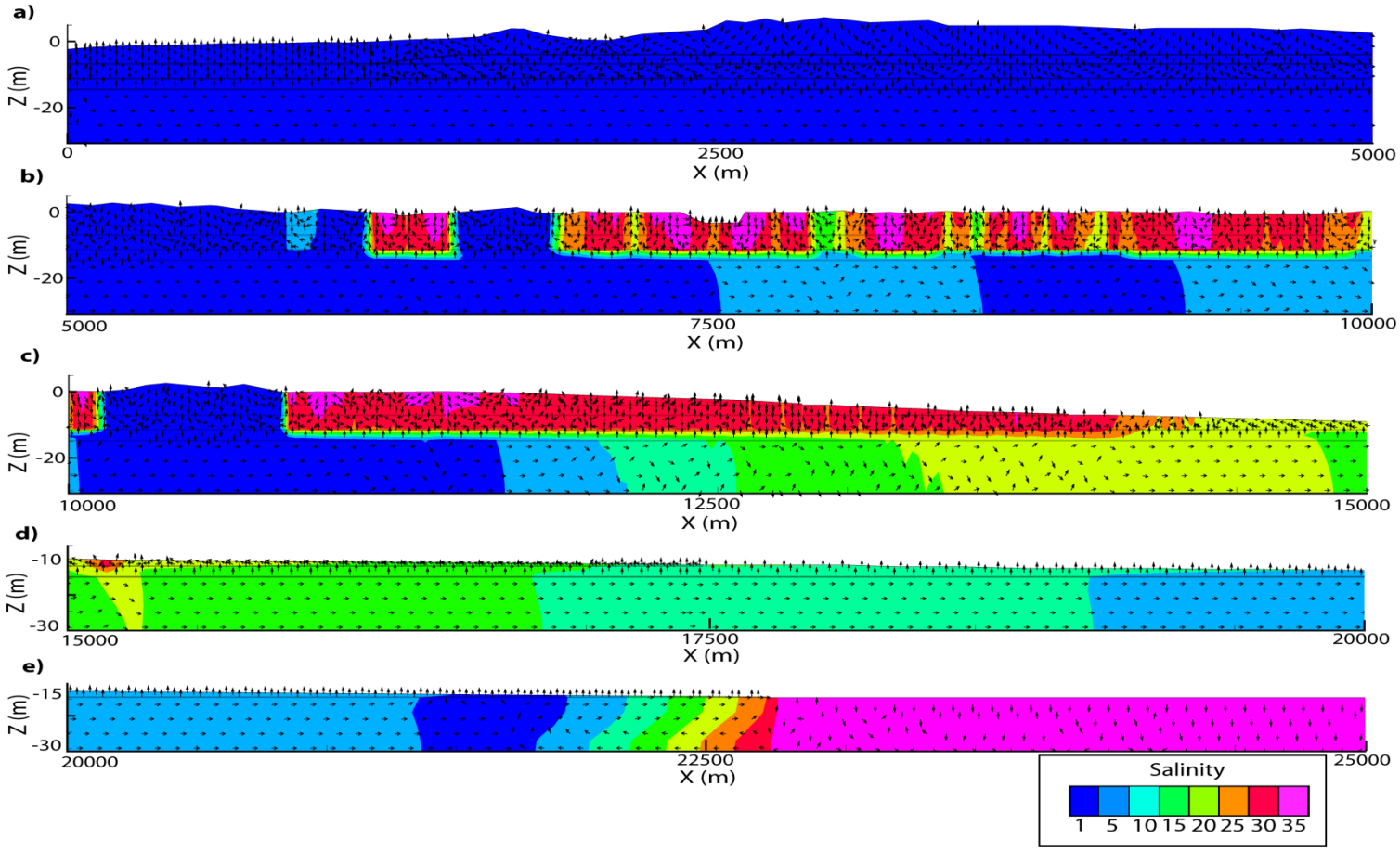

Figure 4.7. North Inlet groundwater model results for salinity and flow directions, averaged over a tidal cycle. Arrows indicate flow direction. Vertical exaggeration = 20x. Panels **a-e** display the entire length of the groundwater model segmented into 5000 m intervals from Northwest to Southeast.

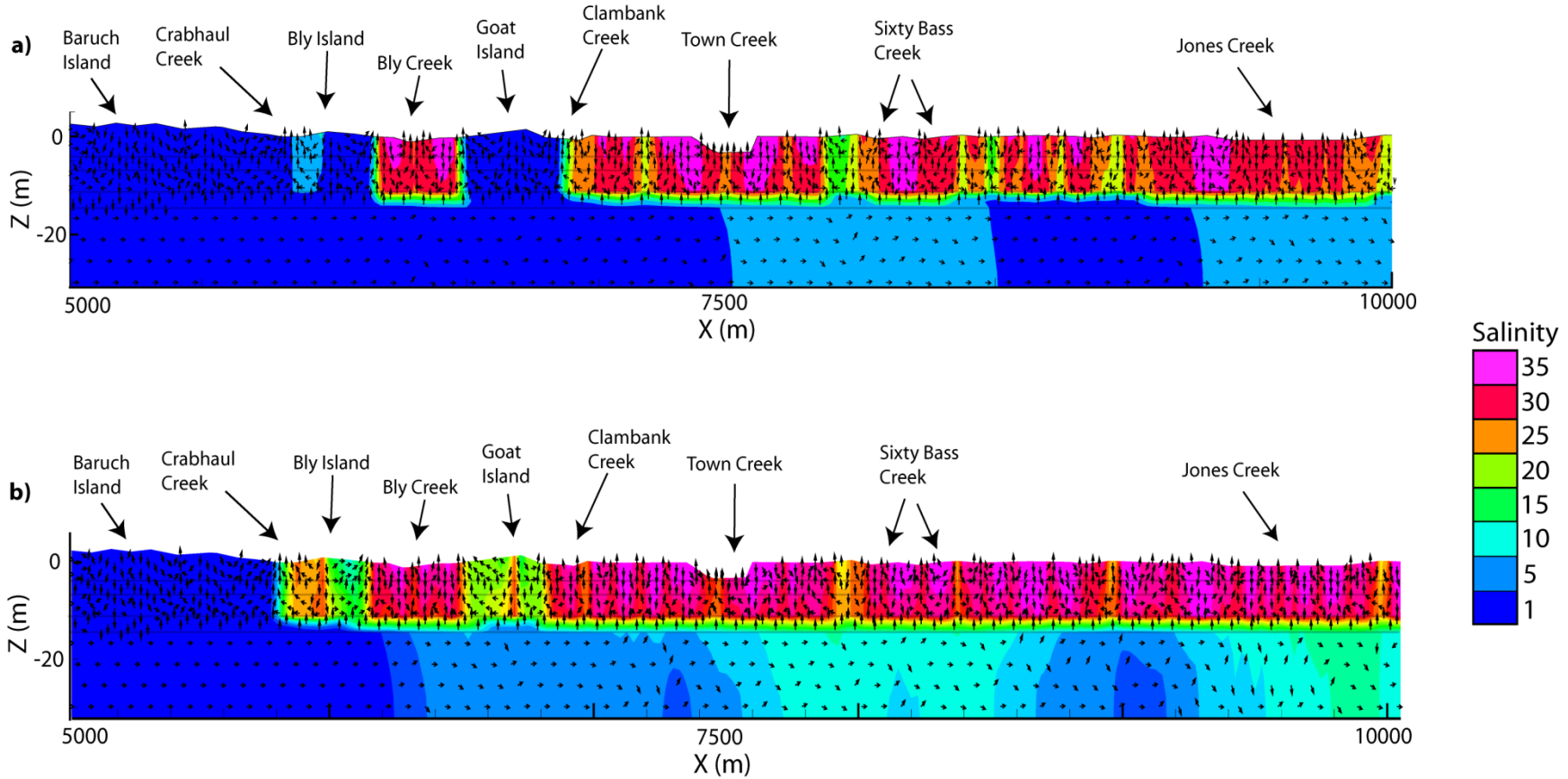

Figure 4.8. North Inlet groundwater model results for salinity and tidally-averaged flow directions in the marsh zone. **a)** Present day conditions. **b)** Year 2100, after sea-level rise of 6 mm/yr. Vertical exaggeration = 20x.

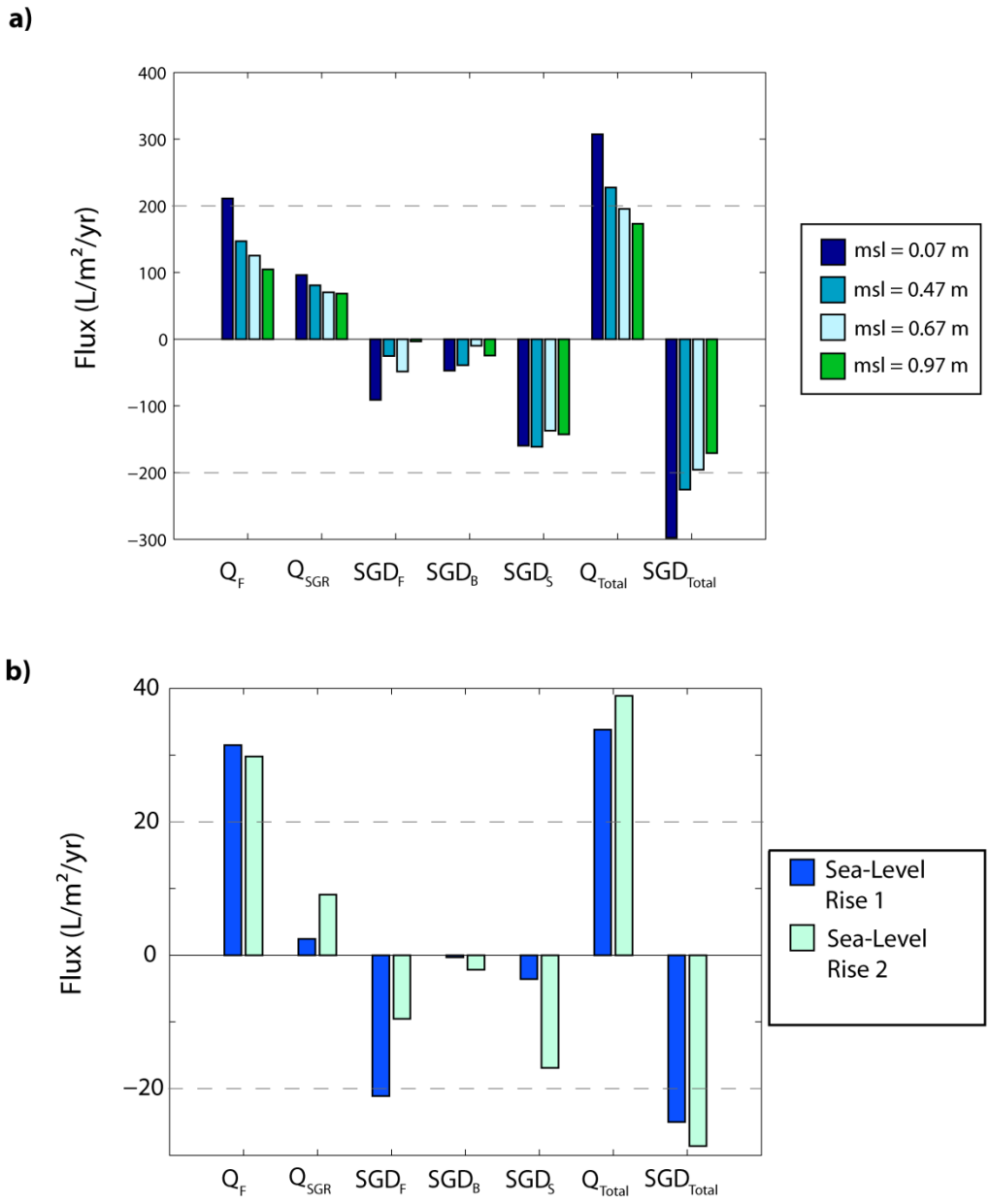

Figure 4.9. Groundwater fluxes in the marsh and inner shelf zones. **a)** Marsh zone: modern and future tidal simulations with mean sea-level elevations of 0.07, 0.47, 0.67 and 0.97 m. **b)** Inner shelf zone: past sea level rise (6.47 Kya) and the average of three future sea level rise scenarios (4, 6 and 9 mm/yr).

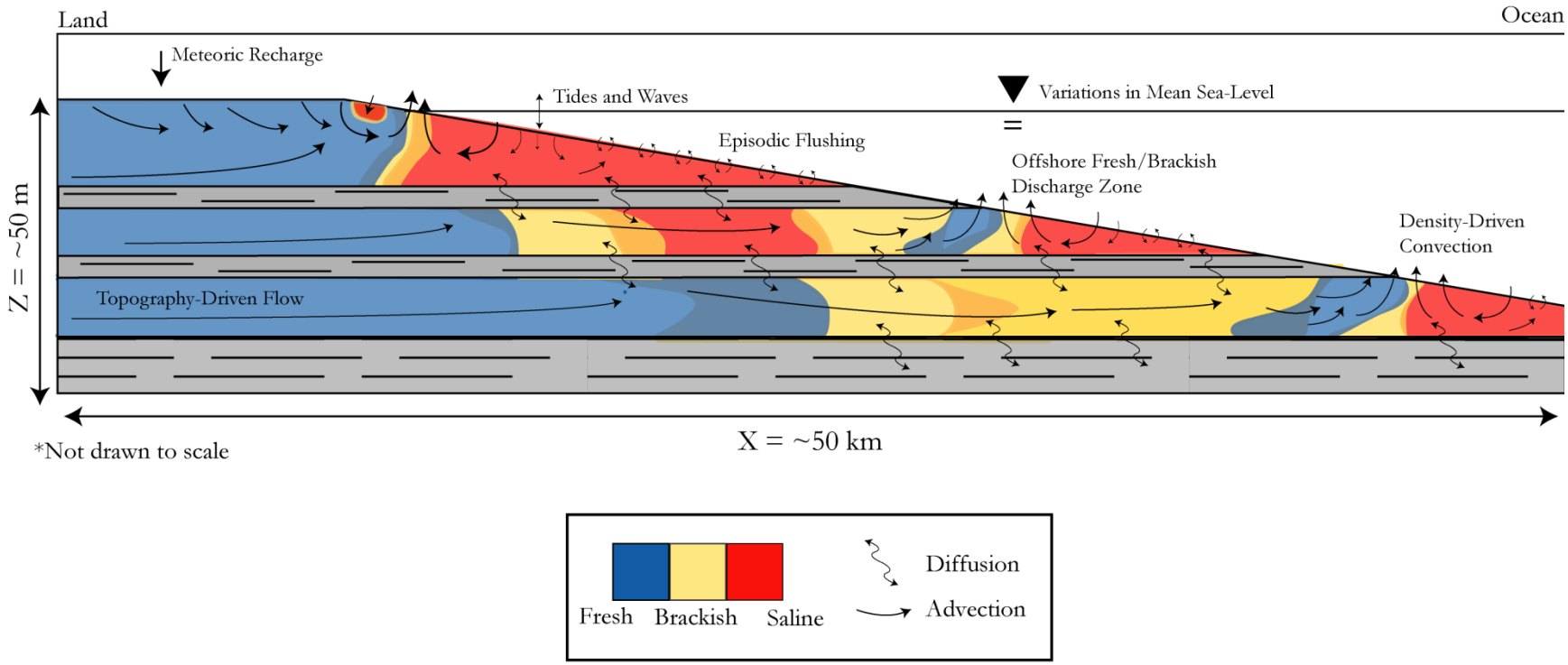

Figure 4.10. Conceptual model for integrated nearshore-embayment scale SGD for passive margins. Groundwater systems at these two scales are essentially independent. Exchange between the nearshore scale and the embayment scale is driven by diffusion over long time periods. A brackish paleowater plume exists near the terminus of major confining units and slowly discharges to the ocean.

Chapter 5

Conclusions

Coastal groundwater is a substantial topic of discussion in the modern scientific community due to the wide range of issues central to the field. Fresh groundwater reserves in aquifers within continental shelves have been well documented and purported as a future potential resource for coastal communities. The dynamics of submarine groundwater discharge and the associated freshwater-saltwater interface are also highly active research questions within the coastal groundwater discipline. The goal of this dissertation was to investigate groundwater flow systems and solute transport processes at both the nearshore and embayment scales so that a more comprehensive understanding of groundwater dynamics at the land-sea interface is possible. This final chapter provides a summary of the findings of the three separate studies that comprise this dissertation.

In the second chapter of this dissertation, I examined the effects of varying hydrologic parameters on the strength of the upper saline plume and rates of seawater recirculation in theoretical beaches. My results show that the upper saline plume may be an uncommon phenomenon that only occurs in beaches with a specific combination of hydraulic conductivity, fresh groundwater flux and beach slope. The strongest upper saline plumes develop in beaches with steeper slopes, higher influx of fresh groundwater, and hydraulic conductivities equal to 10 m/d. Median grain sediment size of the beach is strongly correlated to both hydraulic conductivity and beach slope, and therefore the strength of the upper saline plume. Finally, this study hypothesized that a field based

measurement of a saline plume salinity gradient (SPSG) could be used to provide first-order estimates of rates of tidally and density-driven recirculation in the beach aquifer.

In the third chapter of this dissertation, I compared submarine groundwater discharge and solute transport processes in a real beach on a transgressive barrier island to results from the previous theoretical study in chapter two. I found that the inclusion of real beach heterogeneity drove important deviations from predictions based on conceptual models using theoretical beach studies. The strength of the upper saline plume under Cabretta Beach was stronger than anticipated due to the presence of a buried mud layer in the beach. Saline water infiltration was greater during neap tides than spring tides due to variations in the beach profile. The strength of the upper saline plume was greatest during spring tides. Finally, I showed that field measurements of salinity gradients (SPSG) under the beach can be used to estimate rates of tidally and density driven recirculation in the beach aquifer. My results also indicated that several biogeochemical cycles recently investigated at Cabretta Beach were heavily influenced by groundwater flow.

In the fourth chapter of this dissertation, I developed a conceptual model for groundwater flow and the configuration of the freshwater-saltwater interface that spanned both the nearshore and embayment scales. I then tested how this system would respond to future predicted rates of sea-level rise. I showed that the nearshore and embayment scale aquifers were hydraulically independent. As a result, these systems responded very differently to forces such as tidal fluctuations and sea-level rise. A complex distribution of groundwater salinity developed in the first major confined aquifer (Chicora Member) which was driven by sea-level rise and slow diffusion over the mid to late Holocene.

Additionally, a plume of brackish paleo-groundwater discharged at the terminus of the Lower Bridge confining unit offshore. Simulations including modern tidal fluctuations showed that the nearshore scale SGD system contributed much higher fluxes of water to the ocean than the embayment scale. The North Inlet salt marsh contributed a SGD flux approximately 298 $L/m^2/yr$ to the coastal ocean. The inner shelf contributed only about 25 $L/m^2/yr$ (~365 $m^3/m/yr$). Finally, I showed that the nearshore scale system was highly susceptible to predicted rates of future sea-level rise and associated salinization. The embayment scale was largely unaffected by future sea-level rise. Fluxes of SGD and SGR decreased under future sea-level conditions at the nearshore scale and were relatively constant at the embayment scale.

Finally, this dissertation aimed to provide a more comprehensive understanding of the complex mechanisms for groundwater flow and solute transport at the land-sea interface. Specifically, the focus of this work was to investigate the interplay between the configuration of the freshwater-saltwater interface and groundwater flow at multiple spatial scales in both theoretical and field-based studies. My results indicate that groundwater flow and the associated solute transport are largely independent with respect to spatial scale. In general, groundwater systems at the nearshore scale did no undergo significant exchange with the embayment or shelf scales. In the unconfined, surficial aquifer, the configuration of the freshwater-saltwater interface was mostly controlled by the geomorphology of the beach and hydrologic properties of the local groundwater system. Studies investigating hydrology and geochemical processes in beaches and marshes can safely assume the impacts of the larger scale SGD systems in that environment are insignificant. Groundwater flow at the embayment scale likely has

residence times that are three to four orders of magnitude higher than flow in the shallow subsurface. As a result, the dominant drivers for flow and the potential impacts of future sea-level rise are variable with respect to spatial scale. For example, this work indicates that the nearshore scale (beaches and salt marshes) will be much more susceptible to salinization due to sea-level rise than aquifers of the embayment scale. These systems respond to changes over short time scales very rapidly. This hydraulic independence important because the complexity of coastal groundwater systems is substantial enough that many investigations focus on particular field sites or scientific questions specific to a single spatial scale. Although large, integrated studies of coastal groundwater flow may be able to provide a more comprehensive understanding for complex groundwater processes, the assumptions necessary to perform these investigations oftentimes result in conclusions that are too idealized or general. Detailed study of the complex groundwater processes at specific spatial scales is required to gain an intimate knowledge of the dynamics that control flow and material fluxes at the land-sea interface.

References

Abarca, E., Karam, H., Hemond, H.F., Harvey, C.F., 2013. Transient groundwater dynamics in a coastal aquifer: The effects of tides, the lunar cycle, and the beach profile. Water Resour. Res. 49, 2473–2488. doi:10.1002/wrcr.20075

AGI, 2009. Instruction Manual for EarthImager 2D Version 2.4.0. Resist. IP Invers. Softw. 2.4.0, 139.

Alizad, K., Hagen, S.C., Morris, J.T., Bacopoulos, P., Bilskie, M. V., Weishampel, J.F., Medeiros, S.C., 2016. A coupled, two-dimensional hydrodynamic-marsh model with biological feedback. Ecol. Modell. 327, 29–43. doi:10.1016/j.ecolmodel.2016.01.013

Anderson, J., 2010. Field Observations and Numerical Simulations of Groundwater Dynamics Within Cabretta Island, A Georgia Barrier Island. Theses Diss. 68. doi:http://scholarcommons.sc.edu/etd/310

Anderson, W.P., Evans, D.G., Snyder, S.W., 2000. The effects of Holocene barrier-island evolution on water-table elevations, Hatteras Island, North Carolina, USA. Hydrogeol. J. 8, 390–404. doi:10.1007/s100400000081

Ataie-ashtiani, B., Volker, R.E., Lockington, D.A., 1999. Tidal effects on sea water intrusion in unconfined aquifers 216, 17–31.

Aubrey, D.G., 1979. Seasonal patterns of onshore/offshore sediment movement. J. Geophys. Res. 84, 6347. doi:10.1029/JC084iC10p06347

Bakhtyar, R., Brovelli, a., Barry, D. a., Robinson, C., Li, L., 2013. Transport of variable-density solute plumes in beach aquifers in response to oceanic forcing. Adv. Water Resour. 53, 208–224. doi:10.1016/j.advwatres.2012.11.009

Bakken, T.H., Ruden, F., Mangset, L.E., 2012. Submarine Groundwater: A New Concept for the Supply of Drinking Water. Water Resour. Manag. 26, 1015–1026. doi:10.1007/s11269-011-9806-1

Bascom, W.N., 1951. The Relationship Between Sand Size and Beach-Face Slope. Am.

Geophys. Union 32, 866–874.

Baustian, J.J., Mendelssohn, I.A., Hester, M.W., 2012. Vegetation's importance in regulating surface elevation in a coastal salt marsh facing elevated rates of sea level rise. Glob. Chang. Biol. 18, 3377–3382. doi:10.1111/j.1365-2486.2012.02792.x

Boehm, A.B., Paytan, A., Shellenbarger, G.G., Davis, K. a., 2006. Composition and flux of groundwater from a California beach aquifer: Implications for nutrient supply to the surf zone. Cont. Shelf Res. 26, 269–282. doi:10.1016/j.csr.2005.11.008

Bokuniewicz, H., Pollock, M., Blum, J., Wilson, R., 2004. Submarine ground water discharge and salt penetration across the sea floor. Ground Water 42, 983–989. doi:10.1111/j.1745-6584.2004.tb02637.x

Boufadel, C., 2000. A mechanistic study of nonlinear solute transport in a groundwater-surface water system under steady state and transient hydraulic conditions. Water Resour. Res. 36, 2549–2565.

Bowen, J.L., Kroeger, K.D., Tomasky, G., Pabich, W.J., Cole, M.L., Carmichael, R.H., Valiela, I., 2007. A review of land–sea coupling by groundwater discharge of nitrogen to New England estuaries: Mechanisms and effects. Appl. Geochemistry 22, 175–191. doi:10.1016/j.apgeochem.2006.09.002

Bratton, J.F., 2010. The Three Scales of Submarine Groundwater Flow and Discharge across Passive Continental Margins. J. Geol. 118, 565–575. doi:10.1086/655114

Brown, A.C., McLachlan, A., 2002. Sandy shore ecosystems and the threats facing them: some predictions for the year 2025. Environ. Conserv. 29, 62–77. doi:10.1017/S037689290200005X

Burnett, W.C., Bokuniewicz, H., Huettel, M., Moore, W.S., Taniguchi, M., 2003. Groundwater and pore water inputs to the coastal zone. Biogeochemistry 66, 3–33. doi:10.1023/B:BIOG.0000006066.21240.53

Burnett, W.C., Taniguchi, M., Oberdorfer, J., 2001. Measurement and significance of the direct discharge of groundwater into the coastal zone. J. Sea Res. 46, 109–116. doi:10.1016/S1385-1101(01)00075-2

Campbell, B.G., Coes, A.L., 2010. Groundwater Availability in the Atlantic Coastal Plain of North and South Carolina, U.S. Geological Survey Professional Paper. doi:10.1073/pnas.0703993104

Carlston, C.W., 1963. An early American statement of the Badon Ghyben-Herzberg principle of static fresh-water-salt-water balance. Am. J. Sci. 261, 88–91.

Cartwright, N., Li, L., Nielsen, P., 2004. Response of the salt–freshwater interface in a coastal aquifer to a wave-induced groundwater pulse: field observations and modelling. Adv. Water Resour. 27, 297–303. doi:10.1016/j.advwatres.2003.12.005

Charette, M.A., Sholkovitz, E.R., 2002. Oxidative precipitation of groundwater-derived ferrous iron in the subterranean estuary of a coastal bay. Geophys. Res. Lett. 29, 1–4. doi:10.1029/2001GL014512

Choudhury, K., Saha, D.K., Chakraborty, P., 2001. Geophysical study for saline water intrusion in a coastal alluvial terrain. J. Appl. Geophys. 46, 189–200.

Cohen, D., Person, M., Wang, P., Gable, C.W., Hutchinson, D., Marksamer, A., Dugan, B., Kooi, H., Groen, K., Lizarralde, D., Evans, R.L., Day-Lewis, F.D., Lane, J.W., 2010. Origin and Extent of Fresh Paleowaters on the Atlantic Continental Shelf, USA. Ground Water 48, 143–158. doi:10.1111/j.1745-6584.2009.00627.x

Cooper, H.H., 1959. A hypothesis concerning the dynamic balance of fresh water and salt water in a coastal aquifer. J. Geophys. Res. 64, 461–467. doi:10.1029/JZ064i004p00461

Creed, C.G., 2000. Construction Slopes for Beach Nourishment Projects. J. Waterw. Port, Coastal, Ocean Eng.

D'Elia, C.F., Webb, K.L., Porter, J.W., 1981. Nitrate-rich groundwater inputs to Discovery Bay, Jamaica : A significant source of N to local coral reefs? 31, 903–910.

Davison, A.T., Nicholls, R.J., Leatherman, S.P., 1992. Beach Nourishment as a Coastal Management Tool: An Annotated Bibliography on Developments Associated with the Artificial Nourishment of Beaches. Source J. Coast. Res. J. Coast. Res. 8, 984–1022.

Du Commun, J., 1828. On the cause of fresh water springs, fountains, & c. Am. J. Sci. 14, 174–176.

Edmunds, W.M., 2001. Palaeowaters in European coastal aquifers -- the goals and main conclusions of the PALAEAUX project. Geol. Soc. London, Spec. Publ. 189, 1–16. doi:10.1144/GSL.SP.2001.189.01.02

Engelhart, S.E., Horton, B.P., 2012. Holocene sea level database for the Atlantic coast of the United States. Quat. Sci. Rev. 54, 12–25. doi:10.1016/j.quascirev.2011.09.013

Evans, T.B., Wilson, A.M., 2016. Groundwater transport and the freshwater – saltwater interface below sandy beaches. J. Hydrol. 538, 563–573. doi:10.1016/j.jhydrol.2016.04.014

Frangiamore, C., Gibbons, W., 2016. Altamaha River [WWW Document]. New Georg. Encycl. URL http://www.georgiaencyclopedia.org/articles/geography-environment/altamaha-river (accessed 9.2.16).

Freeze, R.A., Cherry, J.A., 1979. Groundwater. Prentice Hall, Englewood Cliffs, N.J.

Galeati, G., Gambolati, G., Neuman, S.P., 1992. Coupled and partially coupled Eulerian-Lagrangian Model of freshwater-seawater mixing. Water Resour. Res. 28, 149–165. doi:10.1029/91WR01927

Gardner, L.R., Porter, D.E., 2001. Stratigraphy and geologic history of a southeastern salt marsh basin North Inlet, South Carolina, USA. Wetl. Ecol. Manag. 9, 371–385. doi:10.1023/A:1012060408387

Gardner, L.R., Reeves, H.W., 2002. Spatial patterns in soil water fluxes along a forest-marsh transect in the southeastern United States. Aquat. Sci. 64, 141–155. doi:10.1007/s00027-002-8062-0

Gelhar, L.W., Welty, C., Rehfeldt, K.R., 1992. Review of Data on Field-Scale Dispersion in Aquifers based on fractal concepts. Water Resour. Res. 28, 1955–1974.

Genuchten, M.T. van, 1980. A Closed-form Equation for Predicting the Hydraulic Conductivity of Unsaturated Soils. Soil Sci. Soc. Am. J. 44, 892–898.

Ghyben, W.B., 1889. Nota in verband met de voorgenomen put boring nabij Amsterdam. Koninkl. Inst. Ing. Tijdschr 21.

GIS Department, 2016. Georgetown County Government [WWW Document]. 2005 LiDAR Acquis. URL http://www.georgetowncountysc.org/GIS_Mapping/ (accessed 1.3.16).

Glaeser, J.D., 1978. Global Distribution of Barrier Islands in Terms of Tectonic Setting. J. Geol. 86, 283–297.

Glover, R.E., 1959. The pattern of fresh water flow in a coastal aquifer. J. Geophys. Res. 64, 457–459. doi:10.1029/JZ064i004p00457

Glover, R.E., 1959. The pattern of fresh-water flow in a coastal aquifer. J. Geophys. Res. 64, 457–459. doi:10.1029/JZ064i004p00457

Groen, J., 2002. The effects of transgressions and regressions on coastal and offshore groundwater. Vrije Universiteit, Amsterdam.

Hathaway, J.C., 1979. U.S. Geological Survey Core Drilling on the Atlantic Shelf. Science (80-.). 206, 515–527.

Hayes, M.O., 1979. Barrier island morphology as a function of tidal and wave regime, in: Leatherman, S.P. (Ed.), Barrier Islands from the Gulf of St. Lawrence to the Gulf of Mexico. Academic Press, New York, pp. 1–28.

Heiss, J.W., Michael, H.A., 2014. Saltwater-freshwater mixing dynamics in a sandy beach aquifer over tidal, spring-neap, and seasonal cycles. Water Resour. Res. 2108–2123. doi:10.1002/2012WR013085.Received

Heiss, J.W., Ullman, W.J., Michael, H.A., 2014. Swash zone moisture dynamics and unsaturated infiltration in two sandy beach aquifers. Estuar. Coast. Shelf Sci. 143, 20–31. doi:10.1016/j.ecss.2014.03.015

Henry, H.R., 1959. Salt intrusion into fresh-water aquifers. J. Geophys. Res. 64, 1911–1919. doi:10.1029/JZ064i011p01911

Herzberg, A., 1901. Die Wasserversorgung einiger Nordseebader. J. Gasbeleucht. Wasserversorg 44.

Hubbert, M.K., 1940. The Theory of Ground-Water Motion. J. Geol. 48, 785–944. doi:10.1007/sl0551-009-0348-x

Huettel, M., Berg, P., Kostka, J.E., 2014. Benthic Exchange and Biogeochemical Cycling in Permeable Sediments. http://dx.doi.org/10.1146/annurev-marine-051413-012706.

Hughes, A.H., 2016. Ecohydrology and Groundwater Dynamics in a Salt Marsh Island. University of South Carolina.

Hughes, J.D., Vacher, H.L., Sanford, W.E., 2009. Temporal response of hydraulic head, temperature, and chloride concentrations to sea-level changes, Floridan aquifer system, USA. Hydrogeol. J. 17, 793–815. doi:10.1007/s10040-008-0412-0

Hughes, J.D., Vacher, H.L., Sanford, W.E., 2007. Three-dimensional flow in the Florida platform: Theoretical analysis of Kohout convection at its type locality. Geology 35, 663–666. doi:10.1130/G23374A.1

Johannes, R., 1980. The Ecological Significance of the Submarine Discharge of Groundwater. Mar. Ecol. Prog. Ser. 3, 365–373. doi:10.3354/meps003365

Kim, G., Hwang, D.-W., 2002. Tidal pumping of groundwater into the coastal ocean revealed from submarine ^{222}Rn and CH_4 monitoring. Geophys. Res. Lett. 29, 23-1-23–4. doi:10.1029/2002GL015093

Kirwan, M.L., Murray, A.B., 2007. A coupled geomorphic and ecological model of tidal marsh evolution. Proc. Natl. Acad. Sci. 104, 6118–6122. doi:10.1073/pnas.0700958104

Kohout, F.A., 1967. Ground-water flow and the geothermal regime of the Floridian Plateau. Trans. - Gulf Coast Assoc. Geol. Soc. 17, 339–354.

Kohout, F.A., 1964. The flow of fresh water and salt water in the Biscayne Aquifer of the Miami area, Florida, 161G-C. U.S. Geol. Surv., Washington, D.C.

Kohout, F.A., 1960. Cyclic flow of salt water in the Biscayne aquifer of southeastern Florida. J. Geophys. Res. 65, 2133–2141. doi:10.1029/JZ065i007p02133

Kohout, F.A., Hathaway, J.C., Folger, D.W., Bothner, M.H., Walker, E.H., Delaney, D.F., M.H., F., Weed, E.G.A. Rhodehamel, E.V.C., 1977. Fresh ground- water stored in aquifers under the continental shelf, Implications from a deep test, Nantucket Island, Massachusetts. Water Resour. Bull. 13, 373–386.

Kohout, F.A., Meisler, H., Meyer, F.W., Johnston, R.H., Leve, G.W., Wait, R.L., 1988. Hydrogeology of the Atlantic continental margin, in: Sheridan, R.E., Grow, J.A. (Eds.), The Atlantic Continental Margin. Geological Society of America, Boulder, Colorado, pp. 463–480.

Kooi, H., Groen, J., 2001. Offshore continuation of coastal groundwater systems; predictions using sharp-interface approximations and variable-density flow modelling. J. Hydrol. 246, 19–35. doi:10.1016/S0022-1694(01)00354-7

Krantz, D.E., Manheim, F.T., Bratton, J.F., Phelan, D.J., 2004. Hydrogeologic Setting and Ground Water Flow Beneath a Section of Indian River Bay, Delaware. Ground Water 42, 1035–1051. doi:10.1111/j.1745-6584.2004.tb02642.x

Krest, J.M., 2000. Marsh nutrient export supplied by groundwater discharge: Evidence from radium measurements. Global Biogeochem. Cycles 14, 167–176.

Kuan, W.K., Jin, G., Xin, P., Robinson, C., Gibbes, B., Li, L., 2012. Tidal influence on

seawater intrusion in unconfined coastal aquifers. Water Resour. Res. 48, 1–11. doi:10.1029/2011WR010678

Lebbe, L., 1999. Parameter identification in fresh-saltwater flow based on borehole resistivities and freshwater head data. Adv. Water Resour. 22, 791–806. doi:10.1016/S0309-1708(98)00054-2

Li, L., Barry, D.A., Stagnitti, F., Parlange, J.-Y., 1999. Submarine groundwater discharge and associated chemical input to a coastal sea. Water Resour. Res. 35, 3253–3259. doi:10.1029/1999WR900189

Li, L., Barry, D.A., Stagnitti, F., Parlange, J.-Y., Jeng, D.-S., 2000. Beach water table fluctuations due to spring–neap tides: moving boundary effects. Adv. Water Resour. 23, 817–824. doi:10.1016/S0309-1708(00)00017-8

Loáiciga, H.A., Pingel, T.J., Garcia, E.S., 2011. Sea water intrusion by sea-level rise: scenarios for the 21st century. Ground Water 50, 37–47. doi:10.1111/j.1745-6584.2011.00800.x

Longuet-Higgins, 1983. Wave set-up, percolation and undertow in the surf zone. Proc. R. Soc. London A 390, 283–291. doi:10.1098/rspa.1983.0132

Manheim, F.T., 1981. Patterns of Groundwater Salinity Changes in a Deep Continental-Oceanic Transect off the Southeastern Atlantic Coast of the U.S.A. J. Hydrol.

Manheim, F.T., 1968. Composition of Deeper Subsurface Waters Along the Atlantic Continental Margin. Southeast. Geol.

Manheim, F.T., Krantz, D.E., Bratton, J.F., 2004. Studying Ground Water Under Delmarva Coastal Bays Using Electrical Resistivity. Ground Water 42, 1052–1068. doi:10.1111/j.1745-6584.2004.tb02643.x

Maupin, M.A., Kenny, J.F., Hutson, S.S., Lovelace, J.K., Barber, N.L., Linsey, K.S., 2010. Estimated Use of Water in the United States in 2010. US Geol. Surv. Circ. 1405, 56. doi:http://dx.doi.org/10.3133/cir1405

McLachlan, A., Dorvlo, A., 2005. Global Patterns in Sandy Beach Macrobenthic Communities. J. Coast. Res. 214, 674–687. doi:10.2112/03-0114.1

Michael, H.A., Mulligan, A.E., Harvey, C.F., 2005. Seasonal oscillations in water exchange between aquifers and the coastal ocean. Nature 436, 1145–1148. doi:10.1038/nature03935

Michael, H.A., Russoniello, C.J., Byron, L.A., 2013. Global assessment of vulnerability to sea-level rise in topography-limited and recharge-limited coastal groundwater systems. Water Resour. Res. 49, 2228–2240. doi:10.1002/wrcr.20213

Moore, W.S., 2010a. The Effect of Submarine Groundwater Discharge on the Ocean. Ann. Rev. Mar. Sci. 2, 59–88. doi:10.1146/annurev-marine-120308-081019

Moore, W.S., 2010b. A reevaluation of submarine groundwater discharge along the southeastern coast of North America. Global Biogeochem. Cycles 24, 1–9. doi:10.1029/2009GB003747

Moore, W.S., 1998. The subterranean estuary: a reaction zone of ground water and sea water. Mar. Chem. 65, 111–125. doi:10.1016/S0304-4203(99)00014-6

Moore, W.S., 1996. Large groundwater inputs to coastal waters revealed by 226Ra enrichments. Nature. doi:10.1038/380612a0

Moore, W.S., Wilson, A.M., 2005. Advective flow through the upper continental shelf driven by storms, buoyancy, and submarine groundwater discharge, Earth and Planetary Science Letters. doi:10.1016/j.epsl.2005.04.043

Morris, J.T., 1995. The Mass Balance of Salt and Water in Intertidal Sediments: Results from North Inlet, South Carolina. Estuaries 18, 556. doi:10.2307/1352376

Morris, J.T., Sundareshwar, P. V., Nietch, C.T., Kjerfve, B., Cahoon, D.R., 2002. Responses of coastal wetlands to rising sea level. Ecology 83, 2869–2877. doi:10.1890/0012-9658(2002)083[2869:ROCWTR]2.0.CO;2

Morris, J.T., Sundberg, K., Hopkinson, C.S., 2013. Salt Marsh Primary Production and Its Response to Relative Sea Level and Nutrients in Estuaries at Plum Island, Massachusets, and North Inlet, South Carolina, USA. Oceanography 26, 78–84. doi:http://dx.doi.org/10.5670/oceanog.2013.48

National Oceanic and Atmospheric Administration; National Ocean Service; Coast Survey, 2016. Winyah Bay Nautical Map.

National Research Council, 2008. Desalination: A National Perspective. The National Academies Press, Washington, D.C. doi:10.17226/12184

Nicholls, R.J., Small, C., 2002. Improved estimates of coastal population and exposure to hazards released. Eos, Trans. Am. Geophys. Union 83, 301. doi:10.1029/2002EO000216

Nielsen, P., 1990. Tidal dynamics of the water table in beaches. Water Resour. Res. 26, 2127–2134. doi:10.1029/WR026i009p02127

Novakowski, K.I., Torres, R., Gardner, L.R., Voulgaris, G., 2004. Geomorphic analysis of tidal creek networks. Water Resour. Res. 40, n/a-n/a. doi:10.1029/2003WR002722

Oreskes, N., Shrader-Frechette, K., Belitz, K., 1994. Verification, Validation, and Confirmation of Numerical Models in the Earth Sciences. Science (80-.). 263, 641–646.

Oude Essink, G.H.P., van Baaren, E.S., de Louw, P.G.B., 2010. Effects of climate change on coastal groundwater systems: A modeling study in the Netherlands. Water Resour. Res. 46, n/a-n/a. doi:10.1029/2009WR008719

Paytan, A., Shellenbarger, G.G., Street, J.H., Gonneea, M.E., Davis, K., Young, M.B., Moore, W.S., 2006. Submarine groundwater discharge: An important source of new inorganic nitrogen to coral reef ecosystems. Limnol. Oceanogr. 51, 343–348. doi:10.4319/lo.2006.51.1.0343

Person, M., Dugan, B., Swenson, J.B., Urbano, L., Library, L., Street, W., York, N., Stott, C., Willett, M., 2003. Pleistocene hydrogeology of the Atlantic continental shelf , New England. GSA Bull. 1324–1343.

Petkewich, M.D., Parkhurst, D.L., Conlon, K.J., Campbell, B.G., Mirecki, J.E., 2004. Hydrologic and geochemical evaluation of aquifer storage recovery in the Santee Limestone/Black Mingo aquifer, Charleston, South Carolina, 1998–2002, U.S. Geological Survey Scientific Investigations Report. doi:10.1017/CBO9781107415324.004

Post, V., Groen, J., Kooi, H., Person, M., Ge, S., Edmunds, W.M., 2013. Offshore fresh groundwater reserves as a global phenomenon. Nature 504, 71–8. doi:10.1038/nature12858

Rahmstorf, S., 2006. A Semi-Empirical Approach to Projecting Future Sea-Level Rise. Science (80-.). 315, 368–370. doi:10.1126/science.1135456

Rahmstorf, S., Foster, G., Cazenave, A., 2012. Comparing climate projections to observations up to 2011. Environ. Res. Lett. 7, 1–5. doi:10.1088/1748-9326/7/4/044035

Robinson, C., Gibbes, B., Carey, H., Li, L., 2007a. Salt-freshwater dynamics in a subterranean estuary over a spring-neap tidal cycle. J. Geophys. Res. 112, 1–15. doi:10.1029/2006JC003888

Robinson, C., Gibbes, B., Li, L., 2006. Driving mechanisms for groundwater flow and salt transport in a subterranean estuary. Geophys. Res. Lett. 33, 3–6. doi:10.1029/2005GL025247

Robinson, C., Li, L., Barry, D. a., 2007b. Effect of tidal forcing on a subterranean estuary. Adv. Water Resour. 30, 851–865. doi:10.1016/j.advwatres.2006.07.006

Robinson, C., Li, L., Prommer, H., 2007c. Tide-induced recirculation across the aquifer-ocean interface. Water Resour. Res. 43, 1–14. doi:10.1029/2006WR005679

Robinson, C., Xin, P., Li, L., Barry, D.A., 2014. Groundwater flow and salt transport in a subterranean estuary driven by intensified wave conditions. Water Resour. Res. 50, 165–181. doi:10.1002/2013WR013813

Robinson, M., Gallagher, D., Reay, W., 1998. Field Observations of Tidal and Seasonal Variations in Ground Water Discharge to Tidal Estuarine Surface Water. Ground Water Monit. Remediat. 18, 83–92. doi:10.1111/j.1745-6592.1998.tb00605.x

Santos, I.R., Burnett, W.C., Dittmar, T., Suryaputra, I.G.N.A., Chanton, J., 2009. Tidal pumping drives nutrient and dissolved organic matter dynamics in a Gulf of Mexico subterranean estuary. Geochim. Cosmochim. Acta 73, 1325–1339. doi:10.1016/j.gca.2008.11.029

Santos, I.R., Burnett, W.C., Misra, S., Suryaputra, I.G.N.A., Chanton, J.P., Dittmar, T., Peterson, R.N., Swarzenski, P.W., 2011. Uranium and barium cycling in a salt wedge subterranean estuary: The influence of tidal pumping. Chem. Geol. 287, 114–123. doi:10.1016/j.chemgeo.2011.06.005

Santos, I.R., Erler, D., Tait, D., Eyre, B.D., 2010. Breathing of a coral cay: Tracing tidally driven seawater recirculation in permeable coral reef sediments. J. Geophys. Res. Ocean. 115, C12010. doi:10.1029/2010JC006510

Santos, I.R., Eyre, B.D., Huettel, M., 2012. The driving forces of porewater and groundwater flow in permeable coastal sediments: A review. Estuar. Coast. Shelf Sci. 98, 1–15. doi:10.1016/j.ecss.2011.10.024

Schutte, C.A., Joye, S.B., Wilson, A.M., Evans, T., Moore, W.S., Casciotti, K., 2015.

Intense nitrogen cycling in permeable intertidal sediment revealed by a nitrous oxide hot spot. Global Biogeochem. Cycles 29, 1584–1598. doi:10.1002/2014GB005052

Schutte, C.A., Wilson, A.M., Evans, T., Moore, W.S., Joye, S.B., 2016. Methanotrophy controls groundwater methane export from a barrier island. Geochim. Cosmochim. Acta 179, 242–256. doi:10.1016/j.gca.2016.01.022

Shaw, T.J., Moore, W.S., Kloepfer, J., Sochaski, M.A., 1998. The flux of barium to the coastal waters of the southeastern USA: the importance of submarine groundwater discharge. Geochim. Cosmochim. Acta 62, 3047–3054. doi:10.1016/S0016-7037(98)00218-X

Slomp, C.P., Van Cappellen, P., 2004. Nutrient inputs to the coastal ocean through submarine groundwater discharge: Controls and potential impact. J. Hydrol. 295, 64–86. doi:10.1016/j.jhydrol.2004.02.018

Smith, A.J., 2004. Mixed convection and density-dependent seawater circulation in coastal aquifers. Water Resour. Res. 40, n/a-n/a. doi:10.1029/2003WR002977

Sorensen, R.M., 2006. Basic Coastal Engineering, 3rd ed, Basic Coastal Engineering. Springer US, Boston. doi:10.1007/0-387-23333-4_2

Spiteri, C., Regnier, P., Slomp, C.P., Charette, M.A., 2006. pH-Dependent iron oxide precipitation in a subterranean estuary. J. Geochemical Explor. 88, 399–403. doi:10.1016/j.gexplo.2005.08.084

Sun, H., 1997. A two-dimensional analytical solution of groundwater response to tidal loading in an estuary. Water Resour. Res. 33, 1429–1435. doi:10.1029/97WR00482

Taniguchi, M., Iwakawa, H., 2004. Submarine groundwater discharge in Osaka Bay, Japan. Limnology 5, 25–32. doi:10.1007/s10201-003-0112-3

Thibodeau, P.M., Gardner, L.R., Reeves, H.W., 1998. The role of groundwater flow in controlling the spatial distribution of soil salinity and rooted macrophytes in a southeastern salt marsh, USA. Mangroves Salt Marshes 2, 1–13. doi:10.1023/A:1009910712539

Thorn, P., Urish, D., 2013. Preliminary observation of complex salt-fresh water mixing in a beach aquifer. GroundWater 51, 145–150. doi:10.1111/j.1745-6584.2012.00947.x

Uchiyama, Y., Nadaoka, K., Rolke, P., Adachi, K., Yagi, H., 2000. Submarine groundwater discharge into the sea and associated nutrient transport in a sandy

beach. Water Resour. Res. 36, 1467–1479. doi:10.1029/2000WR900029

Ullman, W.J., Chang, B., Miller, D.C., Madsen, J. a, 2003. Groundwater mixing, nutrient diagenesis, and discharges across a sandy beachface, Cape Henlopen, Delaware (USA). Estuar. Coast. Shelf Sci. 57, 539–552. doi:10.1016/S0272-7714(02)00398-0

UNESCO/ICES/SCOR/IAPSO, 1981. UNESCO Technical Papers in Marine Science 144.

Valiela, I., Costa, J., Foreman, K., Teal, J.M., Howes, B., Aubrey, D., 1990. Transport of groundwater-borne nutrients from watersheds and their effects on coastal waters. Biogeochemistry 10, 177–197. doi:10.1007/BF00003143

Vandenbohede, A., Lebbe, L., 2006. Occurrence of salt water above fresh water in dynamic equilibrium in a coastal groundwater flow system near De Panne, Belgium. Hydrogeol. J. 14, 462–472. doi:10.1007/s10040-005-0446-5

Voss, C.I., Provost, A.M., 2002. SUTRA. A model for saturated–unsaturated variable-density ground-water flow with solute or energy transport.

Wentworth, C.K., 1948. Growth of the Ghyben-Herzberg transition zone under a rinsing hypothesis. Am. Geophys. Union Trans. 29, 97–98.

Werner, A.D., Simmons, C.T., 2009. Impact of Sea-Level Rise on Sea Water Intrusion in Coastal Aquifers. Ground Water 47, 197–204. doi:10.1111/j.1745-6584.2008.00535.x

Whiting, G.J., Childers, D.L., 1989. Subtidal advective water flux as a potentially important nutrient input to southeastern U.S.A. Saltmarsh estuaries. Estuar. Coast. Shelf Sci. 28, 417–431. doi:10.1016/0272-7714(89)90089-9

Wilson, A.M., 2003. The occurrence and chemical implications of geothermal convection of seawater in continental shelves. Geophys. Res. Lett. 30, 2127. doi:10.1029/2003GL018499

Wilson, A.M., Evans, T.B., Moore, W.S., Schutte, C.A., Joye, S.B., 2015. What time scales are important formonitoring tidally influenced submarine groundwater discharge? Insights froma salt marsh. Water Resour. Res. 51, 4198–4207. doi:10.1002/2014WR015984

Wilson, A.M., Gardner, L.R., 2006. Tidally driven groundwater flow and solute exchange in a marsh: Numerical simulations. Water Resour. Res. 42, n/a-n/a.

doi:10.1029/2005WR004302

Wilson, A.M., Huettel, M., Klein, S., 2008. Grain size and depositional environment as predictors of permeability in coastal marine sands. Estuar. Coast. Shelf Sci. 80, 193–199. doi:10.1016/j.ecss.2008.06.011

Wilson, A.M., Moore, W.S., Joye, S.B., Anderson, J.L., Schutte, C. a., 2011. Storm-driven groundwater flow in a salt marsh. Water Resour. Res. 47, 1–11. doi:10.1029/2010WR009496

Wilson, A.M., Ruppel, C., 2007. Salt tectonics and shallow subseafloor fluid convection: models of coupled fluid-heat-salt transport. Geofluids 7, 377–386. doi:10.1111/j.1468-8123.2007.00191.x

Winston, R.B., 2014. Modifications made to ModelMuse to add support for the Saturated-Unsaturated Transport model (SUTRA). doi:http://dx.doi.org/10.3133/tm6a49

Xin, P., Robinson, C., Li, L., Barry, D. a., Bakhtyar, R., 2010. Effects of wave forcing on a subterranean estuary. Water Resour. Res. 46, 1–17. doi:10.1029/2010WR009632

Yuqun Xue, Chunhong Xie, Jichun Wu, Peimin Liu, Jianji Wang, Qingbo Jiang, 1995. A three-dimensional miscible transport model for seawater intrusion in China. Water Resour. Res. doi:10.1029/94WR02379

Appendix A

Permission to Reprint

licensing transaction, (ii) these terms and conditions and (iii) CCC's Billing and Payment terms and conditions.
8. License Contingent Upon Payment: While you may exercise the rights licensed immediately upon issuance of the license at the end of the licensing process for the transaction, provided that you have disclosed complete and accurate details of your proposed use, no license is finally effective unless and until full payment is received from you (either by publisher or by CCC) as provided in CCC's Billing and Payment terms and conditions. If full payment is not received on a timely basis, then any license preliminarily granted shall be deemed automatically revoked and shall be void as if never granted. Further, in the event that you breach any of these terms and conditions or any of CCC's Billing and Payment terms and conditions, the license is automatically revoked and shall be void as if never granted. Use of materials as described in a revoked license, as well as any use of the materials beyond the scope of an unrevoked license, may constitute copyright infringement and publisher reserves the right to take any and all action to protect its copyright in the materials.
9. Warranties: Publisher makes no representations or warranties with respect to the licensed material.
10. Indemnity: You hereby indemnify and agree to hold harmless publisher and CCC, and their respective officers, directors, employees and agents, from and against any and all claims arising out of your use of the licensed material other than as specifically authorized pursuant to this license.
11. No Transfer of License: This license is personal to you and may not be sublicensed, assigned, or transferred by you to any other person without publisher's written permission.

12. No Amendment Except in Writing: This license may not be amended except in a writing signed by both parties (or, in the case of publisher, by CCC on publisher's behalf).
13. Objection to Contrary Terms: Publisher hereby objects to any terms contained in any purchase order, acknowledgment, check endorsement or other writing prepared by you, which terms are inconsistent with these terms and conditions or CCC's Billing and Payment terms and conditions. These terms and conditions, together with CCC's Billing and Payment terms and conditions (which are incorporated herein), comprise the entire agreement between you and publisher (and CCC) concerning this licensing transaction. In the event of any conflict between your obligations established by these terms and conditions and those

and made available only to
bona fide students registered on a relevant course. This permission is granted for 1 year only.
You may obtain a new license for future website posting.
17. For journal authors: the following clauses are applicable in addition to the above:
Preprints:
A preprint is an author's own writeup
of research results and analysis, it has not been peerreviewed,
nor has it had any other value added to it by a publisher (such as formatting,
copyright, technical enhancement etc.).
Authors can share their preprints anywhere at any time. Preprints should not be added to or
enhanced in any way in order to appear more like, or to substitute for, the final versions of
articles however authors can update their preprints on arXiv or RePEc with their Accepted
Author Manuscript (see below).
If accepted for publication, we encourage authors to link from the preprint to their formal publication via its DOI. Millions of researchers have access to the formal publications on ScienceDirect, and so links will help users to find, access, cite and use the best available

version. Please note that Cell Press, The Lancet and some societyowned
have different
preprint policies. Information on these policies is available on the journal homepage.
Accepted Author Manuscripts: An accepted author manuscript is the manuscript of an article that has been accepted for publication and which typically includes authorincorporated
changes suggested during submission, peer review and editorauthor
communications.
Authors can share their accepted author manuscript:
immediately
via their noncommercial
person homepage or blog
by updating a preprint in arXiv or RePEc with the accepted manuscript
via their research institute or institutional repository for internal institutional
uses or as part of an invitationonly
research collaboration workgroup
directly by providing copies to their students or to research collaborators for
their personal use
for private scholarly sharing as part of an invitationonly
work group on
commercial sites with which Elsevier has an agreement
after
the embargo period
via noncommercial
hosting platforms such as their institutional repository

via commercial sites with which Elsevier has an agreement
In all cases accepted manuscripts should:
link
to the formal publication via its DOI
bear
a CCBYNCND
license this
is easy to do
if
aggregated with other manuscripts, for example in a repository or other site, be
shared in alignment with our hosting policy not be added to or enhanced in any way to
appear more like, or to substitute for, the published journal article.
Published journal article (JPA): A published journal article (PJA) is the definitive final
record of published research that appears or will appear in the journal and embodies all
valueadding
publishing activities including peer review coordination,
copyediting,
formatting, (if relevant) pagination and online enrichment.
Policies for sharing publishing journal articles differ for subscription and gold open access
articles:
Subscription Articles: If you are an author, please share a link to your article rather than the
fulltext.
Millions of researchers have access to the formal publications on ScienceDirect,
and so links will help your users to find, access, cite, and use the best available version.
Theses and dissertations which contain embedded PJAs as part of the formal submission can
be posted publicly by the awarding institution with DOI links back to the formal
publications on ScienceDirect.
If you are affiliated with a library that subscribes to ScienceDirect you have additional
private sharing rights for others' research accessed under that agreement. This includes use
for classroom teaching and internal training at the institution (including use in course packs
and courseware programs), and inclusion of the article for grant funding purposes.
Gold Open Access Articles: May be shared according to the authorselected
enduser
license and should contain a CrossMark logo, the end user license, and a DOI link to the
formal publication on ScienceDirect.
Please refer to Elsevier's posting policy for further information.
18. For book authors the following clauses are applicable in addition to the above:
Authors are permitted to place a brief summary of their work online only. You are not
allowed to download and post the published electronic version of your chapter, nor may
you

scan the printed edition to create an electronic version. Posting to a repository: Authors are
permitted to post a summary of their chapter only in their institution's repository.

19. Thesis/Dissertation: If your license is for use in a thesis/dissertation your thesis may be
submitted to your institution in either print or electronic form. Should your thesis be published commercially, please reapply for permission. These requirements include permission for the Library and Archives of Canada to supply single copies, on demand, of
the complete thesis and include permission for Proquest/UMI to supply single copies, on demand, of the complete thesis. Should your thesis be published commercially, please reapply for permission. Theses and dissertations which contain embedded PJAs as part of the formal submission can be posted publicly by the awarding institution with DOI links back to the formal publications on ScienceDirect.
Elsevier Open Access Terms and Conditions
You can publish open access with Elsevier in hundreds of open access journals or in nearly
2000 established subscription journals that support open access publishing. Permitted third
party reuse
of these open access articles is defined by the author's choice of Creative
Commons user license. See our open access license policy for more information.
Terms & Conditions applicable to all Open Access articles published with Elsevier:
Any reuse of the article must not represent the author as endorsing the adaptation of the article nor should the article be modified in such a way as to damage the author's honour or
reputation. If any changes have been made, such changes must be clearly indicated.
The author(s) must be appropriately credited and we ask that you include the end user license and a DOI link to the formal publication on ScienceDirect.
If any part of the material to be used (for example, figures) has appeared in our publication
with credit or acknowledgement to another source it is the responsibility of the user to ensure their reuse complies with the terms and conditions determined by the rights holder.
Additional Terms & Conditions applicable to each Creative Commons user license:
CC BY: The CCBY
license allows users to copy, to create extracts, abstracts and new
works from the Article, to alter and revise the Article and to make commercial use of the Article (including reuse and/or resale of the Article by commercial entities), provided the user gives appropriate credit (with a link to the formal publication through the relevant DOI), provides a link to the license, indicates if changes were made and the licensor is not
represented as endorsing the use made of the work. The full details of the license are available at http://creativecommons.org/licenses/by/4.0.
CC BY NC SA: The CC BYNCSA

Appendix B

Supplemental Material

S1. Baruch Island Stratigraphy

The Williamsburg Formation is a late Paleocene age (55 Ma) sediment package that was deposited in inner shelf and marginal-marine depositional environments (Campbell and Coes, 2010; Petkewich et al., 2004). The Williamsburg Formation, along with the underlying Rhems Formation belong to the Black Mingo Group, which is colloquially referred to as the Tertiary sands (Petkewich et al., 2004). At its type section, the Williamsburg formation is comprised of sandy shale, fossiliferous clayey sand (Lower Bridge Member), and a moldic quartz-bearing pelecypod limestone (Chicora Member) (Campbell and Coes, 2010; Petkewich et al., 2004). The underlying Rhems Formation is comprised mostly of opaline claystone at the type section (Campbell and Coes, 2010). At our study site, the Chicora Member limestone is the first major confined aquifer of the embayment scale and is also referred to as the Gordon aquifer, which is the lowermost aquifer of the Floridan aquifer system (Campbell and Coes, 2010). The overlying Santee Limestone and Ocala Limestone (Middle and Upper Floridan respectively) are both missing at North Inlet due to stratigraphic pinch out associated with the uplift of the Cape Fear Arch. Sediment logs from the SCDNR borehole GEO-380 indicate the Chicora Member limestone is underlain by interbedded sequences of mudstone and siltstone, referred to as the Crouch Branch confining unit (Campbell and Coes, 2010).

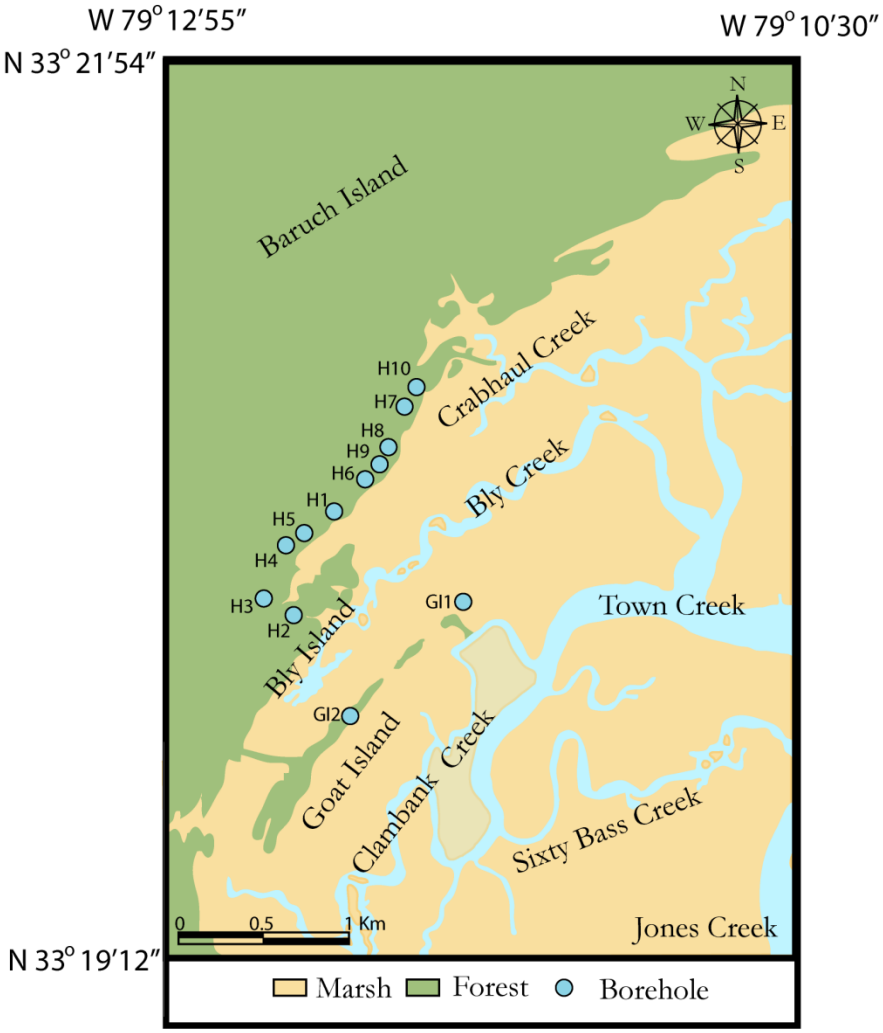

Figure B.1. Baruch Borehole locations. H = Hobcaw, GI = Goat Island.

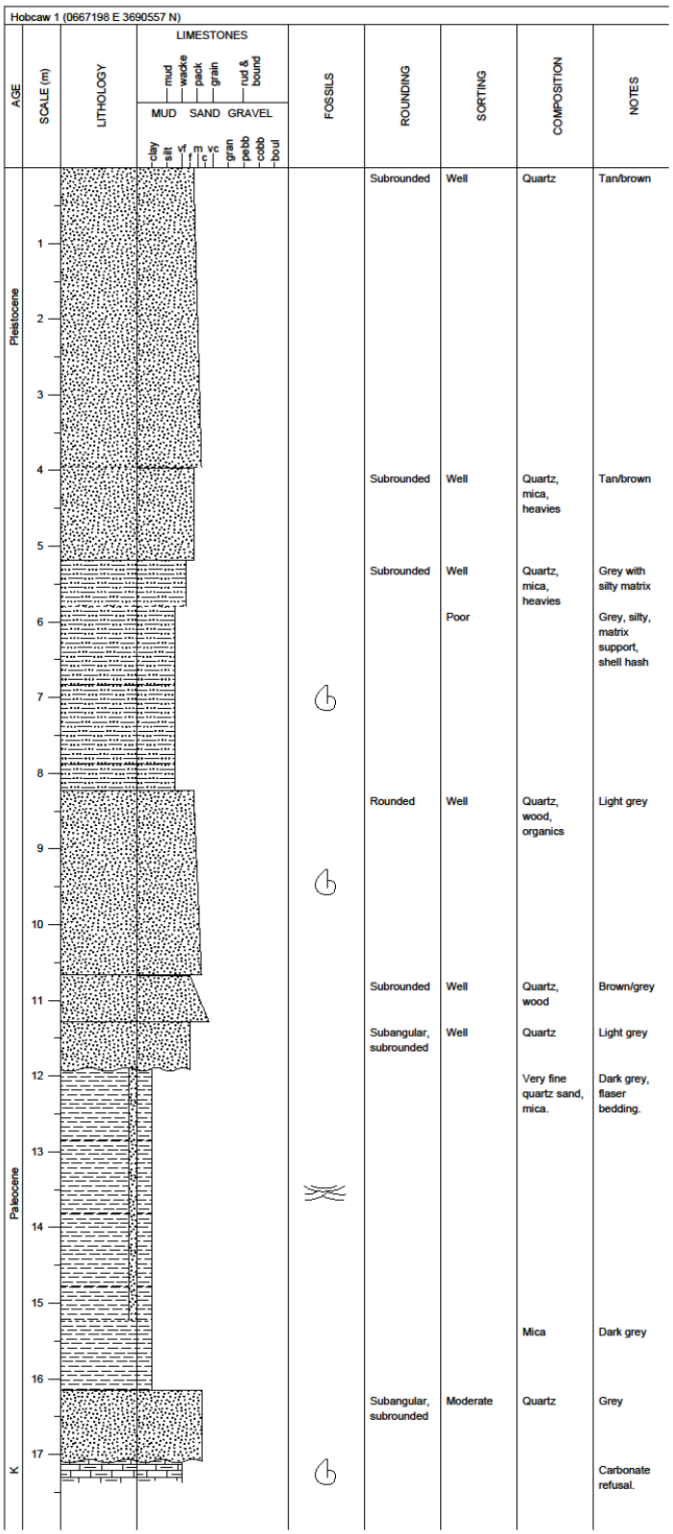

Figure B.2. Hobcaw 1 sediment log.

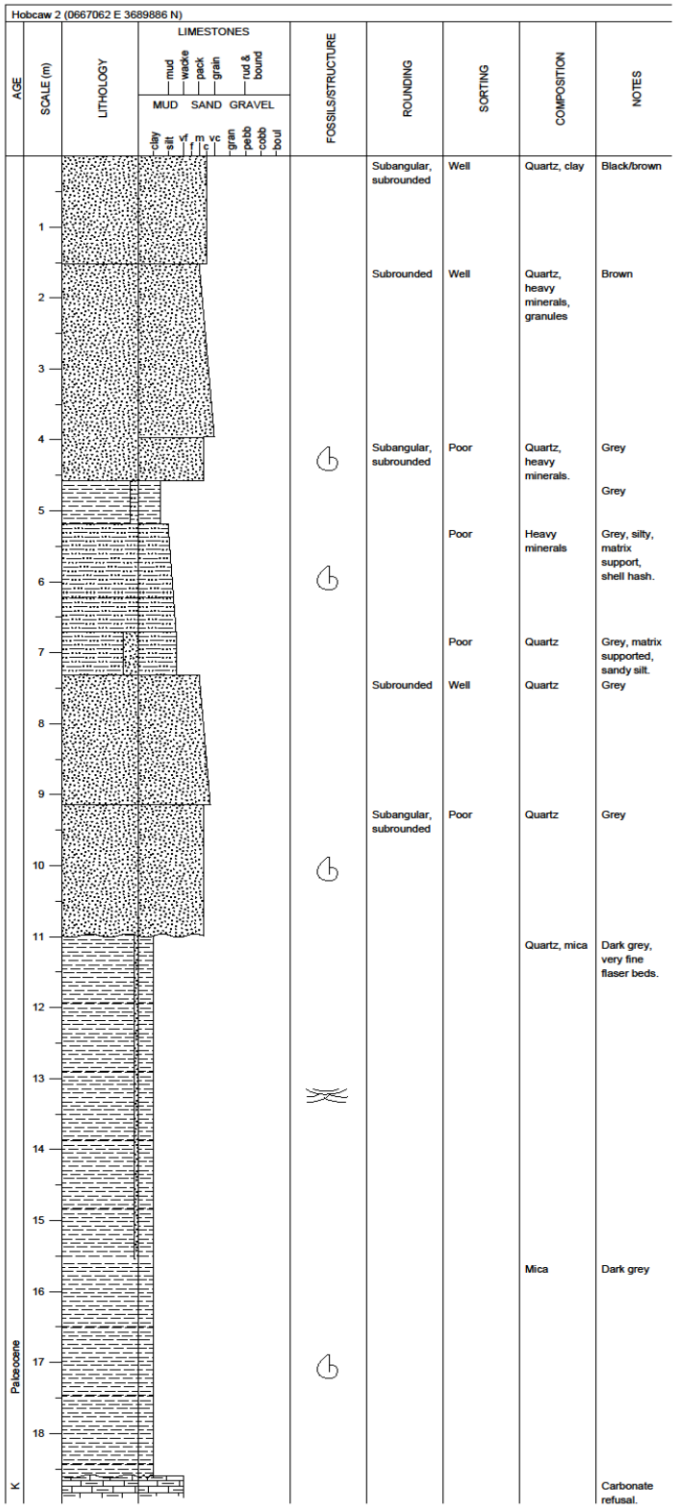

Figure B.3. Hobcaw 2 sediment log.

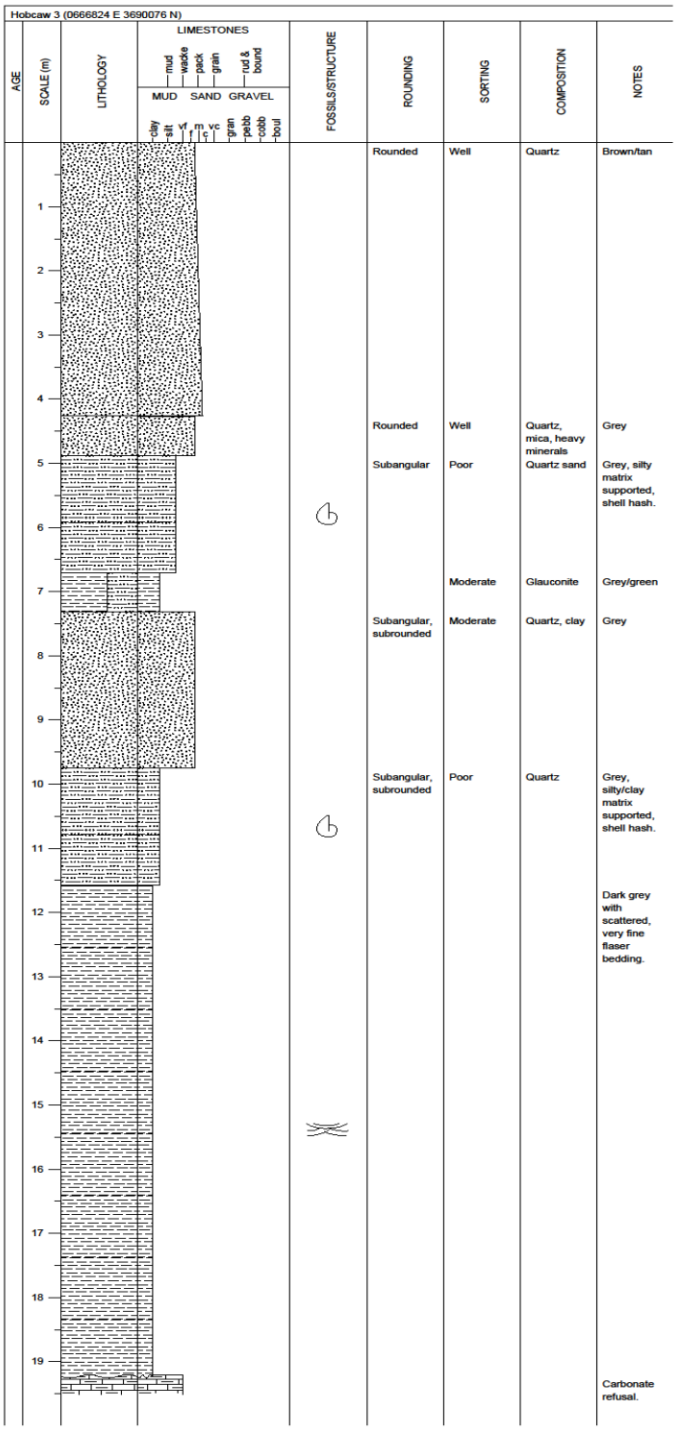

Figure B.4. Hobcaw 3 sediment log.

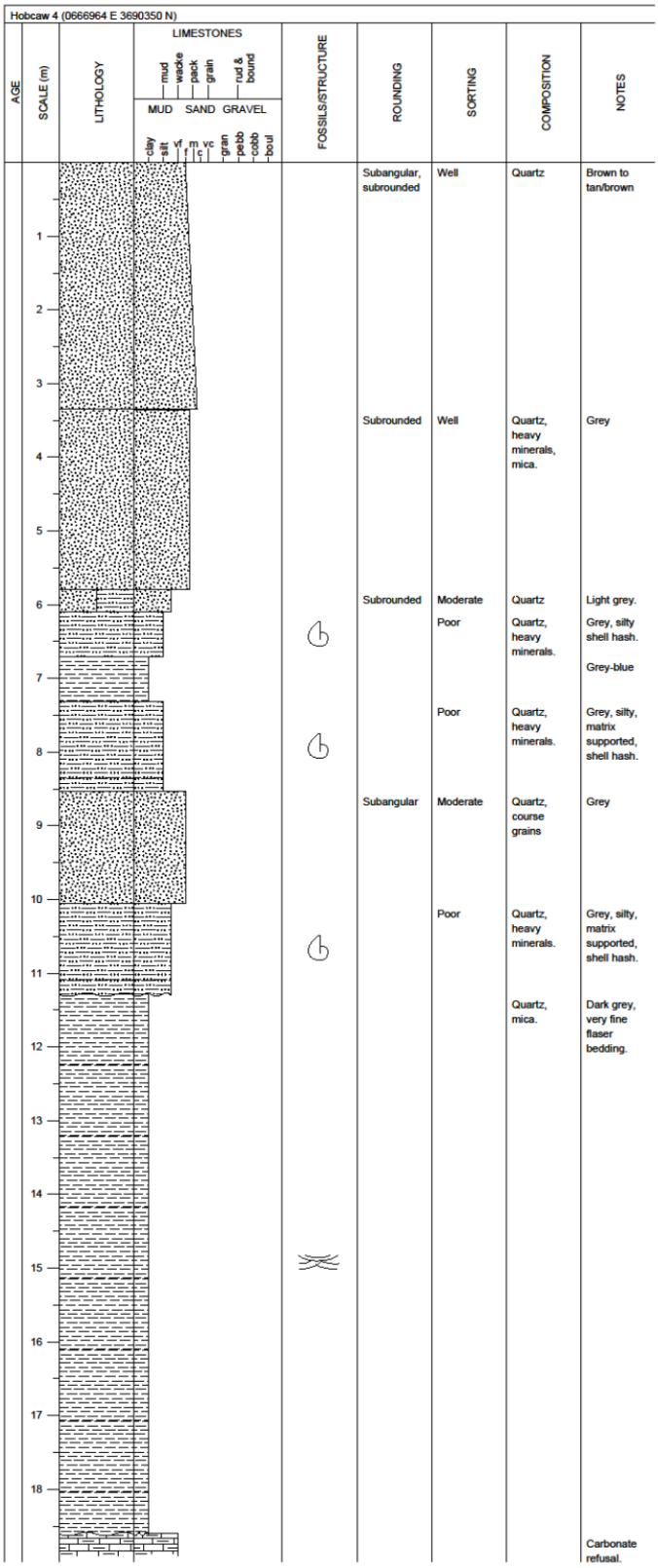

Figure B.5. Hobcaw 4 sediment log.

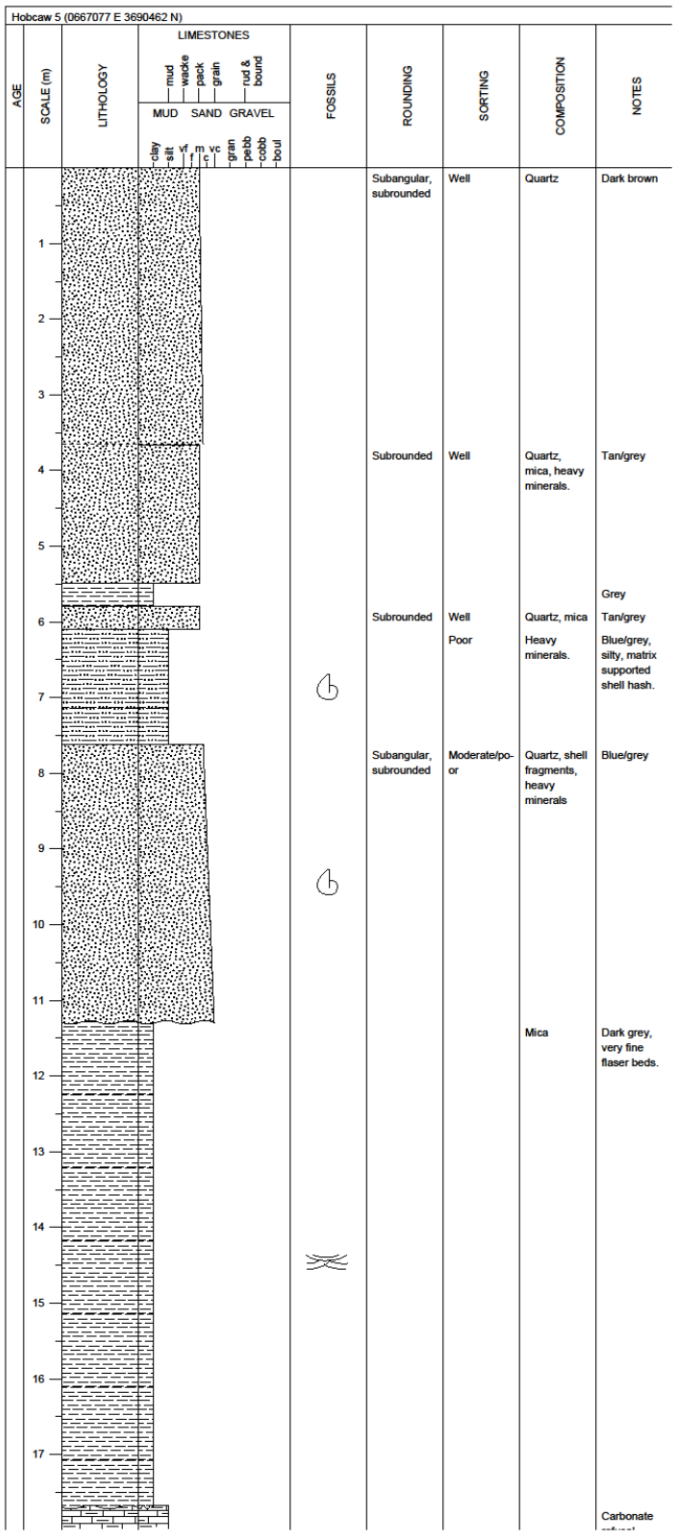

Figure B.6. Hobcaw 5 sediment log.

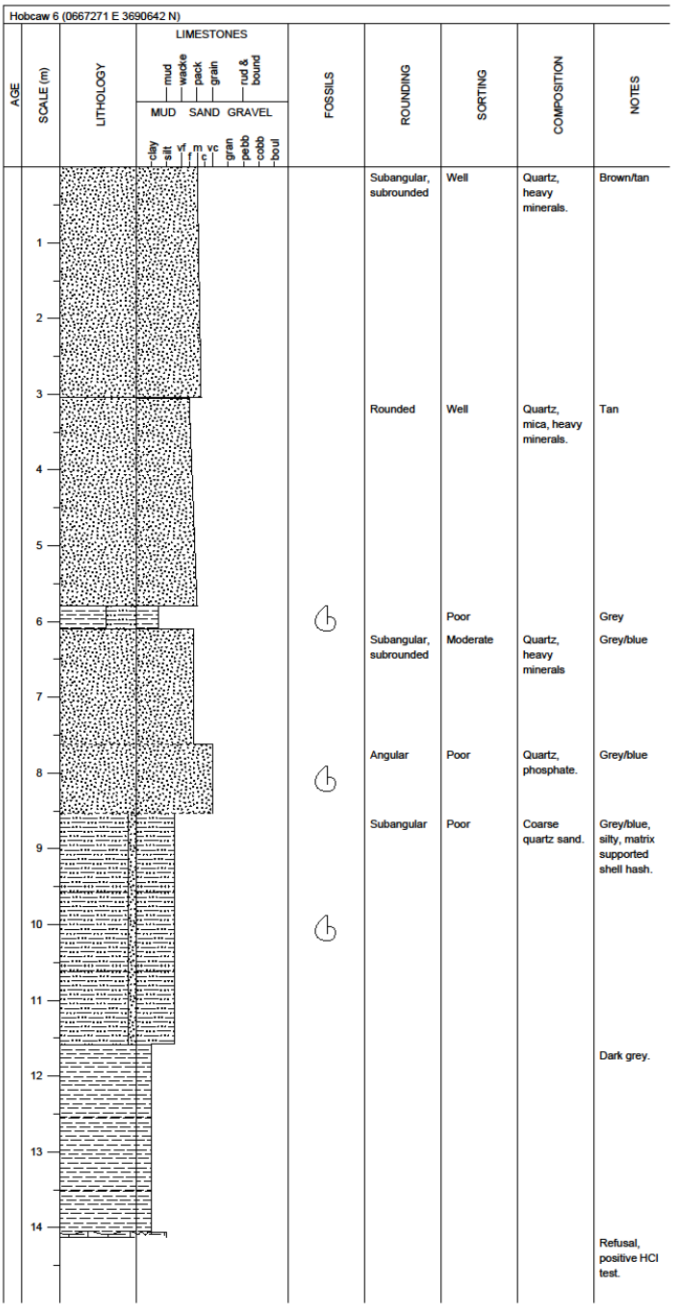

Figure B.7. Hobcaw 6 sediment log.

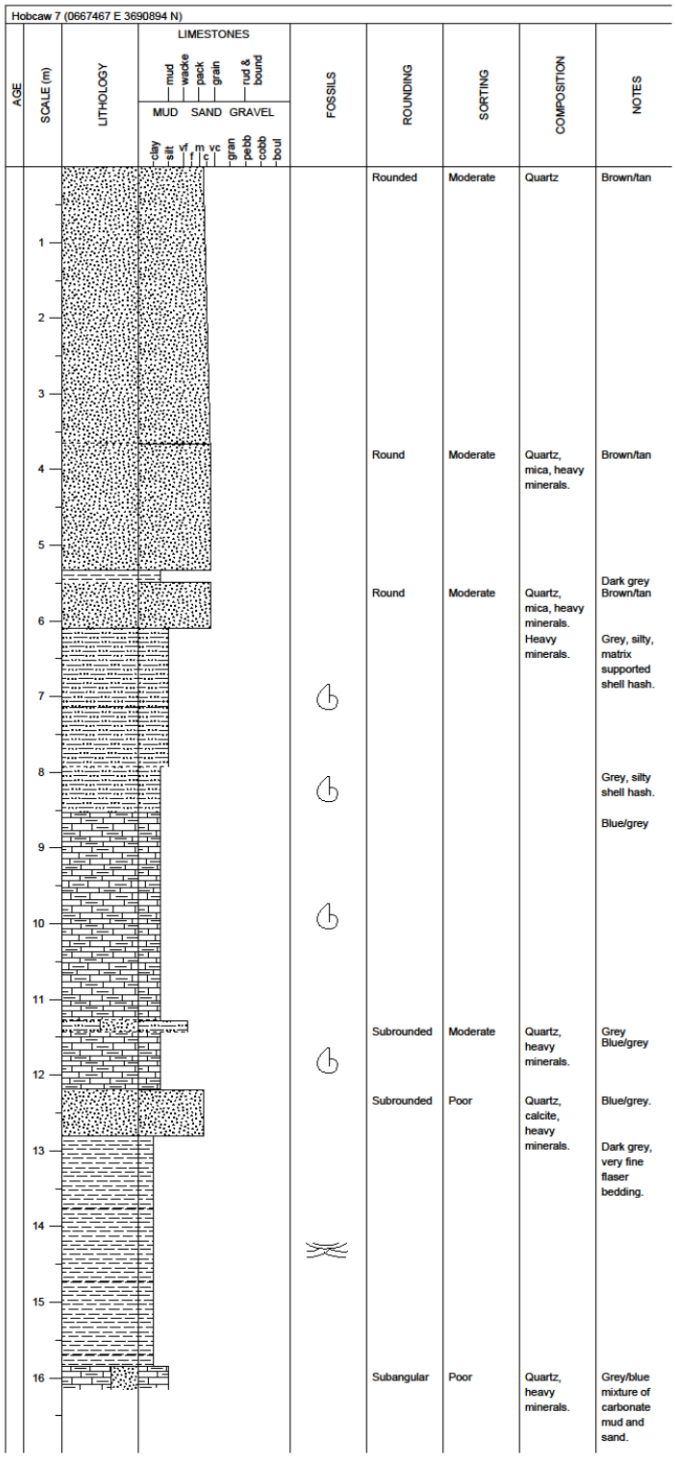

Figure B.8. Hobcaw 7 sediment log.

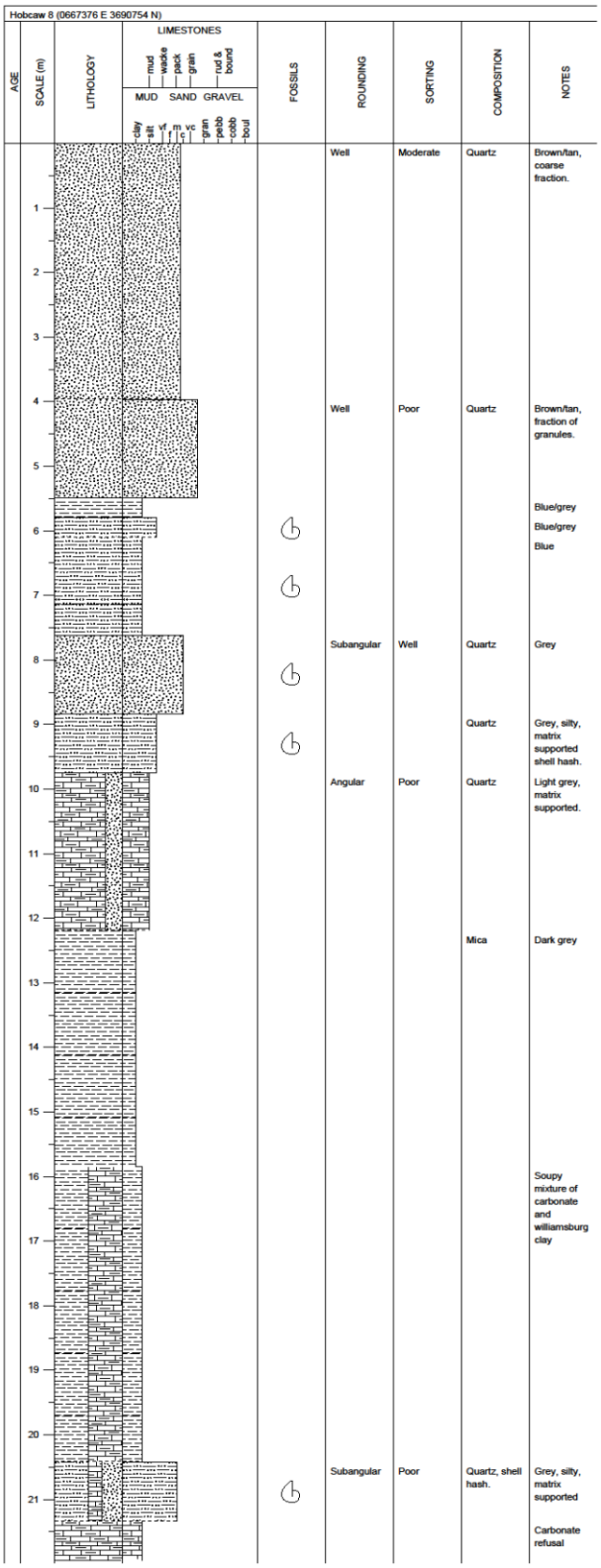

Figure B.9. Hobcaw 8 sediment log.

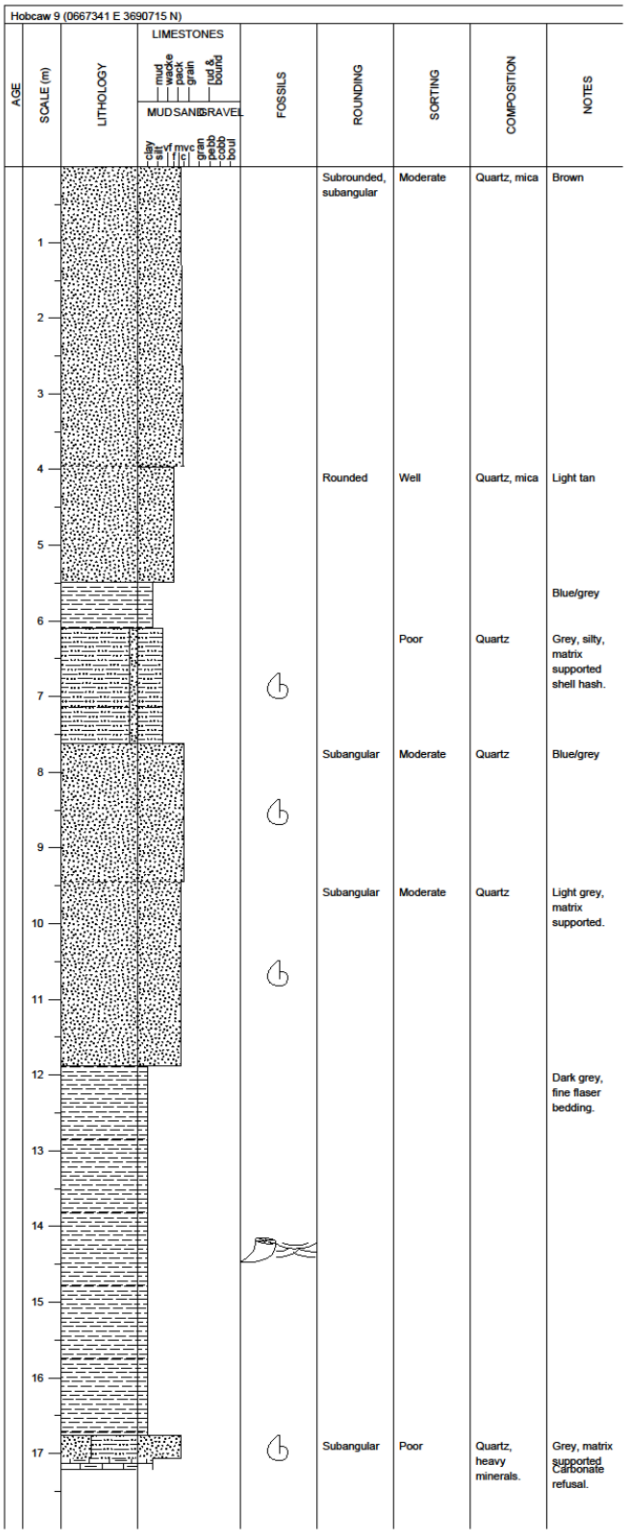

Figure B.10. Hobcaw 9 sediment log.

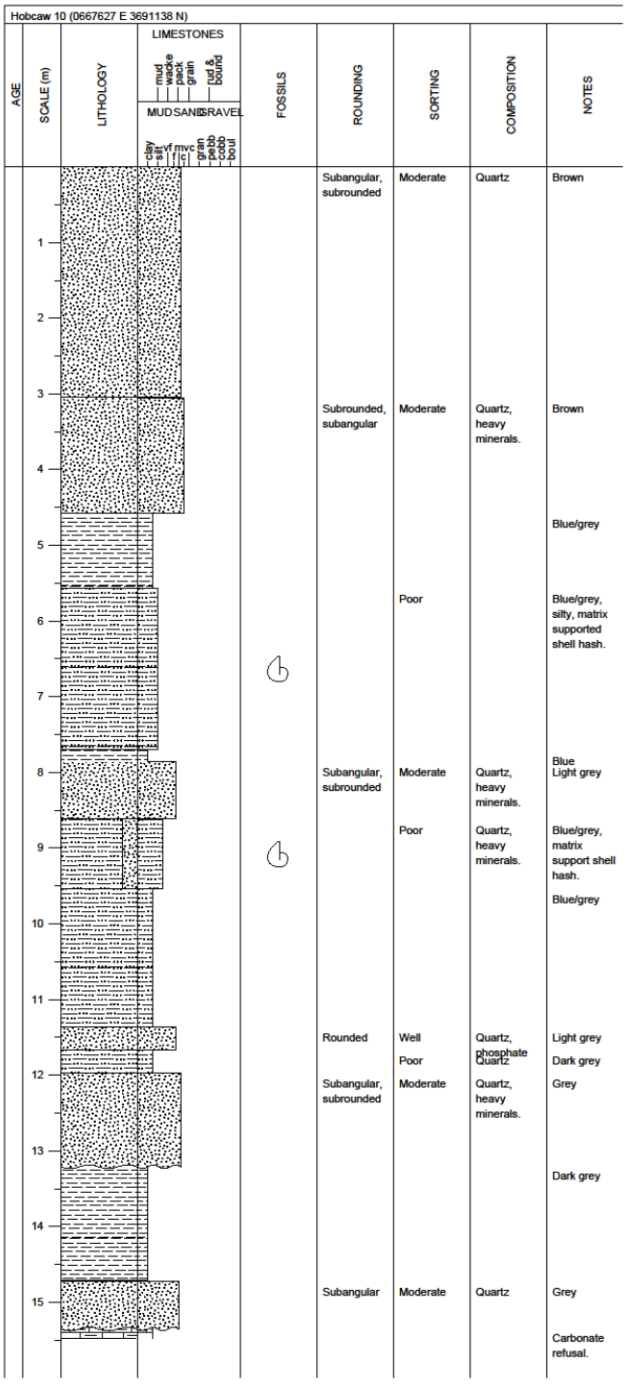

Figure B.11. Hobcaw 10 sediment log.

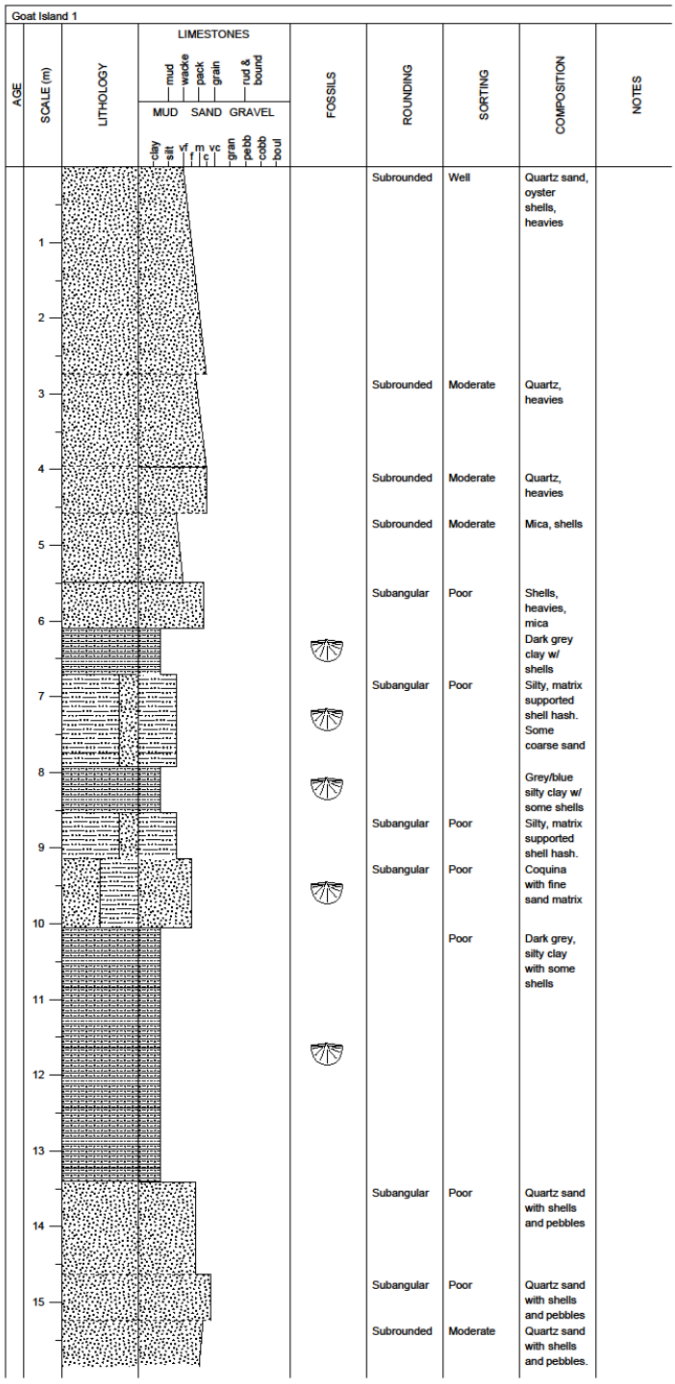

Figure B.12. Goat Island 1 Geoprobe log.

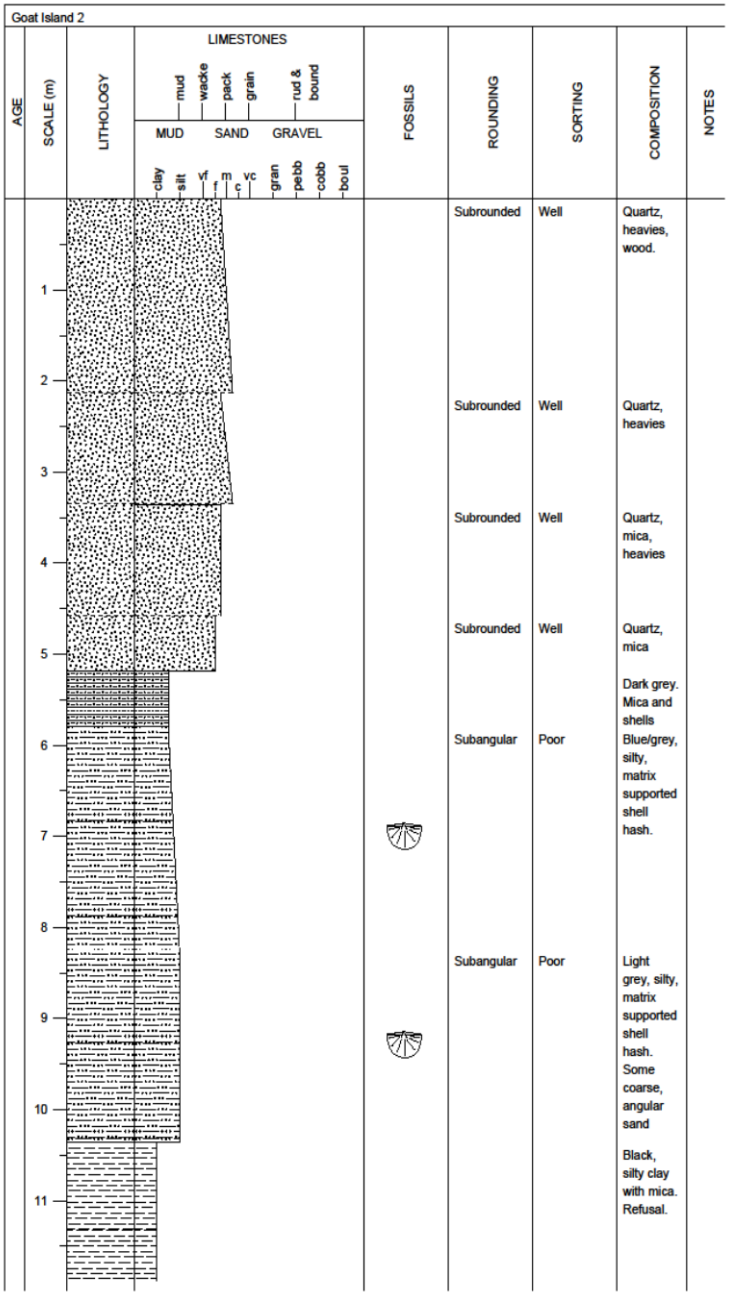

Figure B.13. Goat Island 2 Geoprobe log.

S2. Well Installation

Reproduced from SCDNR – Hydrology Division

MONITORING WELL CONSTRUCTION

Hobcaw Barony Wildlife Refuge

Georgetown County, South Carolina

Joe Gellici

STATEMENT OF WORK

The Contractor will provide well-drilling services to the South Carolina Department of Natural Resources, Land, Water and Conservation Division (SCDNR-LWC) at Hobcaw Barony Wildlife Refuge in Georgetown County. The contract calls for the construction of four monitoring wells having depths of 33, 39, 95 and 95 ft (feet). The contractor is responsible for providing all necessary materials and for constructing, grouting, developing, and finishing the wells. The wells will be used by SCDNR-LWC to monitor groundwater levels and salinity; consequently, no permanent pumps will be installed in the wells.

SITE DESCRIPTION

The wells will be drilled at two separate locations at the Hobcaw Barony Wildlife Refuge, which is located at 20 Hobcaw Road in Georgetown, South Carolina (Figure B.14). Owned by the Belle W. Baruch Foundation, the refuge is accessible by dirt road off U.S. Highway 17 (Ocean Highway) approximately 1 mile past the Waccamaw River Bridge.

The first site, herein referred to as the Goat Island site, is located at 33°20'06.08"N and 79°11'39.72"W (Figures B.14 and B.15). Two wells will be drill at this site (see details below). To access this site, a temporary bridge (20-ft Quick Bridge) must be erected over a small tidal creek. The Contractor is responsible for costs associated with the rental,

installation, and removal of the bridge. There is an existing bridge that spans this creek, but this bridge is not to be used for crossing with the drill rig.

The second site, herein referred to as the Hobcaw site, is located at 33°20'28.40"N and 79°12'12.04"W (Figures B.14 and B.15). Two wells will be drill at this site (see details below). This site is easily accessible; no bridges will need to be erected.

Other than the bridge, minimal site preparation is expected to be needed; however, the Contractor must take every responsible precaution to prevent damage to the property and to prevent leaking oil and other fluids onto the land surface.

WELL CONSTRUCTION SPECIFICATIONS

Specifications for the construction of the wells are given in this section.

General

The Contractor shall supply capable and experienced personnel and suitable drilling equipment to perform the work. The drilling crew shall use adequate safety equipment. Work shall be performed in accordance with all applicable Federal Occupational Safety and Health Administration standards.

The driller who is onsite shall be licensed by the State of South Carolina as a certified well driller. All work shall conform to applicable State and local regulations regarding well drilling and installation.

All work shall be completed before June 30, 2015. The SCDNR-LWC will provide a representative to monitor progress and assist the Contractor, as necessary.

No work shall take place on-site without a SCDNR-LWC representative present unless agreed upon in advance by SCDNR-LWC and the Contractor. The Contractor shall make no changes in the scope of work unless directed to do so by SCDNR-LWC. SCDNR-LWC shall be authorized to require the Contractor to stop work when specifications are not being met.

The Contractor will provide all well casing, well screen, well enclosures, and casing centralizers. The Contractor will be responsible for procuring, providing, and maintaining all other equipment and supplies necessary to perform the work described herein including drilling fluids, gravel-pack materials, and grouts.

SCDNR-LWC will obtain the necessary well-construction permits from the South Carolina Department of Health and Environmental Control (SCDHEC) prior to drilling. The Contractor will be responsible for complying with any other local, State, or Federal requirements as to licenses, permits, fees, etc., or regulations with respect to the drilling and construction operations. The Contractor will be responsible for filling out SCDHEC Water Well Records (Form 1903) for each of the wells within 30 days of well completion.

The Contractor must take every reasonable precaution to prevent damage to the property or fixtures on the property upon which the well is constructed. Any damage to the property or fixtures by the Contractor will be corrected by the Contractor at his expense.

The Contractor will be responsible for taking any precautions necessary to prevent leaking of oil or other contaminants into wells or mud pits or onto the land surface, and for cleaning up any contamination that occurs to the satisfaction of the SCDNR-LWC representative. Any contaminated soil or other materials will be disposed of in an area approved by SCDNR-LWC.

All materials used to prepare the drilling fluid must be composed of fresh non-polluted water and sodium bentonite. All other drilling fluid additives used must be approved by the SCDNR-LWC representative, they must comply with recognized industry standards and practices, and they will be used as prescribed by the manufacturer. No toxic and/or dangerous material can be added to the drilling fluid. If additives deemed

environmentally harmful by SCDNR-LWC are added to the drilling fluids then the drilling fluids will have to be removed from the site for proper disposal.

Drilling fluids and drill cuttings must be contained and disposed of in an area approved by SCDNR-LWC. Drilling fluids cannot be discharged directly into the marsh as the marsh/waterways are a part of the North Inlet-Winyah Bay NERR (National Estuarine Research Reserve).

No cement shall be disposed of at the drill site. If a cement truck is used for supplying grout and additional cement remains in the truck after the grouting operation is complete, this extra cement must be disposed of off-site.

All lubricants, greases, etc., are subject to SCDNR-LWC approval prior to commencement of drilling operations. All connections between drilling rods necessitating lubrication must utilize a lubricant approved by SCDNR-LWC. A list of all drilling muds, additives, and lubricants shall be provided to the SCDNR-LWC representative upon request.

Potable water and power will not be available at the site and must be provided by the Contractor.

Any hole in which the Contractor voluntarily stops work, and/or fails to complete in a satisfactory manner, in accordance with the specifications outlined herein by SCDNR-LWC or any approved changes, or fails to complete for any reason other than uncontrollable geologic circumstances (as determined by mutual agreement between SCDNR-LWC and the Contractor), will be considered abandoned by the Contractor. The Contractor will, at his expense, drill a new hole located as specified by SCDNR-LWC.

All abandoned holes must be properly plugged and sealed by the Contractor in accordance with State regulations. Any hole abandoned by the Contractor shall be properly plugged at the expense of the Contractor. All abandoned holes shall be plugged from bottom to top with cement.

The Contractor, in consultation with a SCDNR-LWC representative, may install surface casing to prevent caving of surficial sediments and mud loss. The casing shall be grouted with neat cement from bottom to top in one operation, either by pressure grouting or using a tremie pipe.

Drill cuttings are NOT required to be collected from the boreholes. A continuous core is available from a nearby borehole that has be used to determine well depths and screen locations.

Well Construction Details

Monitoring Well #1 – Goat Island site – Shallow well

This well will be 33 ft deep and constructed using a single-string installation with 4-inch PVC casing and 4-inch PVC screen (Figure B.16). The well will be gravel-packed and grouted with neat cement.

Construction specifications for the well are as follows:

- Total depth: 33 ft
- Borehole diameter: 8 inches
- Well casing: 31 ft of 4-inch diameter, Schedule-40, flush-joint, PVC
- Well screen: 2 ft of 4-inch diameter, Schedule-40, flush-joint, slotted PVC (0.010 slot)

The borehole will be drilled to a diameter of 8 inches and to a depth of 33 ft. A plug or cap will be screwed to the bottom of the well screen and the casing and screen will be inserted into and centered in the borehole to 33 ft.

Following insertion and alignment of the string of casing and screen, a filter pack (sand #2) will be emplaced around the well screen using a tremie-pipe method of emplacement.

The filter pack will extend from the bottom of the well (33 ft) to 1 ft above the screened interval (30 ft). A 5-ft bentonite plug will be emplaced at the top of the filter pack by gravity feeding or washing bentonite pellets through a tremie line, or by another method approved by SCDNR-LWC. The well will be grouted with Portland Type I neat cement from the top of the bentonite plug to land surface using a tremie-pipe method.

Following placement of the well screen, the well will be developed by blowing with air or by another method approved by SCDNR-LWC until a clear “sand free” discharge is achieved. It is estimated that well development will require a maximum time of two hours.

After well development has been completed, the well will be sounded by SCDNR-LWC. If any material is found at the bottom of the well, it must be cleaned out by the Contractor to the satisfaction of SCDNR-LWC. If the well is found to be defective, the Contractor will be responsible for repairing or replacing the well.

The well is to be finished with 4-inch casing protruding about 3 feet above land surface. The well will be enclosed with a 6-inch square protective steel enclosure equipped with a removable or hinged, lockable cap. The enclosure must be plumb to the satisfaction of SCDNR-LWC. A 3-foot by 3-foot concrete pad, about 4 inches thick, will be poured around the well.

Upon completion of the well drilling, the Contractor must remove and dispose of all cuttings and surplus material resulting from the work. The well site must be restored to its original condition to the satisfaction of SCDNR-LWC. Mud pits, if used, must be filled and leveled and all trash, scrap material, etc. shall be removed from the site. On-site disposal of non-hazardous drilling mud and drill cuttings would be considered if approved by SCDNR-LWC.

A well identification label must be attached to the well casing. It must include the company name and certification number of the driller who installed the well, the dated the well was completed, total well depth, and casing depth.

A water-well construction record (DHEC 1903 form) must be submitted by the driller to DHEC and DNR within 30 days of well completion.

Well Construction Details

Monitoring Well #2 – Goat Island site – Deep well

This well will be 95 ft deep and constructed using a single-string installation with 4-inch PVC casing and 4-inch PVC screen (Figure B.17). The well will be gravel-packed and grouted with neat cement.

Construction specifications for the well are as follows:

- Total depth: 95 ft
- Borehole diameter: 8 inches
- Well casing: 90 ft of 4-inch diameter, Schedule-40, flush-joint, PVC
- Well screen: 5 ft of 4-inch diameter, Schedule-40, flush-joint, slotted PVC (0.010 slot)

The borehole will be drilled to a diameter of 8 inches and to a depth of 95 ft. A plug or cap will be screwed to the bottom of the well screen and the casing and screen will be inserted into and centered in the borehole to 95 ft.

Following insertion and alignment of the string of casing and screen, a filter pack (sand #2) will be emplaced around the well screen using a tremie-pipe method of emplacement. The filter pack will extend from the bottom of the well (95 ft) to 3 ft above the screened interval (87 ft). A 5-ft bentonite plug will be emplaced at the top of the filter pack by gravity feeding or washing bentonite pellets through a tremie line, or by another method approved by SCDNR-LWC. The well will be grouted with Portland Type I neat cement from the top of the bentonite plug to land surface using a tremie-pipe method.

Following placement of the well screen, the well will be developed by blowing with air or by another method approved by SCDNR-LWC until a clear “sand free” discharge is achieved. It is estimated that well development will require a maximum time of two hours.

After well development has been completed, the well will be sounded by SCDNR-LWC. If any material is found at the bottom of the well, it must be cleaned out by the Contractor to the satisfaction of SCDNR-LWC. If the well is found to be defective, the Contractor will be responsible for repairing or replacing the well.

The well is to be finished with 4-inch casing protruding about 3 feet above land surface. The well will be enclosed with a 6-inch square protective steel enclosure equipped with a removable or hinged, lockable cap. The enclosure must be plumb to the satisfaction of SCDNR-LWC. A 3-foot by 3-foot concrete pad, about 4 inches thick, will be poured around the well.

Upon completion of the well drilling, the Contractor must remove and dispose of all cuttings and surplus material resulting from the work. The well site must be restored to its original condition to the satisfaction of SCDNR-LWC. Mud pits, if used, must be filled and leveled and all trash, scrap material, etc. shall be removed from the site. On-site disposal of non-hazardous drilling mud and drill cuttings would be considered if approved by SCDNR-LWC.

A well identification label must be attached to the well casing. It must include the company name and certification number of the driller who installed the well, the dated the well was completed, total well depth, and casing depth.

A water-well construction record (DHEC 1903 form) must be submitted by the driller to DHEC and DNR within 30 days of well completion.

Well Construction Details

Monitoring Well #3 – Hobcaw site – Shallow well

This well will be 39 ft deep and constructed using a single-string installation with 4-inch PVC casing and 4-inch PVC screen (Figure B.18). The well will be gravel-packed and grouted with neat cement.

Construction specifications for the well are as follows:

- Total depth: 39 ft
- Borehole diameter: 8 inches
- Well casing: 37 ft of 4-inch diameter, Schedule-40, flush-joint, PVC
- Well screen: 2 ft of 4-inch diameter, Schedule-40, flush-joint, slotted PVC (0.010 slot)

The borehole will be drilled to a diameter of 8 inches and to a depth of 39 ft. A plug or cap will be screwed to the bottom of the well screen and the casing and screen will be inserted into and centered in the borehole to 39 ft.

Following insertion and alignment of the string of casing and screen, a filter pack (sand #2) will be emplaced around the well screen using a tremie-pipe method of emplacement. The filter pack will extend from the bottom of the well (39 ft) to 1 ft above the screened interval (36 ft). A 5-ft bentonite plug will be emplaced at the top of the filter pack by gravity feeding or washing bentonite pellets through a tremie line, or by another method approved by SCDNR-LWC. The well will be grouted with Portland Type I neat cement from the top of the bentonite plug to land surface using a tremie-pipe method.

Following placement of the well screen, the well will be developed by blowing with air or by another method approved by SCDNR-LWC until a clear “sand free” discharge is achieved. It is estimated that well development will require a maximum time of two hours.

After well development has been completed, the well will be sounded by SCDNR-LWC. If any material is found at the bottom of the well, it must be cleaned out by the Contractor

to the satisfaction of SCDNR-LWC. If the well is found to be defective, the Contractor will be responsible for repairing or replacing the well.

The well is to be finished with 4-inch casing protruding about 3 feet above land surface. The well will be enclosed with a 6-inch square protective steel enclosure equipped with a removable or hinged, lockable cap. The enclosure must be plumb to the satisfaction of SCDNR-LWC. A 3-foot by 3-foot concrete pad, about 4 inches thick, will be poured around the well.

Upon completion of the well drilling, the Contractor must remove and dispose of all cuttings and surplus material resulting from the work. The well site must be restored to its original condition to the satisfaction of SCDNR-LWC. Mud pits, if used, must be filled and leveled and all trash, scrap material, etc. shall be removed from the site. On-site disposal of non-hazardous drilling mud and drill cuttings would be considered if approved by SCDNR-LWC.

A well identification label must be attached to the well casing. It must include the company name and certification number of the driller who installed the well, the dated the well was completed, total well depth, and casing depth.

A water-well construction record (DHEC 1903 form) must be submitted by the driller to DHEC and DNR within 30 days of well completion.

Well Construction Details

Monitoring Well #4 – Hobcaw site – Deep well

This well will be 95 ft deep and constructed using a single-string installation with 4-inch PVC casing and 4-inch PVC screen (Figure B.19). The well will be gravel-packed and grouted with neat cement.

Construction specifications for the well are as follows:

- Total depth: 95 ft
- Borehole diameter: 8 inches
- Well casing: 90 ft of 4-inch diameter, Schedule-40, flush-joint, PVC
- Well screen: 5 ft of 4-inch diameter, Schedule-40, flush-joint, slotted PVC (0.010 slot)

The borehole will be drilled to a diameter of 8 inches and to a depth of 95 ft. A plug or cap will be screwed to the bottom of the well screen and the casing and screen will be inserted into and centered in the borehole to 95 ft.

Following insertion and alignment of the string of casing and screen, a filter pack (sand #2) will be emplaced around the well screen using a tremie-pipe method of emplacement. The filter pack will extend from the bottom of the well (95 ft) to 3 ft above the screened interval (87 ft). A 5-ft bentonite plug will be emplaced at the top of the filter pack by gravity feeding or washing bentonite pellets through a tremie line, or by another method approved by SCDNR-LWC. The well will be grouted with Portland Type I neat cement from the top of the bentonite plug to land surface using a tremie-pipe method.

Following placement of the well screen, the well will be developed by blowing with air or by another method approved by SCDNR-LWC until a clear “sand free” discharge is achieved. It is estimated that well development will require a maximum time of two hours.

After well development has been completed, the well will be sounded by SCDNR-LWC. If any material is found at the bottom of the well, it must be cleaned out by the Contractor to the satisfaction of SCDNR-LWC. If the well is found to be defective, the Contractor will be responsible for repairing or replacing the well.

The well is to be finished with 4-inch casing protruding about 3 feet above land surface. The well will be enclosed with a 6-inch square protective steel enclosure equipped with a removable or hinged, lockable cap. The enclosure must be plumb to the satisfaction of

SCDNR-LWC. A 3-foot by 3-foot concrete pad, about 4 inches thick, will be poured around the well.

Upon completion of the well drilling, the Contractor must remove and dispose of all cuttings and surplus material resulting from the work. The well site must be restored to its original condition to the satisfaction of SCDNR-LWC. Mud pits, if used, must be filled and leveled and all trash, scrap material, etc. shall be removed from the site. On-site disposal of non-hazardous drilling mud and drill cuttings would be considered if approved by SCDNR-LWC.

A well identification label must be attached to the well casing. It must include the company name and certification number of the driller who installed the well, the dated the well was completed, total well depth, and casing depth.

A water-well construction record (DHEC 1903 form) must be submitted by the driller to DHEC and DNR within 30 days of well completion.

PROTECTION OF WATER QUALITY

The Contractor shall take precautions, as are necessary or as may be required by SCDNR-LWC, to permanently prevent contaminated water or water having undesirable physical or chemical characteristics from entering the water-bearing formations through any opening made by the Contractor. In the event that well becomes contaminated, or contamination enters the well due to neglect of the Contractor, he shall, at his own expense, perform such work or supply such casings, seals, sterilizing agents or materials as necessary to eliminate the contamination or shut off the undesirable water. The Contractor must exercise extreme care in the performance of his work in order to prevent the breakdown or caving in of strata overlying the formation from which water is to be drawn.

PROTECTION OF PERSON AND PROPERTY

Job performance is to be in compliance with all applicable OSHA safety regulations. An eye wash, first-aid kit, fire extinguisher and emergency telephone numbers shall be provided on site. The Contractor must maintain good housekeeping at the well site and at all equipment and storage locations. This means all facilities and equipment shall be kept neat, clean and orderly. All trash, mud sacks, cement sacks, and other disposable items must be contained at each well site and properly disposed of periodically. SCDNR-LWC shall be authorized to stop work if safety-related requirements are not followed. Continued, willful abuse of the safety and housekeeping requirements will be grounds for termination of this contract.

PAYMENT

Upon satisfactory completion of the wells, the Contractor will submit to the SCDNR-LWC a detailed statement listing total amounts of materials used in constructing the wells. In consideration for the satisfactory completion of the project, the SCDNR-LWC will make payment to the Contractor in a sum of 100 percent of the total bill. SCDNR-LWC will not pay for time lost due to rig breakdown, loss of tools, difficulties in procuring materials, or for abandoned holes.

<u>All work must be completed and invoiced by June 30, 2015.</u>

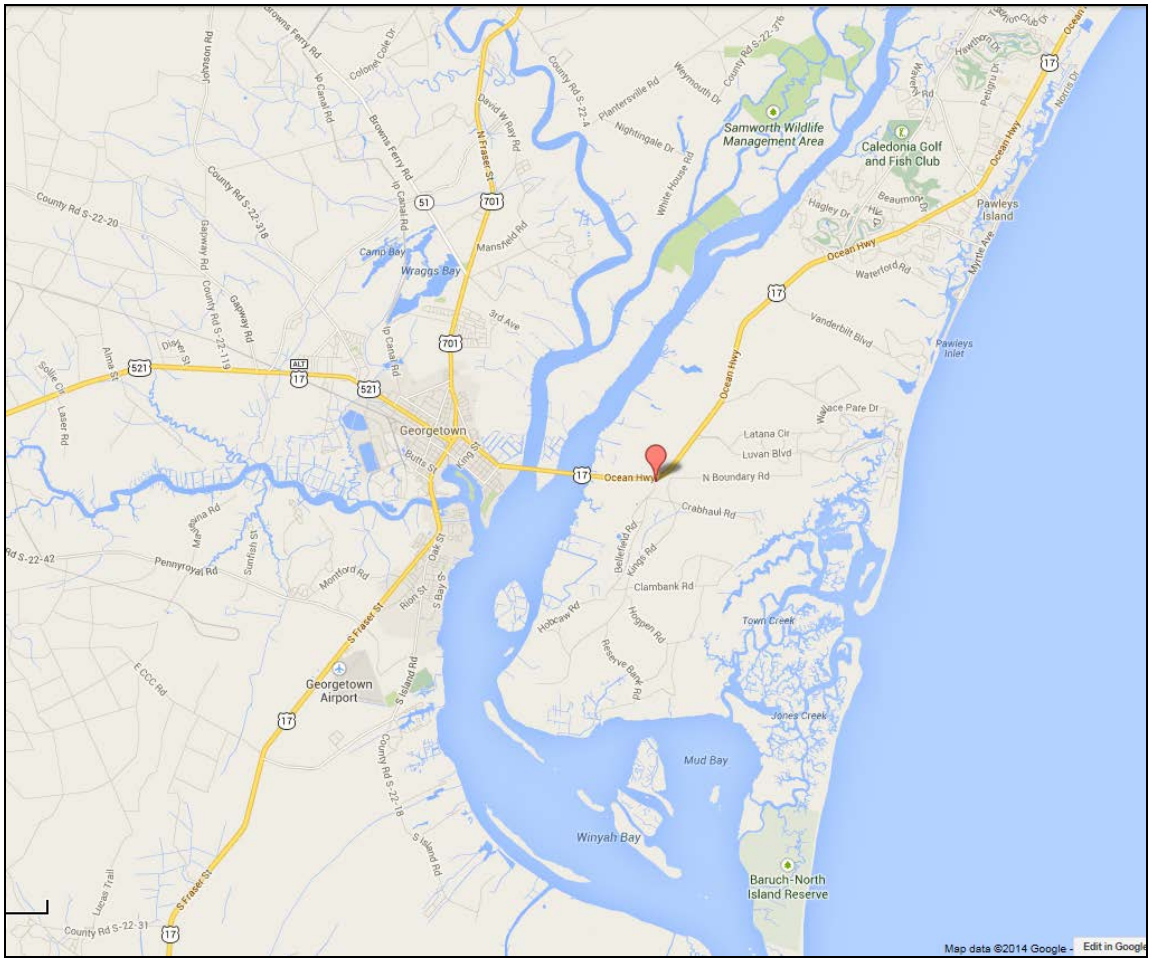

Figure B.14. Location of Hobcaw Barony wildlife refuge in Georgetown County.

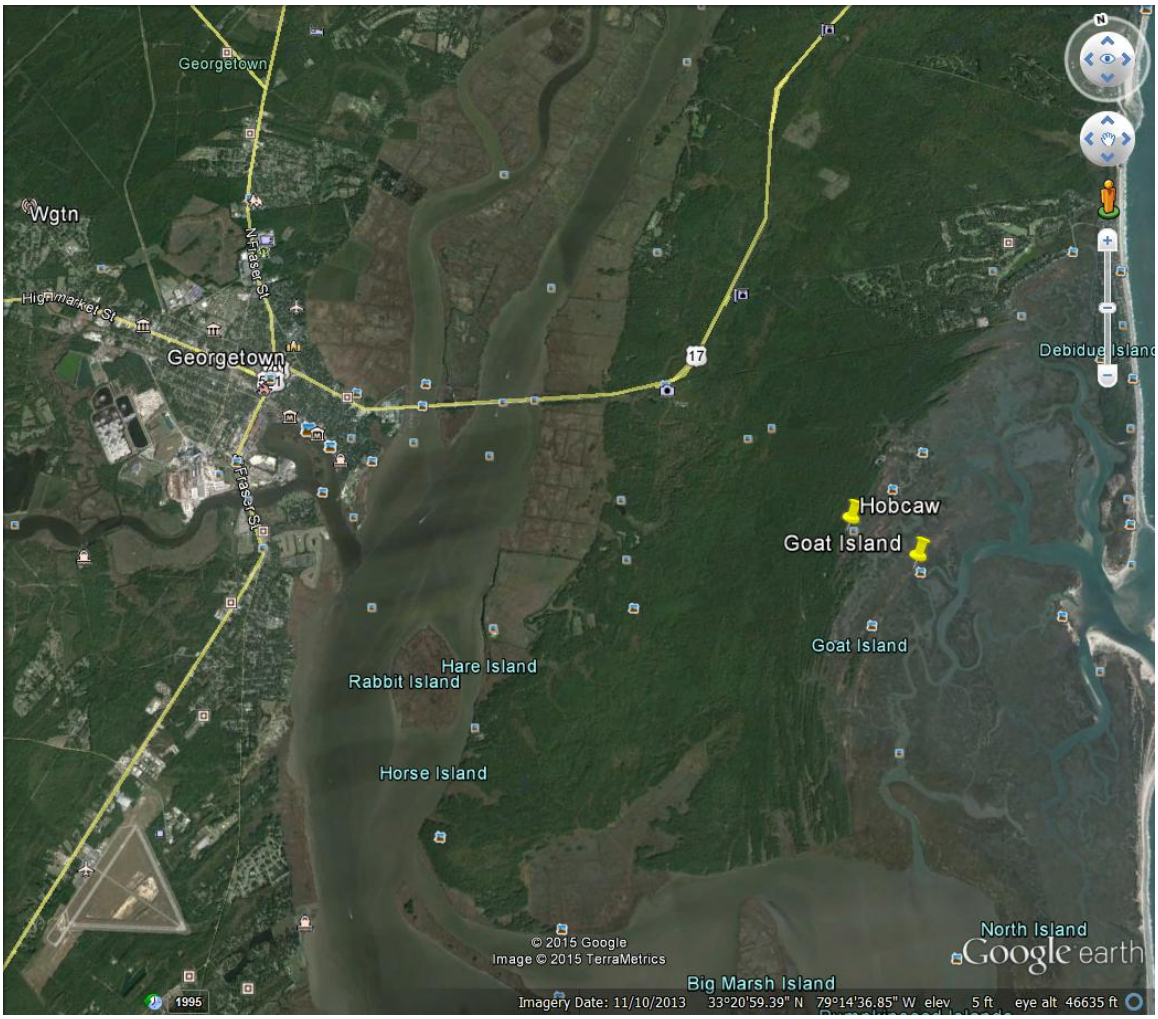

Figure B.15. Location of the Goat Island and Hobcaw drill sites.

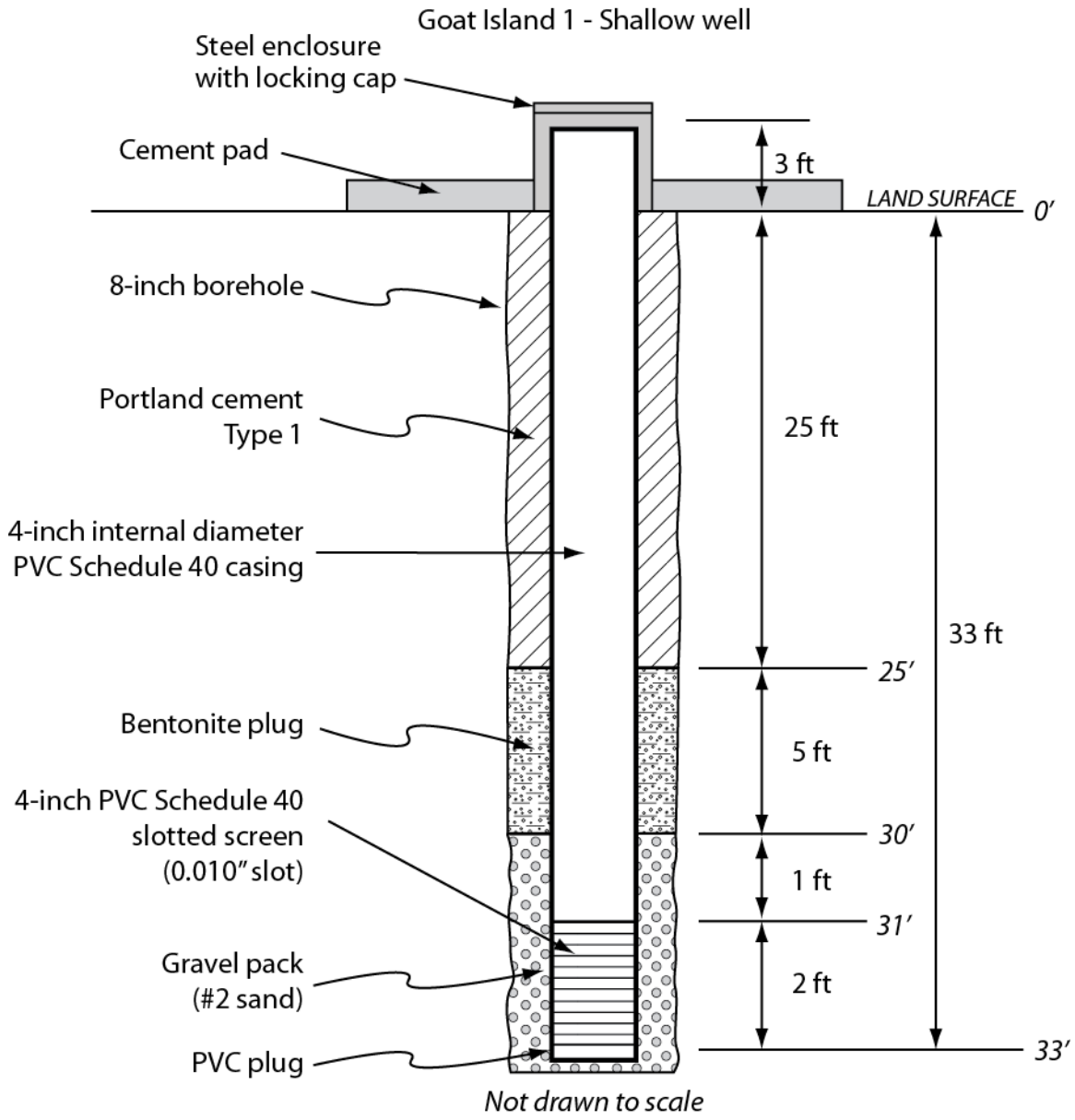

Figure B.16. Well-construction diagram for monitoring well #1.

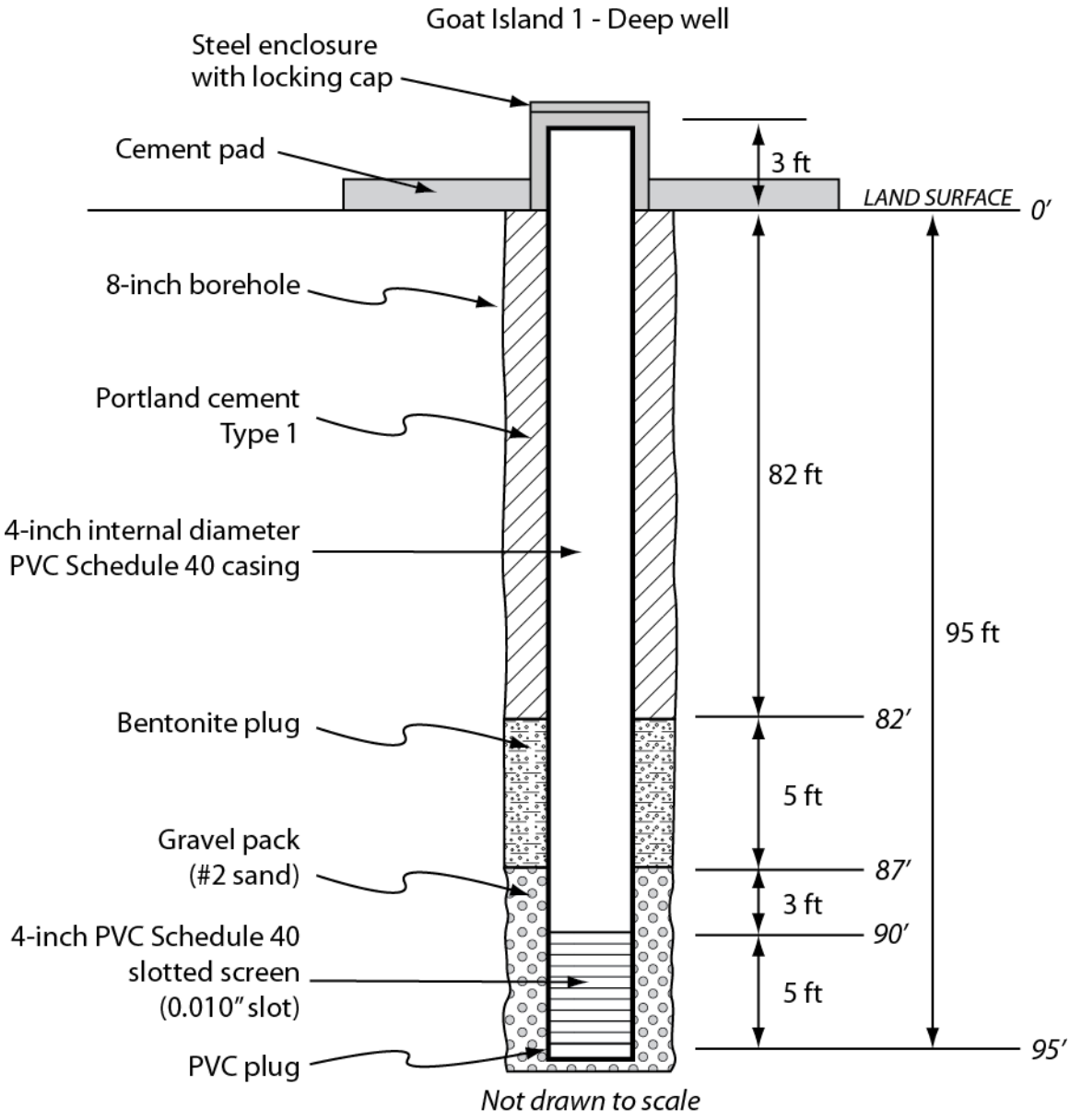

Figure B.17. Well-construction diagram for monitoring well #2.

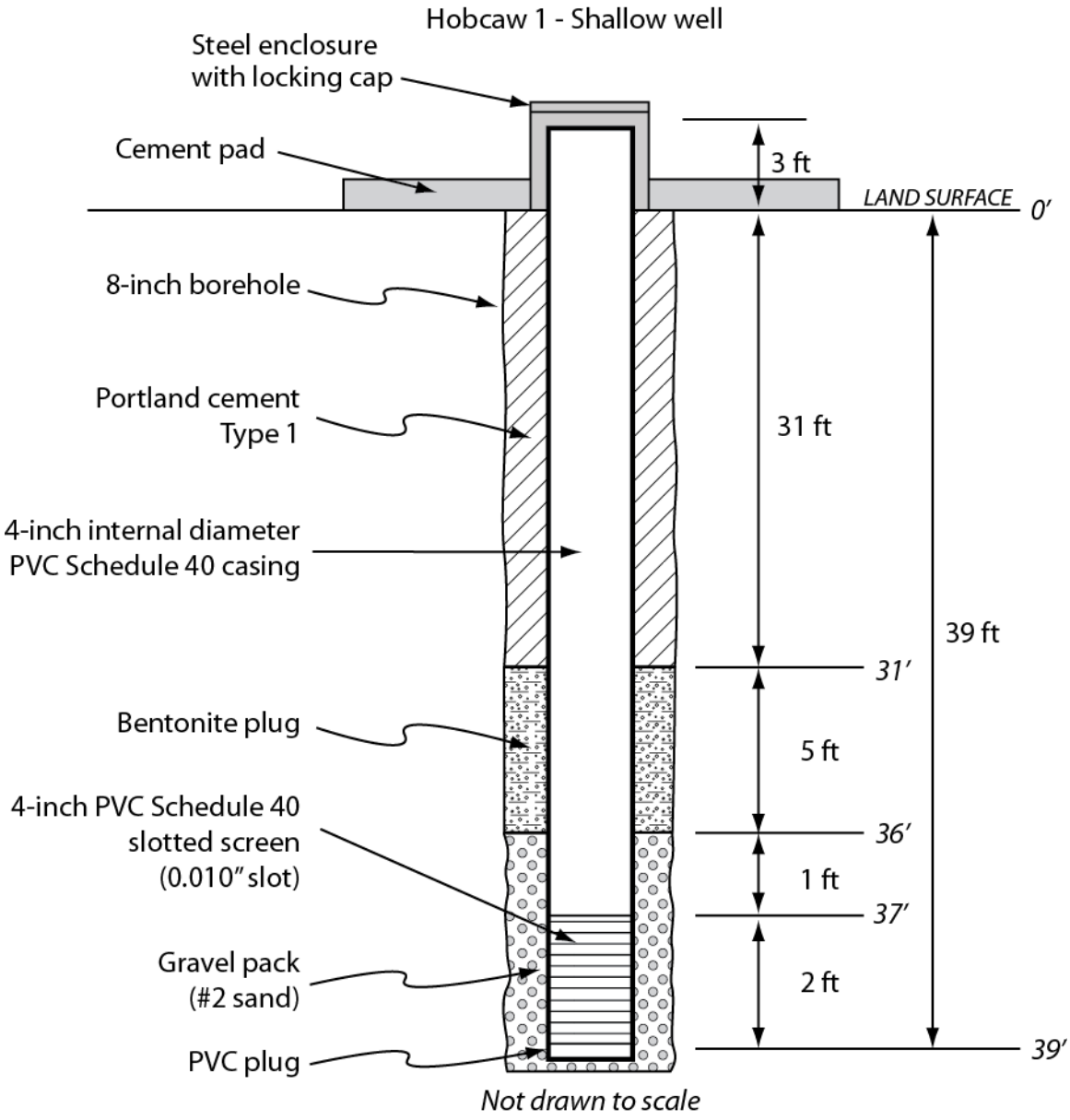

Figure B.18. Well-construction diagram for monitoring well #3.

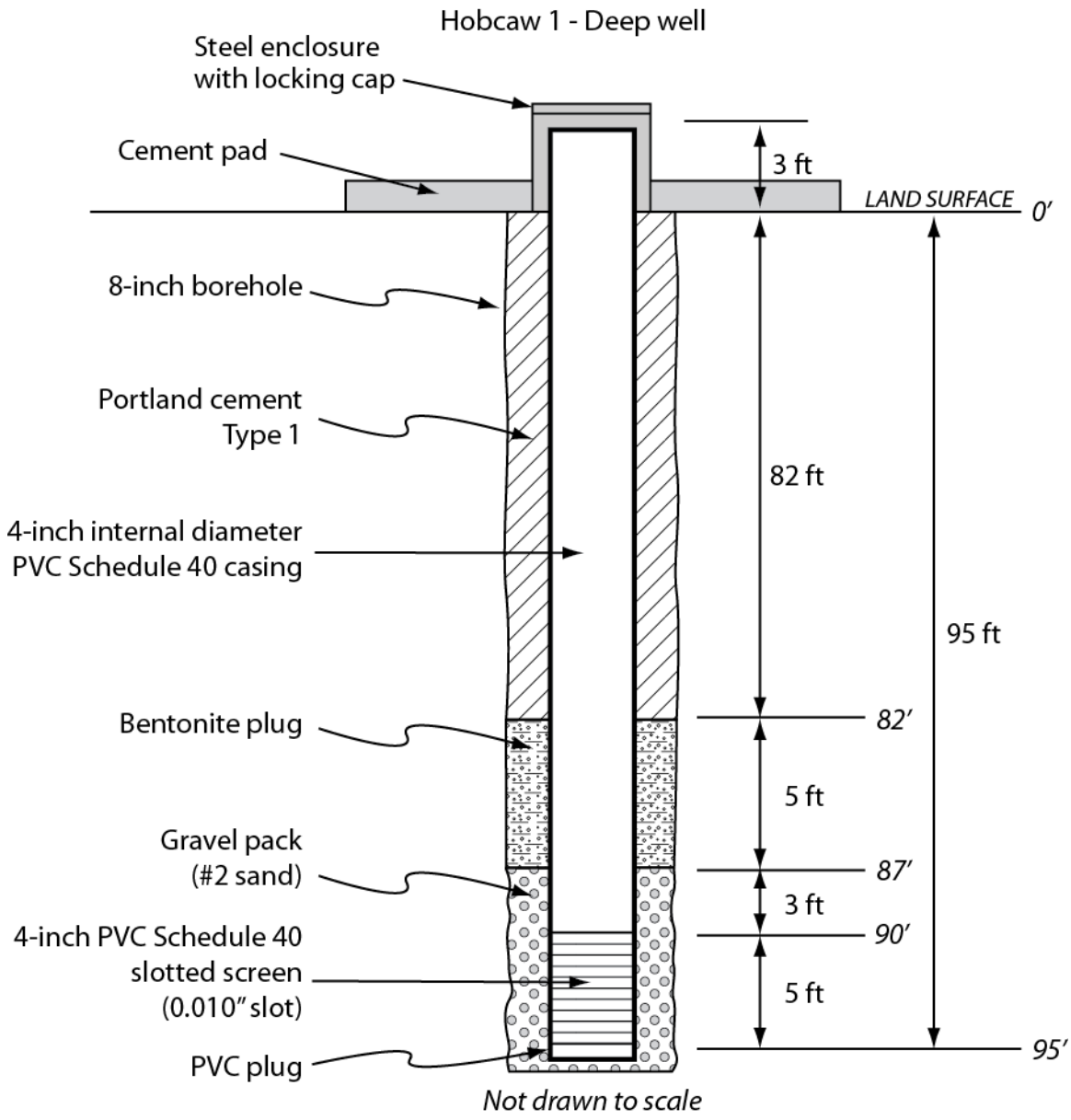

Figure B.19. Well-construction diagram for monitoring well #4.

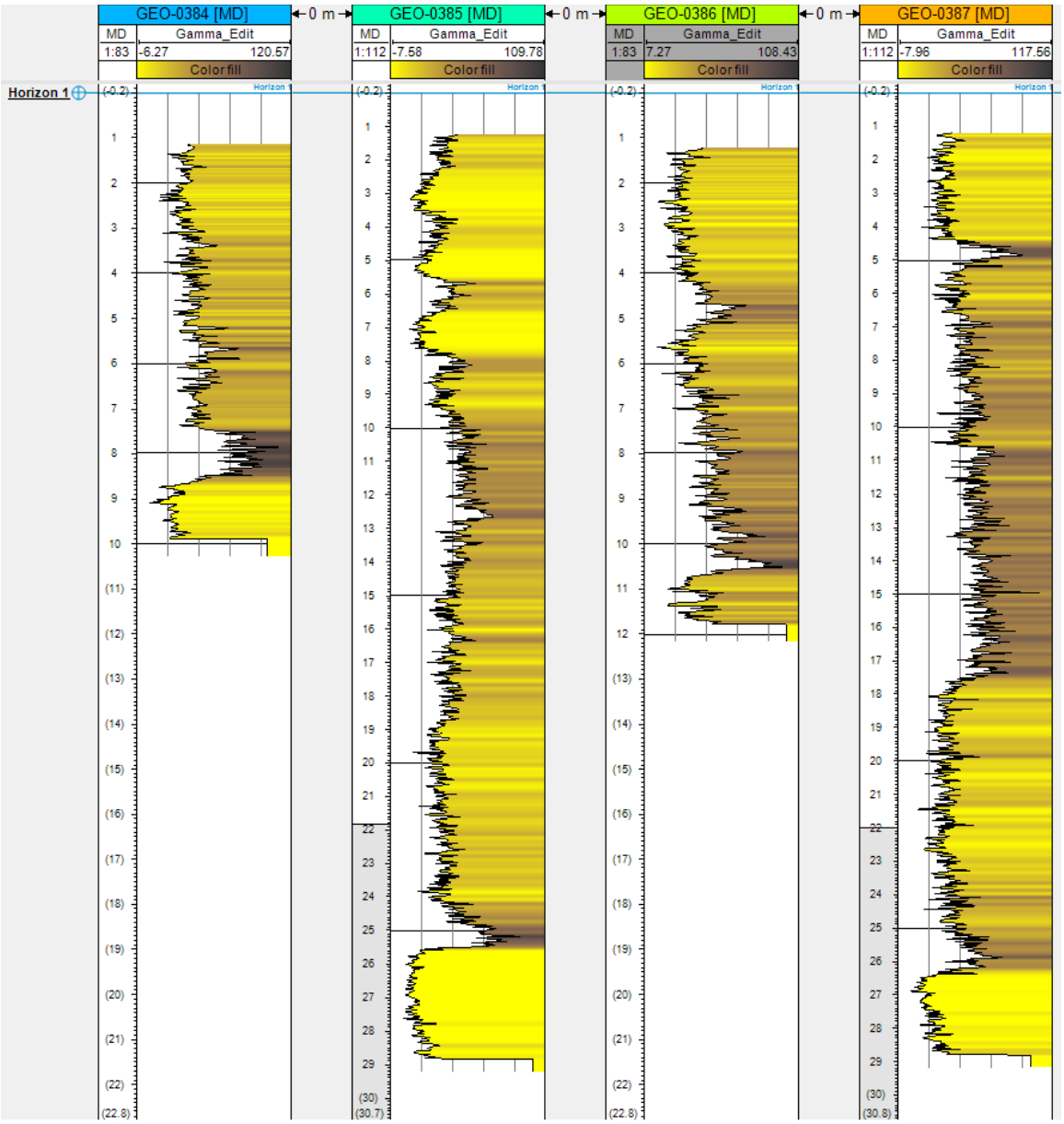

Figure B.20. Gamma ray log well the four wells

S3. North Inlet Model Calibration

We calibrated flow in the model to salinity data collected from the resistivity surveys and the four wells (GEO-0384, 0385, 0386, 0387). We chose permeability values that best represented our field data by comparing simulated hydraulic head and salinity to observed field data. We were able to calibrate groundwater salinities and head to field data with reasonable accuracy (Table B.1). However, we did not simulate evapotranspiration in our model, which led to a slight under approximation of salinity in the marsh basins.

The model was able to accurately reproduce measured groundwater salinity in wells GEO-0385, 0386, and 0387. The model was unable to reproduce saline groundwater conditions measured under Goat Island, in well GEO-0384, under any reasonable hydraulic circumstances. To accurately simulate the hydraulic head measured on Goat Island, rates of precipitation always dictated that groundwater here was fresh. These simulated fresh groundwater results matched the in-situ salinity data we collected from the geoprobe core and the resistivity results for Goat Island. We hypothesized that GEO-0384 was most likely screened in an isolated sediment interval with elevated groundwater salinity, such as a *salicornia* zone from a buried marsh platform.

For the confined sandy aquifer, we found a permeability of 5×10^{-12} m^2 to simulate hydraulic head that best matched the average hydraulic head measurements and amplitude of the tidal signal from wells GEO-0384 and 0386 (Table B.1; Fig. B.21a-c). For all simulations, hydraulic head in the confined sand aquifer increased with decreasing permeability. We found increasing values of permeability to increase the amplitude of the tidal signal (Fig. B.21b-c). In the Chicora Member, we found varying values of permeability to have a limited effect on the modeled hydraulic head. In general, the

simulated hydraulic gradient between wells GEO-0385 and 0387 increased with decreasing values of permeability (Table B.1). Decreasing values of permeability decreased the amplitude of the tidal signal in the simulated head (Fig. B.21d-e). A permeability of 5×10^{-13} m^2 completely attenuated the tidal signal in the simulated hydraulic head at the location of well GEO-0387 (Fig. B.21e). We found permeability values between 1×10^{-11} and 5×10^{-12} m^2 to best match observed hydraulic head and amplitude of the tidal signal in the Chicora Member (Table B.1; Fig. B.21d-e).

Table B.1. Simulated hydraulic head and groundwater salinity at quasi-equilibrium, averaged over a tidal cycle.

Results	GEO – 0384 (*Goat Island*)	GEO – 0386 (*Marsh Road*)	GEO – 0385 (*Goat Island*)	GEO – 0387 (*Marsh Road*)
Permeability (m^2)	**1×10^{-10}**		**1×10^{-11}**	
Average Hydraulic Head (m)	0.5	1.4	1.8	2.0
Average Hydraulic Gradient	-8.7×10^{-4}		-2.2×10^{-4}	
Average Salinity (ppt)	5.3	0	1.6	0
Permeability (m^2)	**5×10^{-11}**		**5×10^{-12}**	
Average Hydraulic Head (m)	0.5	1.5	1.7	1.9
Average Hydraulic Gradient	-8.7×10^{-4}		-2.5×10^{-4}	
Average Salinity (ppt)	2.3	0	0.32	0
Permeability (m^2)	**1×10^{-11}**		**1×10^{-12}**	
Average Hydraulic Head (m)	0.6	1.6	1.4	1.9
Average Hydraulic Gradient	-9.8×10^{-4}		-5.2×10^{-4}	
Average Salinity (ppt)	0	0	0	0
Permeability (m^2)	**5×10^{-12}**		**5×10^{-13}**	
Average Hydraulic Head (m)	0.7	1.8	1.2	1.9
Average Hydraulic Gradient	-1.0×10^{-3}		-6.5×10^{-4}	
Average Salinity (ppt)	0	0	0	0

*Grey shading indicates parameters used in subsequent simulations.

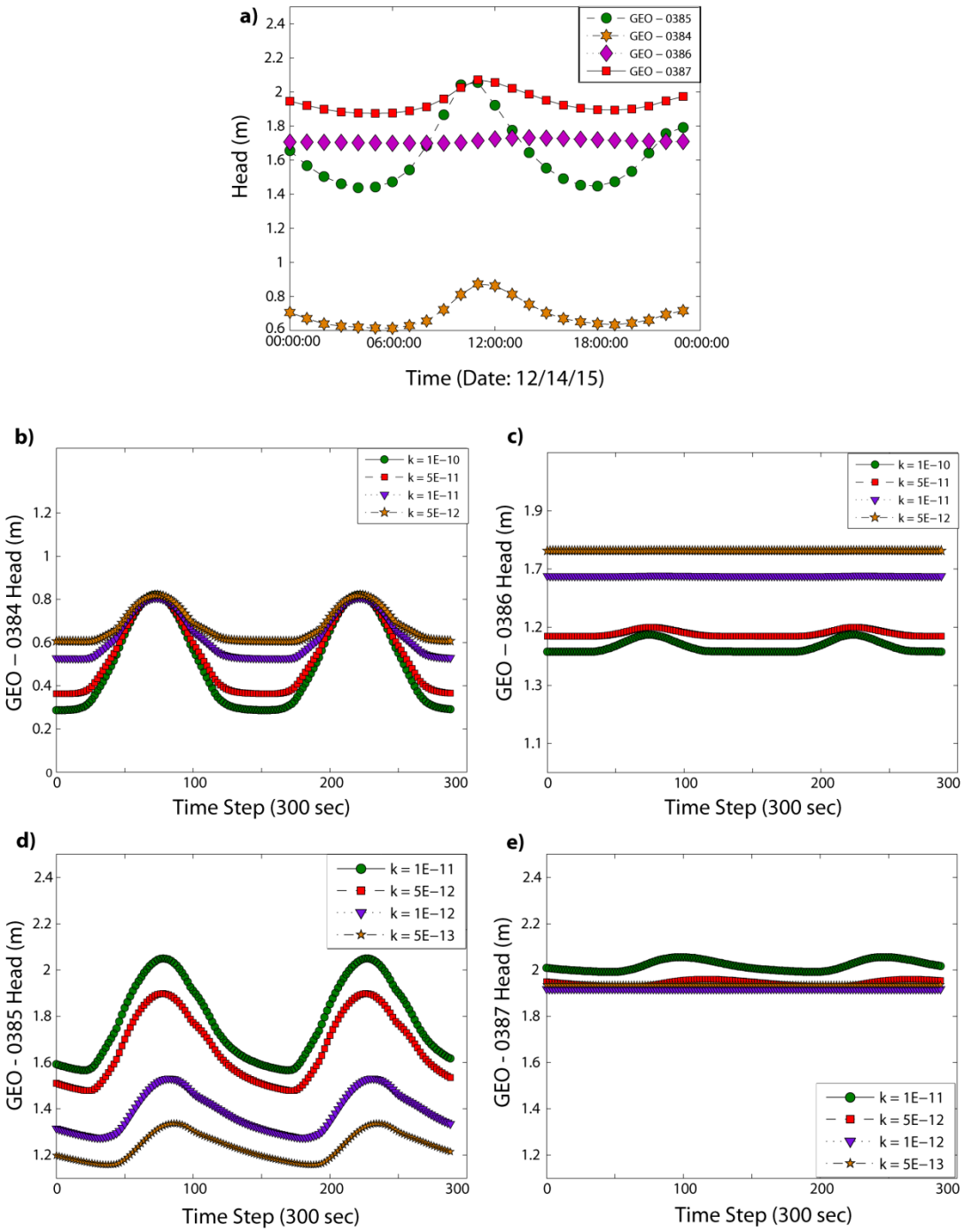

Figure B.21. Model calibration for the second confined aquifer and the Chicora Member aquifer. **a)** Observed hydraulic head data. **b-e)** Simulated hydraulic head data.